Transient Convection Heat Transfer of Helium Gas and Thermal Hydraulics in a Very High Temperature Gas-cooled Reactor

Wang, Li

(Degree)
博士（工学）

(Date of Degree)
2017-03-25

(Date of Publication)
2018-03-01

(Resource Type)
doctoral thesis

(Report Number)
甲第6954号

(URL)
https://hdl.handle.net/20.500.14094/D1006954

Doctoral Dissertation

Transient Convection Heat Transfer of Helium Gas and Thermal Hydraulics in a Very High Temperature Gas-cooled Reactor

（ヘリウムガスの過渡対流熱伝達及び
高温ガス炉内の熱流動解析）

January 2017

Graduate School of Maritime Sciences

Kobe University

Li Wang

（王　麗）

Abstract

Transient Convection Heat Transfer of Helium Gas and Thermal Hydraulics in a Very High Temperature Gas-cooled Reactor

The very high temperature reactor (VHTR) is developed to deliver significant advances compared with current active reactors in respect of economics, safety and proliferation resistance. Meanwhile, owing to the high reactor outlet temperature (to be achieved at about 1000 °C), VHTRs are designed not only aiming for electricity generation but also for process heat utilization e.g. hydrogen production, coal gasification, etc. To ensure safety, some thermal hydraulic problems remain to be solved like transient heat transfer problems, bypass and cross flows in the reactor core, thermal performance during loss of coolant situation and so on. In a VHTR system, the intermediate heat exchanger also requires to be better designed and demonstrated due to the relatively high temperature and high heat removal challenge. In this study, both fundamental experimental research of forced convection transient heat transfer and thermal-hydraulics analyses for reactor core by applying Computational Fluid Dynamics (CFD) were

performed.

Firstly, experimental research for forced convection transient heat transfer between the solid surface and the coolant (helium gas) was conducted. Twisted plates with different helical pitches, different lengths were investigated. The heat generation rate of the twisted plate was increased with a function of $\dot{Q} = Q_0 exp(t/\tau)$, where t is time, τ is period. Experiment was carried out at various periods ranged from 35 ms to 14 s and gas temperature of 303 K under 500 kPa. The flow velocities ranged from 4 m/s to 10 m/s. Platinum plates with a thickness of 0.1 mm and width of 4 mm were used as the test heaters. Platinum plates with a constant pitch size of 20 mm and different pitch numbers of 1, 3 and 5 were tested to show the effect of length on heat transfer coefficient. The transient heat transfer effect with various periods of heat generation rate was clarified and empirical correlations for both transient Nusselt number and quasi-steady state Nusselt number were obtained. The heat transfer enhancement effect by twisted structure effect was also clarified.

Then, three dimensional numerical simulation was applied to analyze the heat transfer process and twisted structure induced heat transfer enhancement mechanism. Numerical simulations for test heaters with various helical pitch sizes of 20 mm, 25 mm and 30 mm were conducted to study the effect of helical pitch size on heat transfer

coefficient and the results were compared to a flat plate. Additionally, Platinum plates with a constant pitch size of 20 mm and different pitch numbers of 1, 3 and 5 were also simulated to show the effect of length on heat transfer coefficient. Simulation results were obtained for average surface temperature difference, heat flux and heat transfer coefficient of the twisted plate and showed reasonable agreement with the experimental data. Based on the numerical simulation, mechanism of local heat transfer coefficient distribution was clarified. A comparison of the twisted plate and flat plate was conducted to show the difference in heat transfer coefficient distribution.

Finally, thermal-hydraulics analyses for reactor core by applying Computational Fluid Dynamics (CFD) were performed. The effects of bypass flow and cross flow gaps, which inevitably exist in the core of a VHTR were also taken into consideration. Validation study for the turbulence model was performed by comparing the friction coefficient with these by published correlations. A sensitive study for near wall mesh was conducted to ensure the mesh quality. Parametric study by changing the size of bypass gap and cross gap was performed with a one-twelfth sector of fuel block. Simulation results show the influence of bypass gap size on temperature distribution and coolant mass flow rate distribution in the prismatic core. It is shown that the maximum fuel and coolant channel outlet temperature increases with the increase in gap size which may lead

to a risk on the structure of fuel block. According to the simulation results, the cross flow can be divided to two kinds. One is the cross flow from bypass gap to coolant channels and another is the flow from high pressure coolant channels to low pressure coolant channels. These two kinds of flow have opposite influence on temperature gradient. It is found that the presence of the cross flow gaps may have a significant effect on the distribution of the coolant in the core due to flow mixing in the cross gaps.

Dedicated to my parents Qibin Wang and Suyun Peng,

my husband Ben Jiang and my best loved little angle Yixuan Jiang, for their unconditional love and encouragement throughout my life.

CONTENTS

Acknowledgements

This work cannot be completed without the help from an enormous number of people during my four years at Kobe University (one year on maternity leave). I would like to acknowledge some of them below.

I would like to express my deepest gratitude to my supervisor, Professor Liu, for his continuous guidance and help. He provided me with interesting projects and guided me with great patience. His expertise in Generation Four nuclear reactor was a great support for my research and he was always ready to discuss with me whenever I met problems. I am sincerely grateful for his continuous guidance and encouragements.

I would like to thank Professor Fukuda, for providing me with tremendously valuable advices on experiment research. His fruitful knowledge and hardworking spirit impressed me and my future career work will benefit from it. Additionally, Prof. Fukuda has supported me financially for the last year, for which I am sincerely thankful.

I recognized the help from the faculty, scientists and graduate students in the campus: Prof. Tomohisa Dan, Prof. Haruo Mimura, Prof. Akira Sou, Prof. Makoto Uchida, Prof. Shibahara, Miss. Kanako Nakao, Mr. Akihiro Mitsuishi and Mr. Shinya Ishiba.

I'd like to thank Prof. Guannan Xi in particular. Sometimes, open a new window means a new world for someone.

My gratitude goes to some people in our lab who provided assistance to my work. Especially, Dr. Zhao Zhou, thank you for the help on test heater manufacturing. The discussion with you are always inspiring. I am also grateful to Dr. Li Yantao, thank you for helping me with the experiment. Dr. Min Han Htet, wish you a great success in your country, Myanmar. Mr. Zhang Yu, thank you for the help on experimental tests for the flow decay transient research.

Support

1) I wish to acknowledge China Scholarship Council for the State Scholarship Fund (file No.201206840073) that supported my study in Japan as a PhD student.

Nomenclature

a	thermal diffusivity, m^2/s
C	coefficient in Eq. 4.6
c_h	specific heat of test heater, J/(kgK)
c_p	specific heat of helium gas, J/(kg·K)
d	diameter of the circular channel, m
E	total energy, J/kg
g	gravitational acceleration, m/s^2
h	heat transfer coefficient, $W/(m^2 K)$
h_f	enthalpy of the fluid, J/kg
h_s	enthalpy of the solid, J/kg
h_{st}	quasi-steady state heat transfer coefficient, $W/(m^2 \cdot K)$
H	180 degree twisted pitch, m
L	effective length of heater, m
Nu	Nusselt number, hL/λ
Nu_{st}	quasi-steady state Nusselt number, $Nu_{st} = h_{st} L_s / \lambda$

Nu_{tr}	transient Nusselt number (τ < 1 s)
p	static pressure, Pa
Pr	Prandtl number
$\dot{Q}$	heat generation rate per unit volume, W/m^3
Q_0	initial heat generation rate per unit volume, W/m^3
q	heat flux, W/m^2
Re	Reynolds number, UL/ν
Re_{sw}	Reynolds number based on swirl velocity, $U_{sw}L/\nu$
Re_y	turbulent Reynolds number, $\mathrm{Re}_y = \rho y_n \sqrt{k} / \mu$
Sw	Redefined swirl parameter, $\mathrm{Re}_{sw}/\sqrt{Y}$
T	temperature, K
T_a	average temperature of the heater, K
T_b	bulk temperature of the fluid, K
T_w	surface temperature of the heater, K
T_{wa}	average surface temperature, K
ΔT	temperature difference between wall and gas, K
t	time, s
U	velocity of helium gas, m/s

U_{sw}	swirl velocity, $U[1+(\pi/2Y)^2]^{1/2}$, m/s
X	coordinate along the axis of the plate, m
Y	coordinate along the width of twisted plate, m
y	twisted ratio, H/W
y_n	wall-normal distance, m
y^+	dimensionless distance, $y^+ = \rho u_\tau y_n / \mu$
Z	coordinate along the thickness of the plate, m
δ	heater thickness, m
ρ	Density of helium gas, kg/m^3
ρ_h	density of test heater, kg/m^3
λ	thermal conductivity of test heater, W/(m·K)
ν	kinematic viscosity of helium gas, m^2/s
τ	period of heat generation rate or e-fold time, s
τ^*	dimensionless period, $\tau U/L$
μ	molecular viscosity, kg/(m·s)

Subscript

b	bulk
f	film
h	test heater
s	swirl
st	quasi-steady state
t	turbulent
tr	transient state
w	wall surface(Heater surface)

Figure List

Chapter I

Introduction

Even a cursory glance at the Copenhagen Climate Change Conference (2009) shows that energy dilemmas are attracting extensive attention worldwide. It is suggest that the global energy consuming will increase by approximately 37% between 2014 and 2050.[1] While fossil fuels—oil, coal and natural gas will continue to account for the main part, it is hard to not only increase energy supplies but also effectively manage the environmental impacts including air pollution, global warming, acid rain and etc. Meanwhile, we have to keep in mind that our fossil fuel sources are finite natural sources. It is not hard to imagine that with the decrease in the fossil fuel sources and the increase in the cost of environment concerns, the energy price has to go higher in the near future. Higher energy price will certainly promote the development in renewable and nuclear energy. However, we are all concerned about the safety since nuclear energy is double-edged, providing relatively clean energy with price advantage but should a disaster due to nuclear accidents occur the damage would be incalculable. Such lessons have been learned more than once during the last fifty years, Three Mile Island accident (1979), Chernobyl disaster (1986), Fukushima Daiichi nuclear disaster (2011). Though the development of enhanced safety

assurance systems could reduce the risks of nuclear energy accidents, the safety coefficient could never reach a one hundred percent due to the unpredictable natural factors and the human factors involved in the nuclear power control system, the equipment maintenance, the accident management and so on. Therefore, serious considerations are required during the transition from current energy patterns to a sustainable energy future. The choices are very limited, though.

Early in 1987, the notion of sustainable development was given by Brundtland in a report named the world commission on environment and development, sustainable development is development that meets the needs of the present without compromising the ability of future generations to meet their own needs [2]. While the argument on whether the nuclear energy could be included in sustainable energy strategies has never stopped. At the national level, different government hold different attitudes. For example, nuclear energy is classified as sustainable energy in China, South Korea, and etc., but is ruled out in countries like Denmark, Austria and so on.

Under this background, the International Generation-IV Initiative was established in 2000 with global cooperation aiming at developing a new generation of nuclear energy systems to deliver significant advances compared with current reactors in respect of economics, safety, environmental performance, proliferation resistance, and physical

security. Countries involved in the Generation-IV International Forum (GIF) including Canada, China, EURATOM, France, Japan, South Korea, Switzerland and USA. Generally, six reactor systems were selected as candidates for meeting the Generation- IV goals [3]:

(1) Very high-temperature gas-cooled reactor (VHTR);

(2) Gas-cooled fast reactor (GFR);

(3) Sodium-cooled fast reactor (SFR);

(4) Lead-cooled fast reactor (LFR);

(5) Molten salt reactor (MSR); and

(6) Super-critical water-cooled reactor (SCWR).

Among all the Generation-IV reactors, the VHTR was selected by United States Department of Energy (DOE) for the Next Generation Nuclear Power (NGNP) Project, a project launched by Congress in the Energy Policy of 2005. The mission of the NGNP project is to demonstrate a high temperature gas-cooled reactor plant that would generate high-temperature process heat for use in hydrogen production and other energy-intensive industries while generating electric power at the same time. In the present stage, two types of reactor concepts, i.e., a prismatic graphite block type and a pebble bed type, are under development not only in USA but also in some other countries, such as South Korea,

Japan and China.

1.1 Historical development of gas-cooled reactors

Gas cooled reactors were developed since 1950s with various types and coolant gases. Some of the reactors were shut down, some were in operation, and still some were under constructions. The most commonly used coolant gas were carbon-dioxide and helium gas. A list of the gas cooled reactors from all over the world can be shown as follows:

(1) Graphite moderated Gas-cooled reactor, e.g. Magnox (UK) and Uranium Naturel Graphite Gaz reactor (UNGG, France).

(2) Advanced gas-cooled reactor (AGR)

(3) Heavy Water Gas Cooled Reactor (HWGCR)

(4) Gas-cooled fast reactor (GFR)

(5) Gas turbine modular helium reactor (GT-MHR)

(6) High temperature gas cooled reactor (HTGR)

(7) Pebble bed reactor (PBR), e.g. AVR reactor (Arbeitsgemeinschaft Versuchsreaktor, Germany) and thorium high-temperature nuclear reactor (THTR-300, Germany)

(8) Very high temperature reactor (VHTR)

The first commercial gas cooled reactor was a CO_2-cooled Magnox reactor called Calder Hall built in the United Kingdom, 1956 (shut down in 2003) . Since then, a total of 26 Magnox reactors were built in UK. Magnox reactors were also exported to other countries, such as Italy (Latina, 1987) and Japan (Tokai Mura, 1998). The fist Magnox reactors were designed principally to produce plutonium for nuclear weapons, while the efficiency was extremely low, only 18.8% [4]. Later, the Advanced Gas-Cooled Reactors were developed from the Magnox with improved thermal efficiency. Since 1976, a total of 14 commercial AGRs (seven stations, each with two AGRs) were built in the UK, and they are all still in operation with high availability.

The first HTGR was the 20 MW(t) Dragon test reactor in the UK constructed in the late 1950s/early 1960s and only operated until 1976. It is followed by two low-power HTGRs with different type: the Peach Bottom Unit 1 (1966-1974) in USA which is prismatic core with cylindrical fuel elements, and the AVR (1967-1988) in Germany which is pebble-bed core. Later, two-mid-sized HTGRs were constructed: the Fort St. Vrain (FSV, 1976-1989) in the USA, and the Thorium Hochtemperatur Reaktor (THTR, 1985-1991) in Germany. Although the operation for the test reactor and the low-power reactors were great success and demonstrated the technical feasibility of HTGRs, both

mid-sized HTGRs experienced a number of problems. Nevertheless, valuable feedback on the fuel was produced and several demonstrations of passive safety performance were proved. However, a temporary stagnation for the developing of HTGR begins from 1990s after the Power Nuclear Project (PNP-500) in Germany was brought to a halt [5].

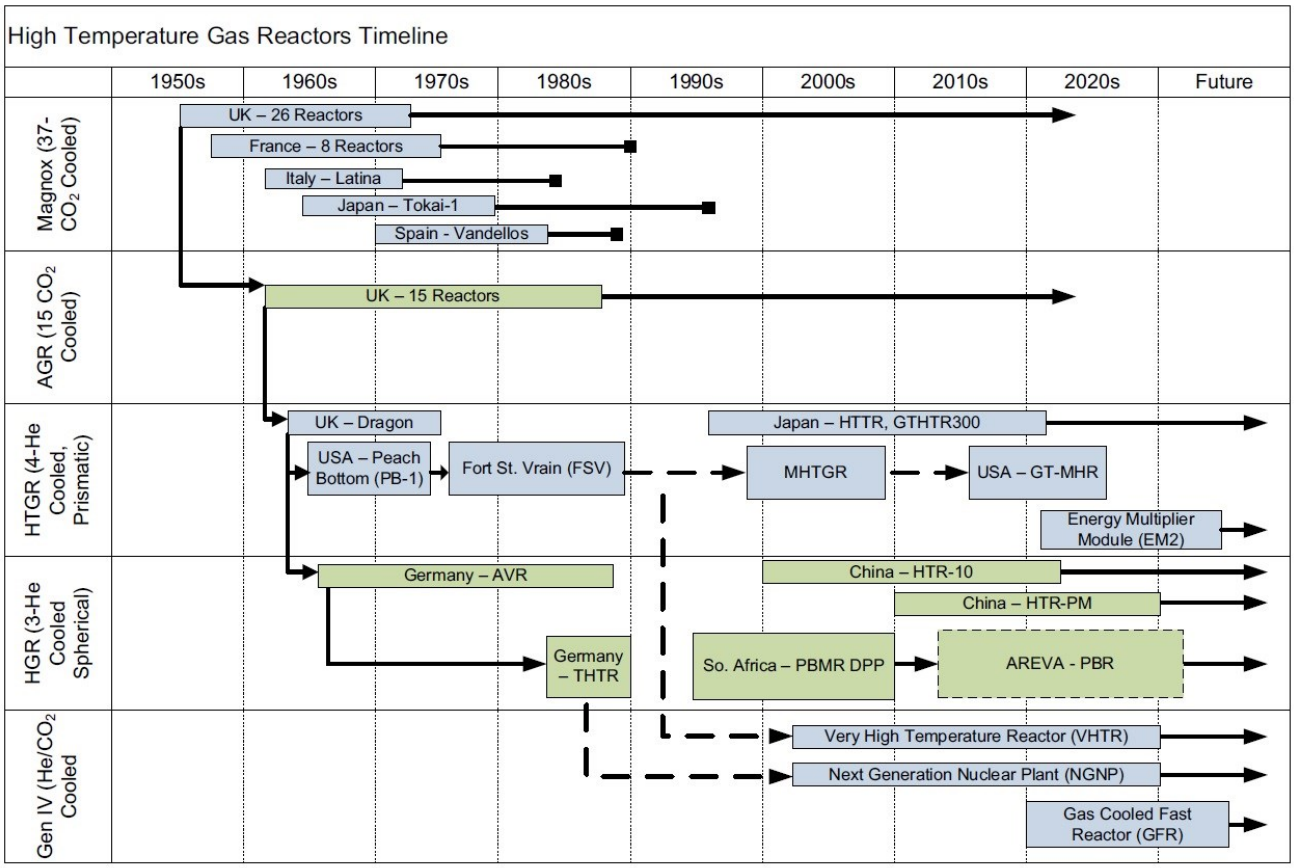

Figure 1.1 Timeline of HTGR development. [6]

The research on gas-cooled reactors did not gain much attention until recently owing to the possibility of passive safety performance and the high efficiency based on the high

reactor out let temperature. Now, two HTGR experimental reactors with different core types were in operation: the High Temperature Test Reactor (HTTR) with prismatic core in Japan, and the High Temperature Reactor (HTR-10) with pebble bed in China. A timeline for the HTGR development is shown in Fig.1.1 [6].

1.2 Status of new national projects

The global cooperation for developing the VHTR systems was driven by GIF in the signatory countries. A number of national R&D (Research and Development) and demonstration projects were established in South Korea, Europe, USA, Japan, China, and so on. Several newly designed HTGRs have been constructed or in the process of design.

South Korean: Two major projects has been established by the Korean government to support the South Korean long-term VHTR development plan: the key technologies development project and the nuclear hydrogen development and demonstration (NHDD) project. Key technologies in developing nuclear hydrogen systems including the design and analysis codes development, material and experiments technology, TRISO fuel manufacturing, SI hydrogen production technology and so on. The NHDD project aims at the design, construct and demonstrate of the nuclear hydrogen system by 2030 [7]. The NHDD project is expected to be supported by both the government and the industry, the

alliance was formed in 2009 with 7 nuclear industrial companies or institutes. Also, a memorandum of understanding (MOU) was signed by the Korean alliance with NIA (NGNP Industrial Alliance) at ICAPP (International Congress on Advances in Nuclear Power Plants) in 2013.

Europe: Europe has been a leader in High Temperature Reactors (HTRs) since 1960s with a lot of experimental and operational experiences accumulated from the test reactors DRAGON, AVR as well as the first European industrial high temperature prototype, THTR. Also, in the 1980s an innovative breakthrough-the modular concept was introduced which led to the design of the HTR MODULE and formed the basis of the HTR-10 and HTR-PM reactors later developed in China [8].

After the temporary break due to the nuclear phase out in Germany, the HTR development restarted in Europe in 1998, and since then a series of projects have been launched, INNOHTR in the Fourth Framework Programme (FP4), a cluster of nine coordinated projects (2000-2006) in the Fifth Framework Programme (FP5), RAPHAEL in the Sixth Framework Programme (FP6) and so on [9]. In addition, a long term coherent partnership for the development of HTR (High Temperature Reactor) technology was established in 2000, as known as the HTR-TN (high temperature reactor-technology network). Substantial achievements were gained from the network that it led to advances

in HTR/VHTR technologies which can contribute to the international cooperation through the GIF. The HTR-TN contributes mainly on the validation of computer codes or the design tools, the materials, component development, fuel manufacturing and irradiation behavior, and waste management [9]. Key experiments involving irradiation behavior, fuel burn up, safety tests, IHX tests, air ingress experiment, etc. have been performed or are still ongoing with the support of a series of European projects, such as the CARBOWASTE (in FP7), the EUROPAIRS, the ADEL, and the NC21-R.

USA: In the US, the Next Generation Nuclear Power (NGNP) Project was mandated by Congress in the Energy Policy of 2005 with two possible versions, one for a prismatic fuel type helium gas-cooled reactor and one for a pebble bed fuel type helium gas-cooled reactor [10]. Three basic requirements were set for the VHTR development: a coolant outlet temperature of about 1000 °C, passive safety, and a total power output consistent with that expected for commercial high-temperature gas-cooled reactors. Three major institutes or companies took part in the NGNP project: AREVA, General Atomics and Westinghouse. For the pre-conceptual design studies, General Atomics and AREVA mainly focused on the GT-MHR and prismatic block-type VHTR whereas Westinghouse was putting forward a Pebble Bed Modular Reactor. In 2008, the US-DOE and the Nuclear Regulatory Commission (NRC) submitted a joint licensing strategy to build a

framework for license application submission in order to get industry support for the NGNP project. In 2012, the NGNP industry Alliance has expressed a preference for the prismatic block type VHTR.

Japan: In 1969, the new generation reactor project was launched by Japan government aiming at not only the electricity generation but also the process heat for the iron industry. Around 1998, the High Temperature Test Reactor (HTTR) was built and since then the R&D was promoted by the Japan Atomic Energy Agency (JAEA). Under the government promotion, part of the work is cooperated with an OECD (Organization for Economic Cooperation and Development) /NEA (The Nuclear Energy Agency) project with the USA, South Korea, Czech Republic, France, Germany, Hungary and Japan as partners. VHTR related R&D consists of three parts, HTTR related tests, innovative HTR designs and hydrogen production technology. As for the innovative HTR designs, several innovation designs were suggested, such as the Naturally Safe High Temperature Reactor (NSHTR), the Clean Burn High Temperature Reactor (CBHTR) and the Multi-purpose HTGR (MPHTGR).

China: In 2007, the national projects on the development of nuclear power proposed by National Development and Reform Commission (NDRC) was approved by the State Council. The development of the generation four reactors were promoted by the

government finance support. As for HTR development, the preferred type was pebble bed type helium gas cooled reactor in China. The experimental reactor HTR-10 built by Institute of Nuclear and New Energy Technology (INET) of the Tsinghua University in China was put into service around 2000. Based on the experimental tests and analysis experiences gained from the HTR-10, a scaling up High Temperature Reactor-Pebble bed Module (HTR-PM, 210 MWe) project was started up. HTR-PM demonstration plant situated in Shidaowan of Shandong Province consists of two reactor modules that will drive together a single 210 MWe turbine. Construction started in 2012 and the commercial operation is scheduled for late 2017. Additionally, a proposal to construct two 600 MWe HTR plants- each with three twin reactor modules and turbine units- at Ruijing city in China's Jiangxi province passed a preliminary feasibility review in early 2015. Construction is expected to start in 2016.

1.3 Thermal-hydraulics challenges for VHTR system

While developing the HTGR system, both the prismatic type and the pebble bed type have experienced various problems not only in the reactor core, but also for the helium-driven gas turbine, the Intermediate Heat Exchanger (IHX) and the fuel cycling system due to the high temperature. One of the major concerns on the VHTR system is the

transient heat transfer process during the startup process, load change process or due to accidents e.g. power burst, rapid depressurization (Loss of coolant situation) and withdraw of control rods are rather complicated for the HTGR system. For instance, during power burst or loss of coolant accident, the graphite reflector acts as major heat sink to maintain fuel temperatures below the design limit maximum temperature for the fuel. This process has to be accurately designed and demonstrated to achieve passive safety demand for VHTR reactor. The behavior of heat transfer devices during transient processes with fast temperature changes may cause some undesirable results such as reduced thermal performance and thermal stress with eventual mechanical failure. Therefore, transient forced convection heat transfer process accompanying exponentially increasing heat input to a heater is important and a better understanding should be generated.

With improved temperature of the working fluid and cycle efficiency of the VHTR system, heat exchangers with high-effective, high integrity have to be achieved. Usually the compact heat exchangers are adopted with the application of heat transfer enhancement technology. A variety of techniques can be applied to improve the effectiveness of heat exchangers by generating strong secondary flows or increasing boundary layer turbulence, such as increasing the surface area by applying various

structures of fins, inserting of a twisted tape that consists in a periodical twist, improving surface roughness and using helically coiled tube. Though, it is well know that the twisted inserts will improve the heat transfer coefficient for the tube flow, the understanding for the mechanism of twisted plate induced secondary flow or turbulence increasing in the boundary layer was still not clearly generated.

Another major concerns on VHTR core is the fuel temperature. A report reviewing experience with the AVR published in 2008 pointed out that the AVR's fuel might have reached dangerously high temperatures during operation [11]. According to the design, maximum fuel operating temperature within the reactor should not exceed 1130 °C whereas the fuel pebbles which are designed to bear 1400 °C heat up, melted with the strips placed within nearby fuel pebbles meaning the reactor was being operated beyond the design limits. Though it was first stated as the result of poor-quality fuel pebbles, other reports show that it might be related to the extreme contamination of the AVR. Likewise, for the prismatic type HTGR, an important issue involving the performance of the fuel particles under normal operating conditions is the power peaking of the fuel rods which will lead to fuel hot spot, hot channels, and in some extreme conditions, the melting of fuel rods. For the prismatic type HTGR, possible solutions could be the use of burnable poison rod locations in the fuel blocks or graded particle pacing fractions in the fuel rod

rows after careful thermal-hydraulics analyses for the core.

In addition, Small gaps among the neighboring blocks exist due to tolerances in manufacturing and installation. Also, the gap size will change during the operation because of thermal expansion and fast-neutron induced shrinkage. Most of the coolant flows through the coolant holes as designed, while a little portion of coolant will flow through the gaps between hexagonal graphite blocks, which is defined as bypass flow. Besides, coolant flows in perpendicular direction to the coolant holes through the interfacial gaps between two block prisms is defined as crossflow. The existence of bypass and cross flow decreases the coolant flows through coolant channel and thus leads to an increase in maximum fuel temperature, which raises potential structural problems. In addition, some researches indicate that bypass and cross flow will cause a large variation in temperature for the coolant jets exiting the core into the lower plenum, which may cause “hot streaking” issue near the entrance of the hot outlet duct [12]. In this regard, evaluation of the core flow distribution and thermal hydraulic analysis are important for the reactor design and safety assessment.

1.3.1 Transient heat transfer problems

As introduced above, transient heat transfer processes has to be carefully studied to

ensure passive safety capability of VHTR reactor or to ensure the work temperature of intermediate heat exchanger (IHX) do not exceed limited maximum value.

Though many analytical solutions and experiments were reported on the steady state heat transfer, the transient process is much more difficult due to the complex thermal hydraulic phenomena. Soliman and Johnson analytically obtained a temperature change in plate by taking into account the turbulent boundary around the plate. However, the solution of heat transfer coefficient for water is 50% higher than their experimental data [13]. Kataoka et al conducted the transient experiment of water which flows in parallel to a cylinder, and obtained an empirical correlation for the ratios between the transient heat transfer coefficient and steady state one in term of one non-dimensional parameter composed of period, velocity, and heater length [14]. Liu and Fukuda obtained the experimental data and correlations for parallel flow of helium gas over a horizontal cylinder and a plate [15-17]. They investigated diameter and geometric effect of heaters on transient heat transfer. Meanwhile, they also did some simple numerical studies on transient heat transfer [18].

With the improvement of computer performance, the computational fluid dynamic (CFD) tool began to be applied for the numerical analysis of the transient heat transfer process. Gordeev et al. simulated steady state convective heat transfer in heated helium

channel flow at the flow Reynolds number below 10,000 by the commercial STAR-CD code [19]. Chen et al. tried transient simulation for helium cooled IFMIF (The International Fusion Materials Irradiation Facility) high flux test module by ANSYS CFX and Star-CD code and qualified the CFX k-ε model [20]. However the transient inner wall temperatures still have differences of over 10% by comparing to experimental results.

1.3.2 Utilization of HTHEs and heat transfer enhancement

Due to the high operation temperature, high temperature heat exchangers (HTHE) are required while developing the VHTR system. The shell-and-tube heat exchangers which are usually designed as helically arranged bundles were the first used intermediate heat exchanger (IHX) in the High Temperature Engineering Test Reactor (HTTR) of Japan [21]. Due to the high heat generation rate of the VHTRs, the IHXs used to remove the heat has to be carefully designed. Various kinds of heat transfer enhancement technologies are under developing in order to reduce space, weight and material cost of the IHXs.

Twisted plates are often adopted to enhance heat transfer in tube flows as turbulence promoters. There are some works on heat transfer using twisted-tape inserts in tubes and ducts to enhance heat transfer, usually in steady states with uniform wall temperature

(UWT) or uniform heat flux (UHF). Saha et al. conducted experimental study for regularly spaced twisted-tape induced laminar tube flow with UHF and the effect of tape width, higher-than-zero phase angle were discussed [22]. Manglik and Bergles investigated heat transfer and pressure drop correlations for twisted-tape-inserts in isothermal tubes [23, 24]. A wide range of Reynolds number from laminar to transition and transient flow had been studied. They also presented experimental flow visualization and computational modeling of single-phase laminar flows to clarify the mechanism of enhancement of heat transfer [25].

However, the researches mentioned above have been aiming at the heat transfer enhancement on the tube flow, the study focused on twisted plate itself was seldom reported. Hata et al. studied the twisted-tape-induced swirl flow heat transfer with exponentially increasing heat inputs and measured the pressure drop by a forced convective flow [26]. A predictable correlation for turbulent heat transfer of the twisted tape was derived based on experimental data. However, the study was based on water, for helium gas there is no reliable correlations or proper numerical models for the prediction of transient temperature and heat transfer coefficient. Hence, it is important to establish a database on forced convection of helium gas which can be applied to the thermal hydraulic analysis for the IHX.

1.3.3 Temperature and flow distribution in the core

In a prismatic VHTR core, most of the coolant flows through the coolant holes in the graphite compacts with or without fuel rods, while a little portion of bypass flow and cross flow will also occur. The flow distribution in the core has significant influence on the heat transfer performance within the core thus affects the temperature distribution in the core and the lower plenum where the helium gas mixed to reach relative uniform temperature and then flows out of the reactor. The location of maximum temperature of the fuel assembly in a reactor core is called hot spot. Due to the temperature limitation of the fuel rods, the hot spot temperature should not get over a criterial value of about 1600 °C. In addition, the existence of bypass and cross flow will decrease the amount of the coolant gas flows through the designed coolant channels. In some extreme circumstances, it might cause hot channel issue and lead to a large variation in temperature for the coolant jets exiting the core into the lower plenum, which may cause "hot streaking" issue near the entrance of the hot outlet duct. Therefore, the flow and temperature distribution in the reactor core requires well understanding and has to be carefully designed.

Simplified models such as the equivalent cylinder model and the unit cell model had been widely used for the analyses and designs for prismatic reactors [27]. Although a

basic evaluation of heat transfer in the core can be acquired with economically reduced computational efforts, these simplified models are hard to take the interior heat transfer within a single fuel assembly and the gap flow between fuel assemblies into consideration. Thus, full three-dimensional thermal hydraulics analysis for the reactor core have attracted great interest. Several experimental researches and computational fluid dynamic (CFD) analysis have been carried out to investigate the bypass and cross flow phenomena. For the complexity of core, experimental studies are based on simplified structures. These results show the effect of bypass and cross flow on flow distribution, and it is considered that pressure difference is the main influencing factor [28]. A Three dimensional simulation by using a one-twelfth sector of fuel block in full length of core has been conducted by Tak et al. [29]. The temperature distribution of the fuel block was clearly shown and a better understanding of the bypass flow influence was acquired. However the coolant mass flow rate distribution was not clarified through the calculation model.

Due to the complicated structure, massively computation capabilities are demanded for the full scale calculation. Such large computational requirements are not necessarily caused by the 3-D heat conduction in the graphite blocks, but rather by the simulation of helium flow in the coolant channel [30]. In this region, turbulence flow are coupled with solid surface and very fine mesh were required to solve the turbulence equations in the

boundary layer. Thus, replacing the 3-D CFD simulation of the helium flow in the coolant channel with empirical correlations will effectively reduce the computational requirements and make full core thermal hydraulics analysis possible. For VHTR core analysis, Travis and El-Genk tried 3-D full length CFD analysis for 1/6 core by applying a convective heat transfer correlation to the helium flow in coolant channels [31]. However, this correlation was not developed from experimental data, but based on the results of a 3-D numerical analysis of a single fuel module with a central flow channel. In light of these, it is deemed necessary to clarify the transient heat transfer process and to develop experimentally based empirical correlations for the forced convection of helium gas flowing over a solid surface to be applied in the VHTR core analysis.

For the study of bypass and cross flow in full length of core, CFD approach is even more complex due to the block structure. Thus, very few reports can be found. Sato et al. [32, 33] also conducted a research on the core by a one-twelfth sector. The influence of bypass flow on maximum fuel temperature and mass flow distribution were investigated. Wang et al. [34] studied the cross flow phenomenon based on a two-layer block model. According to the simulation result, a significant flow occurs in the crossflow gap by removing coolant from bypass flow gap toward coolant holes with a reduction up to 28% of the mass flow rate in the bypass flow gap. However this study is based on normal

atmospheric temperature without heating and the inlet boundary condition adopted is uniform mass flow rate condition.

1.4 Objectives and Outline of This Thesis

This research is conducted to study the thermal-hydraulics problems for the VHTR system including the transient heat transfer phenomena, the heat transfer enhancement for HTHEs, and the flow and temperature distribution in the reactor core. Experimental research and numerical simulation methods are both applied in this study.

In our previous research, Liu et al. [16-18] obtained the experimental data and correlations for parallel flow of helium gas over a horizontal cylinder and a plate. The diameter and geometric effect of heaters on transient heat transfer were investigated under wide experimental conditions. Meanwhile, some simple numerical studies on transient heat transfer have also been done by Zhao et al. [35]. In the study by Zhao et al., simulation works were based on simple structure of flat plate and several turbulence models were compared. However, there are few experimental data and numerical solution on helium gas flowing over a twisted plate, since simulation work is more complicated due to the structure.

In this paper, chapter 2 is focused on the experimental study of transient heat transfer

phenomenon. The experimental apparatus, the electric control and measurement circuit, the experimental method and procedure, the experimental conditions, and the experimental results will be introduced. The test heater was installed in a test loop that the pressure, flow velocity, and the temperature of the helium gas could all be adjusted to designed value. A twisted plate was used as the test heater with the heat generation rate increasing in an exponential function. The heat flux, surface temperature difference and heat transfer coefficient were measured under various heat generation periods and velocities. Experimental results for the transient heat transfer process due to exponentially increasing heat generation rate was generated.

In chapter 3, the numerical simulation method was introduced in detail with the simulation model, mesh validation, turbulence model selection. Numerical simulation results were obtained for average surface temperature difference, heat flux and heat transfer coefficient of the twisted plate and showed reasonable agreement with experimental data. A comparison for the heat transfer coefficient distribution along the twisted plate with a flat plate was shown to show the effect of the twisted structure. The heat transfer enhancement mechanism induced by the twisted structure was clarified.

In Chapter 4, the heat transfer enhancement by twisted structure was discussed by considering the influence of flow velocity, the effect of helical pitch, and the effect of

length. A series of twisted plate with different with different helical pitch and length was experimentally and numerically studied. The diameter and geometric effect of heaters on transient heat transfer were investigated under wide experimental conditions. In addition, three-dimensional transient simulation were also carried out to get the temperature distribution, velocity distribution and heat transfer coefficient. Effect of heater length on heat transfer was discussed based on the experimental data and simulation results. Correlations for quasi-steady state and transient heat transfer of twisted plate were obtained under wide experimental conditions. In addition, local heat transfer coefficient along the twisted plate was also investigated. According to this study, the numerical solution result for the single phase helium gas flow is reliable and could be applied as one of the approach for heat transfer enhancement design. In addition, the experiments for forced convection helium gas flowing over a heating surface in this research also provide as benchmarks for the numerical study of VHTR core.

In Chapter 5, the heat transfer process within a referenced GT-MHR is investigated by using the commercial code ANSYS FLUENT (ANSYS 14.0) based on the validated numerical simulation method in the Chapter 3 and 4. Effect of core bypass gap on flow distribution and fuel maximum temperature are studied with a full length model. Hot spot temperature of the block, coolant outlet temperature difference and bypass flow fraction

are compared for bypass gap sizes of 0, 3 and 5 mm. The detailed temperature distribution within the fuel block is clarified. Moreover, the influence of core cross flow on mass flow rate of coolant outlet channels and heat transfer in the core is also investigated.

Chapter II

Experimental Tests for Forced Convection Transient Heat Transfer

2.1 Introduction to the experimental apparatus

Experimental apparatus was reported in Liu et al. [17]. A schematic diagram of the experiment apparatus is shown in Figure 2.1. The experimental system is composed of gas compressor (2), flow meter (5), test section (6), surge tank (3), (8), cooler (7), the heat input control system, and the data measurement and processing system.

The main flow loop and flow direction of helium gas is shown by the arrows. A vacuum pump was used to degas the main flow loop and other branches. Helium gas was circulated by a compressor, and the fluctuations of gas flowing and pressure due to compressor were removed with the high-capacity surge tanks which are set at both inlet and outlet of the compressor. Moreover, the helium gas inside the loop was cooled by a cooler after the exit of the test section and before flows into the compressor and it will be heated to the desired temperature level by a preheater. Flowing rate in the test section was measured with the turbine meter, and the system pressure was measured with a pressure transducer. The temperature of the turbine meter exit and the temperature near test section

heater were measured by K-type thermocouples with a precision of ±1 K.

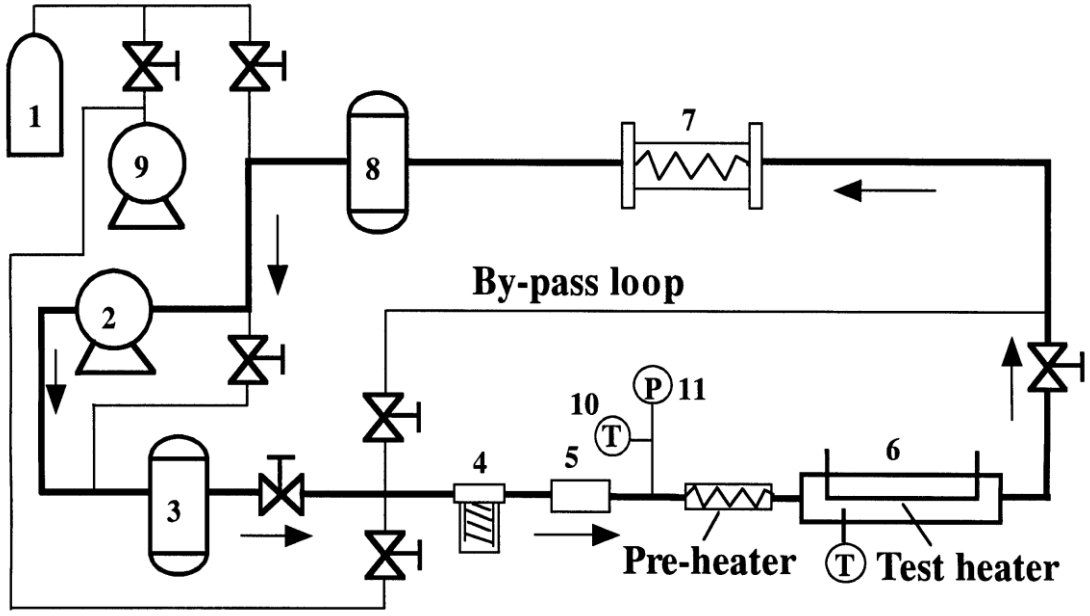

1. Gas cylinder 2. Compressor 3. Delivery surge tank 4. Filter

5. Turbine flow meter 6. Test section 7. Cooler 8. Surge tank

9. Vacuum pump 10. Thermocouple 11. Pressure indicator

Figure 2.1 Schematic diagram of experimental apparatus.

The test heater was mounted horizontally along the center part of the circular test channel, which is made of stainless steel (20 mm in the inside diameter), as shown in Figure 2.2. Platinum plate with thickness of 0.1 mm, width of 4 mm was used as the test heater. A twisted heater with the 360 degree helical pitch of 20 mm was used in the experiment. The ends of the heater were connected to two copper plates with the same thickness, then connected to two copper electrodes. Two fine platinum wires (50 μm-dia.)

were spot welded to the end parts of the twisted plate as potential conductors. The length between the potential taps is defined as the effective length on which transient heat transfer was measured.

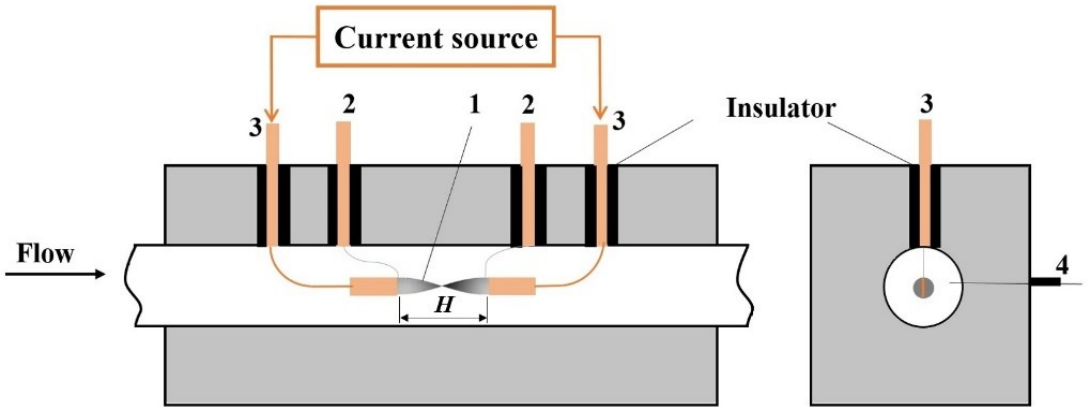

1. Test heater 2. Potential conductor 3. Current conductor 4. Thermocouple

Figure 2.2 The test section.

The test heater was heated by direct current from a power source. The heat generation rates of the heater were controlled and measured by a heat input control system [36]. The average temperature of test heater was measured by resistance thermometry using a double bridge circuit including the test heater as a branch [37]. The test heater was annealed and its electrical resistance versus temperature relation was calibrated in water, and washed with a trichloroethylene liquid before using it in the experiment.

2.2 Electrical control and measurement circuit

A schematic diagram of the overall electrical control and measurement circuit for the test section could be shown as Figure 2.3. A total of four parts including the double bridge circuit, electrical control and feedback part, the signal input part and the output data processing part were built with connections. The double bridge circuit (also called Kelvin Bridge or Kelvin double bridge) was applied to measure the resistance of the test heater so as to obtain the average temperature of the test heater with the calibrated temperature-resistance correlation. A high speed analogue computer was applied in part 2 to support a rapid and precise calculation-feedback process for the heat generation and heater temperature control. While the signal input and output data processing were fulfilled with a personal computer (PC).

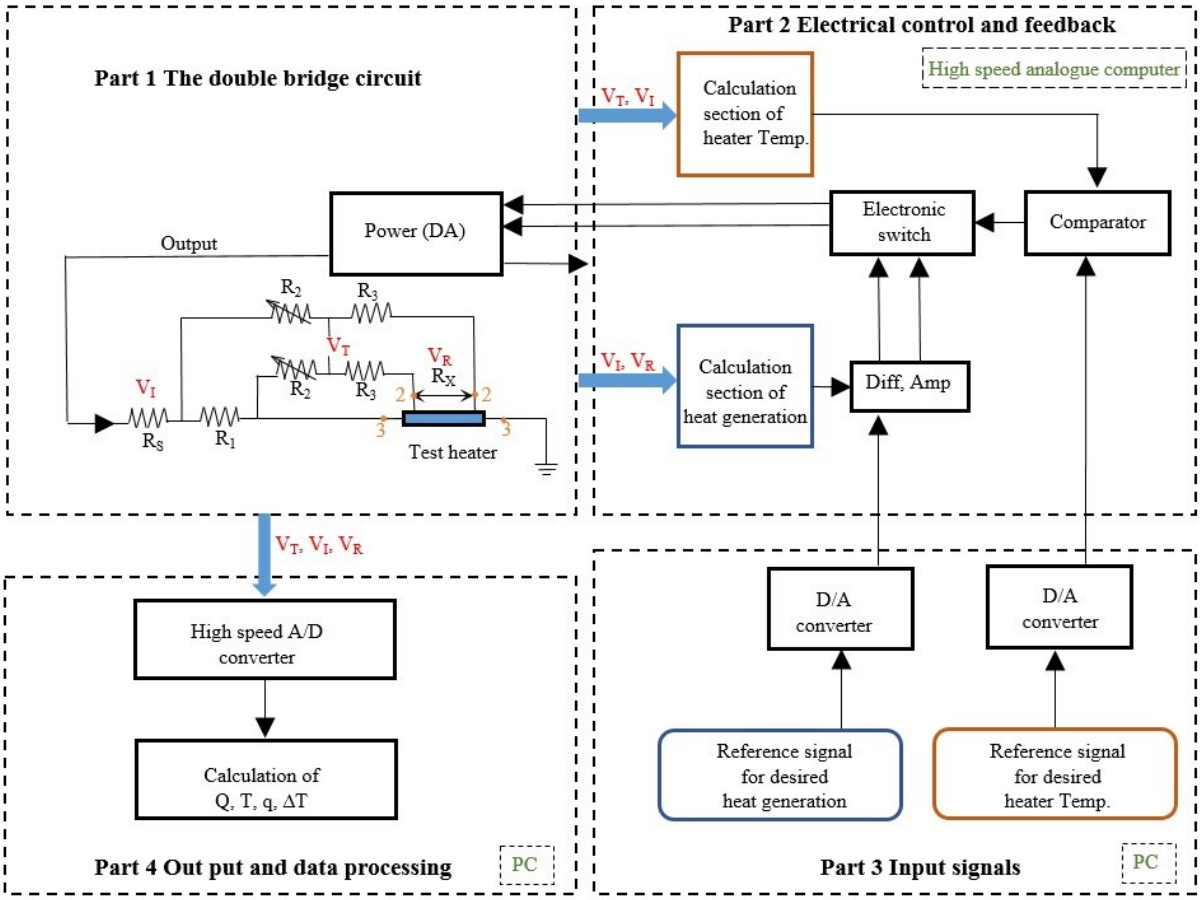

Figure 2.3 Electrical control and measurement circuit.

2.2.1 Heat input control system

The heat input to the test heater was generated from direct current by a changeable low-voltage power and the control system is shown in the part 2 of Figure 2.3. The input signals as the reference value of heat generation rate and the heater temperature were converted to analogue signals through a digital to analog (D/A) converter. When the initial power was added to test heater, the actual generated heat generation rate (analog signal)

could be calculated through a calculation section with the measured V_I and V_R, which are amplified through an amplifier. The actual heat generation rate was fed back to be compared with the reference value, so as to adjust the power output to minimize the differences between the actual value and the reference value. Moreover, the actual value of heater temperature (analog signal) was calculated through a calculation section with the measured V_T and V_I, and it was also used as a feedback signal to be compared with the corresponding reference value of heater temperature. Once the actual heat generation rate or the actual heater temperature of the test heater reaches the corresponding reference value set before, the current of the power supply is instantaneously intercepted by the electronic switch.

2.2.2 Measurement and output data processing system

As shown in the part 1 of Figure 2.3, the double bridge circuit is used for the temperature measurement of the test heater. It is a widely used indirect temperature measurement method with high accuracy for unknown electrical resistors below 1 ohm. As we known, resistors above about 1 ohm can be measured by simply using an ohmmeter or a Wheatstone bridge, for which the resistance of the connecting wires is negligible compared to the resistors. However, for the resistor is of less than 1 ohm, the resistance

of the connecting wires becomes not negligible. The double bridge circuit is designed to remove the effect of the resistance connecting wires or terminals with four terminals for the objective resistor. The connection of the four terminals of the test resistance (test heater) with double bridge circuit is shown in Figure 2.2 and Figure 2.3.

Electric equilibrium was taken at main fluid temperature for each experiment before the experiment beginning. When the experiment starts, the electric current, flows through the test heater, and the temperature of the test heater rises, then the equilibrium of double bridge circuit was broken. The output voltages of the bridge together with the voltage of drops across the potential taps of the heater across the standard resistance and gas temperature signal from the thermocouple which present the main fluid temperature are amplified and passed to the A/D converter of a computer. The data was processed by the computer. The converter is 16 bit A/D (synchronization 4 μs/4CH of sampling simultaneously, 1μs of conversion time for each channel).

The resistance of the test heater is given by the next equation.

$$R_x = \frac{R_1 R_3 + \frac{V_t}{I}(R_3 + R_2)}{R_2} \tag{2.1}$$

The average temperature of the test heater is obtained by calculating a previously calibrated resistance-temperature relation. The heat generation rate of the test heater is

given by the next expression.

$$\dot{Q} = V_R \frac{V_I}{R_S} \tag{2.2}$$

2.3 Experimental method and procedure

2.3.1 Temperature-resistance calibration for test heater

The application of platinum resistance for temperature measurement over a wide temperature range depends on the quasi-linear correlation of the temperature-resistance and differential sensitivity for $\partial T / \partial R$. The Callendar-Van Dusen equation is generally known as a valid correlation for the temperature-resistance relationship and is given as:

$$R = R_0(1 + \alpha T_a + \beta {T_a}^2) \tag{2.3}$$

Where, T_a is the average temperature, °C, R is the measured resistance at temperature of T_a, mΩ, α and β are temperature coefficients. Typically, industrial platinum resistance thermometers have nominal α and β values of about 3.98×10^{-3}, 5.88×10^{-7}, respectively.

In this experiment, the hand-made platinum test heaters were calibrated for the temperature range from 25 °C to 150 °C with a thermostatic bath. The calibrated correlations were list in the Table 2.1:

Table 2.1 Calibrated R-T correlations for the test heaters

Test heater	Effective length	Calibrated *R-T* correlations
Pitch number = 1	26.8 mm	$R = 6.360 \times (1 + 3.923 \times 10^{-3} T - 0.588 \times 10^{-6} T^2)$
Pitch number = 3	67.8 mm	$R = 16.833 \times (1 + 3.980 \times 10^{-3} T - 0.588 \times 10^{-6} T^2)$
Pitch number = 5	106.4 mm	$R = 26.861 \times (1 + 3.979 \times 10^{-3} T - 0.588 \times 10^{-6} T^2)$

2.3.2 Temperature measurement for test heater

The heat generation rates of the heater were controlled and measured by a heat input control system with a function of $\dot{Q} = Q_0 \exp(t/\tau)$. Where $\dot{Q}$ is heat generation rate, Q_0 is initial heat generation rate, t is time and τ is heat generation period. According to the exponential function, a shorter heat generation period will result in a higher increasing ratio of heat generation.

The average temperature of test heater T_a was measured by resistance thermometry using a double bridge circuit including the test heater as a branch [36, 37]. With the measured T_a of the test heater, the surface temperature of the test heater was calculated from following unsteady heat conduction equation of the plate by assuming the total

surface temperature to be uniform.

For the plate heater,

$$\frac{\partial T}{\partial t} = a\frac{\partial^2 T}{\partial x^2} + \frac{\dot{Q}}{\rho_h c_h} \tag{2.4}$$

Boundary conditions are as follows,

$$\left.\frac{\partial T}{\partial x}\right|_{x=0} = 0, \qquad -\lambda\left.\frac{\partial T}{\partial x}\right|_{x=\frac{\delta}{2}} = q$$

$$T_a = \frac{\int_0^{\delta/2} T dx}{\int_0^{\delta/2} dx} = \frac{2}{\delta}\int_0^{\delta/2} T dx \tag{2.5}$$

where, λ (W/mK) and α (m^2/s) are the thermal conductivity and thermal diffusivity.

The indeterminacy of the measurement of the heat generation rate, heat flux of the test heater and heat transfer coefficient were estimated to be 2.0%, 2.4%, and 4.4%, respectively. And the indeterminacy for the obtained heat transfer coefficients is estimated to be $\pm$ 2.5%.

2.3.3 Temperature measurement for fluid

Both inlet gas temperature of the test section, T_{in} and the outlet gas temperature, T_{out} were measured by K-type thermocouples. Since the differences between the inlet and outlet temperature are not significant, the bulk temperature of helium gas was calculated by average value of the inlet and out let gas temperature, as:

$$T_b = \frac{T_{in} + T_{out}}{2} \tag{2.6}$$

For the experiment is a transient process, the physical properties of the fluid were calculated based on the film temperature which is calculated by following equation:

$$T_f = \frac{T_s + T_b}{2} \tag{2.7}$$

Where, T_s and T_b are the test heater surface temperature, and the bulk gas temperature, respectively.

2.3.4 Flow velocity measurement

The gas flow rate was measured by a turbine flow meter which was set at the location before the gas flows into the test section. The gas flow velocity could be obtained from the following correlation:

$$\dot{m} = \rho \dot{V} = \rho \frac{1}{4} \pi D^2 U \tag{2.8}$$

$$U = \frac{4\dot{m}}{\rho \pi D^2} \tag{2.9}$$

2.3.5 Operating procedure

The experiment was conducted with the following procedure:

Before the test heater was put into the test section, a calibration for temperature-resistance correlation was completed in a thermostat, with a calibration range from room temperature up to 150 °C. A calibrated correlation for the test heater was obtained.

Next, the test heater was installed horizontally to the test section with both ends connected to two copper plates and then connected to the double bridge branch. Two fine platinum wires (50 μm-dia.) were spot welded close to the end parts of the twisted plate as potential conductors and then connected to the double bridge branch.

Then, the helium gas (99.9% purity) was filled to the test loop and maintained at anticipative pressure after the test loop being degassed by a vacuum pump. A piston compressor was used to circulate the flow in the test loop. There are two bypass branches for the test loop, one is parallel to the test section, another goes side by side with the compressor. By adjusting the two bypass valves in the bypass branches, the flowing could be sequentially lowered from maximum stream flow to desired values.

After the pressure and flow rate were confirmed to be stable at desired value in the loop, the electric current was supplied to the test heater with exponentially increasing heat generation rate controlled by the heat input control system, as shown in part 2 of Figure 2.3. Meanwhile, the test heater surface temperature and the heat flux accompanying the passage of the time were measured.

2.3.6 Basic equations

The heat flux through the surface of test heater, q (W/m^2), is calculated as follows.

$$q = \frac{\delta}{2}(\dot{Q} - \rho_h c_h \frac{dT_a}{dt}) \tag{2.10}$$

Where, c_h ρ_h and δ are specific heat, the density, and thickness of the test heater, respectively. $\dot{Q}$ (W/m^3) is the internal heat generation rate of heater, T_a (K) is the average temperature of test heater.

Surface temperature difference is defined as the difference between the average surface temperature of the twisted plate (T_{sa}) and the inlet gas temperature (T_∞), expressed as:

$$\Delta T = T_{sa} - T_\infty \tag{2.11}$$

Heat transfer coefficient, h, is defined as shown in the next equation.

$$h = q / \Delta T \tag{2.12}$$

2.4 Experimental conditions

The detailed experimental conditions are shown in Table 2.2. The transient heat transfer experimental data were measured for the periods of heat generation rate ranged from 35 ms to 14 s. The helium gas temperature was maintained at about 303 K under a

system pressure of around 500 kPa. Three test heaters with pitch numbers of 1, 3 and 5 (effective length 26.8 mm, 67.8 mm and 106.4 mm) were tested in the experiment. The 180 degree helical pitch size for the three test heaters was the same of 20 mm. The flow velocities ranged from 4 to 10 m/s with corresponding Reynolds numbers (Re) ranged from 2×10^3 to 3×10^4.

Table 2.2. Experimental conditions

Test fluid	Helium gas
Effective length	26.8 mm
Pitch number	1
Pitch size	20 mm
Period of heat generation rate	35 ms ~ 14 s
Gas temperature	303 K
System pressure	500 kPa
Flow velocity	4 ~ 10 m/s
Reynolds number	2000 ~ 30,000

2.5 Uncertainty analysis

The uncertainty analysis was done in a previous work (Shibahara M., Liu Q.S. and Fukuda K., 2016) [38]. The maximum uncertainties of heat generation rate, heat flux, and heat transfer coefficient were estimated to be 2.0%, 2.4%, and 4.4%, respectively. The measurement uncertainty analysis was carried out based on the ANSI/ASME performance test codes [39]. The maximum uncertainty of heat generation rate can be obtained by Eqs. (A1)- (A3).

$$\frac{B_{\dot{Q}}}{\dot{Q}} = \sqrt{\left(\frac{\partial \dot{Q}}{\partial V}\right)^2 \left(\frac{B_{V_R}}{V}\right)^2 + \left(\frac{\partial \dot{Q}}{\partial V}\right)^2 \left(\frac{B_{V_I}}{V}\right)^2} \tag{A1}$$

$$\frac{S_{\dot{Q}}}{\dot{Q}} = \sqrt{\left(\frac{\partial \dot{Q}}{\partial V}\right)^2 \left(\frac{S_{V_R}}{V}\right)^2 + \left(\frac{\partial \dot{Q}}{\partial V}\right)^2 \left(\frac{S_{V_I}}{V}\right)^2} \tag{A2}$$

$$\frac{U_{RSS,\dot{Q}}}{\dot{Q}} = \sqrt{\left(\frac{B_{\dot{Q}}}{\dot{Q}}\right)^2 + t_{95}\left(\frac{S_{\dot{Q}}}{\dot{Q}}\right)^2} \tag{A3}$$

where, $B_{\dot{Q}}$, $S_{\dot{Q}}$ and t_{95} are the basis of the heat generation rate, the precision index of the heat generation rate, and confidence level, respectively. B_V and S_V are the basis and precision index of the DC amplifier (Yokogawa, 3131). On the other hand, the maximum uncertainty of the heat flux can be obtained by Eqs. (A4)- (A6).

$$\frac{B_q}{q} = \sqrt{\left(\frac{\partial q}{\partial V}\right)^2 \left(\frac{B_V}{V}\right)^2 + \left(\frac{\partial q}{\partial T_a}\right)^2 \left(\frac{\overline{B_{T_a}}}{T_a}\right)^2} \tag{A4}$$

$$\frac{S_q}{q} = \sqrt{\left(\frac{\partial q}{\partial V}\right)^2 \left(\frac{S_V}{V}\right)^2 + \left(\frac{\partial q}{\partial T_a}\right)^2 \left(\frac{\overline{S_{T_a}}}{T_a}\right)^2} \tag{A5}$$

$$\frac{U_{RSS,q}}{q} = \sqrt{\left(\frac{B_q}{q}\right)^2 + t_{95}\left(\frac{S_q}{q}\right)^2} \tag{A6}$$

where, $\overline{B_{T_a}}$ and $\overline{S_{T_a}}$ are basis of the average temperature and precision index of the precision double bridge (Yokogawa, Type2752) for the temperature calibration, respectively. They can be expressed as follows:

$$\frac{\overline{B_{T_a}}}{T_a} = \sqrt{w_1^2\left(\frac{B_{V_T}}{V}\right)^2 + w_2^2\left(\frac{B_R}{R}\right)^2} \tag{A7}$$

$$\frac{\overline{S_{T_a}}}{T_a} = \sqrt{w_1^2\left(\frac{S_{V_T}}{V}\right)^2 + w_2^2\left(\frac{S_R}{R}\right)^2} \tag{A8}$$

where, w_1 and w_2 are weight coefficients as follows:

$$w_1 = \frac{U_{RSS,V}}{U_{RSS,V} + U_{RSS,R}} \tag{A9}$$

$$w_2 = 1 - w_1 \tag{A10}$$

where, $U_{RSS,V}$ and $U_{RSS,R}$ are uncertainties of the DC amplifier and the double bridge, respectively. They can be calculated by the following equations.

$$\frac{U_{RSS,V}}{V} = \sqrt{\left(\frac{B_{V_T}}{V}\right)^2 + \left(\frac{S_V}{V}\right)^2} \tag{A11}$$

$$\frac{U_{RSS,R}}{R} = \sqrt{\left(\frac{B_R}{R}\right)^2 + \left(\frac{S_R}{R}\right)^2} \tag{A12}$$

$$\frac{S_R}{R} = \sqrt{\frac{\sum_{k=1}^{N}(R_k - R_{LS,k})^2}{N-C}} \tag{A13}$$

where, B_R and S_R are the basis of the precision double bridge and precision index of the temperature calibration, respectively. N and C are a number of data and number of constant value for the least square (LS) method, respectively. Furthermore, the uncertainty of the heat transfer coefficient can be obtained by Eqs. (A14)- (A16).

$$\frac{B_h}{h} = \sqrt{\left(\frac{\partial h}{\partial q}\right)^2\left(\frac{B_q}{q}\right)^2 + \left(\frac{\partial h}{\partial \Delta T}\right)^2\left(\frac{B_{\Delta T}}{\Delta T}\right)^2} \tag{A14}$$

$$\frac{S_h}{h} = \sqrt{\left(\frac{\partial h}{\partial q}\right)^2\left(\frac{S_q}{q}\right)^2 + \left(\frac{\partial h}{\partial \Delta T}\right)^2\left(\frac{S_{\Delta T}}{\Delta T}\right)^2} \tag{A15}$$

$$\frac{U_{RSS,h}}{h} = \sqrt{\left(\frac{B_h}{h}\right)^2 + t_{95}\left(\frac{S_h}{h}\right)^2} \tag{A16}$$

where, $B_{\Delta T}$ and $S_{\Delta T}$ are the temperature difference between the surface temperature of the test heater and balk gas temperature and the precision index of the temperature difference, respectively. They can be expressed as follows.

$$\frac{B_{\Delta T}}{\Delta T} = \sqrt{\left(\frac{\overline{B_{T_a}}}{T_a}\right)^2 + \left(\frac{B_q}{q}\right)^2 + \left(\frac{B_{T_b}}{T_b}\right)^2} \tag{A17}$$

$$\frac{S_{\Delta T}}{\Delta T} = \sqrt{\left(\frac{\overline{S_{T_a}}}{T_a}\right)^2 + \left(\frac{S_q}{q}\right)^2 + \left(\frac{S_{T_b}}{T_b}\right)^2} \tag{A18}$$

2.6 Typical experimental results for one-pitch case

Figure 2.4 shows a typical experimental result of the time-dependence of heat generation rate,$\dot{Q}$ surface superheat, ΔT, and heat flux, q, at the period of 1.4 s. The effective length for the heater is 26.8 mm with only one pitch. The helical pitch size is 20 mm. The flow velocity is 10 m/s and gas temperature is 303 K. It can be seen that the surface temperature difference and heat flux increases exponentially as the heat generation rate increases exponentially.

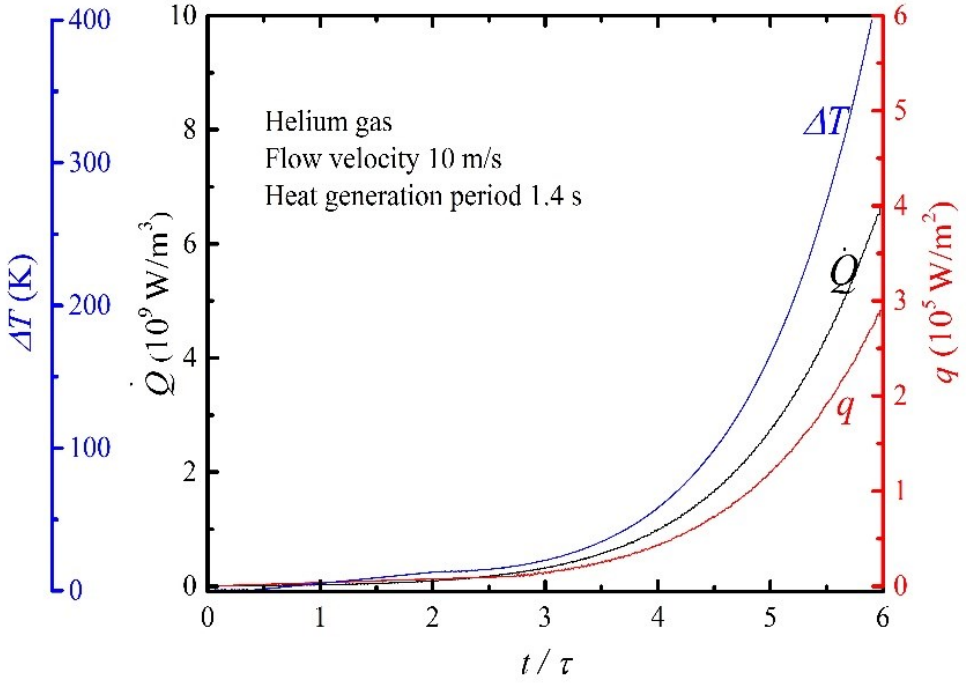

Figure 2.4 Time-dependence of $\dot{Q}$, q, and ΔT at 10 m/s.

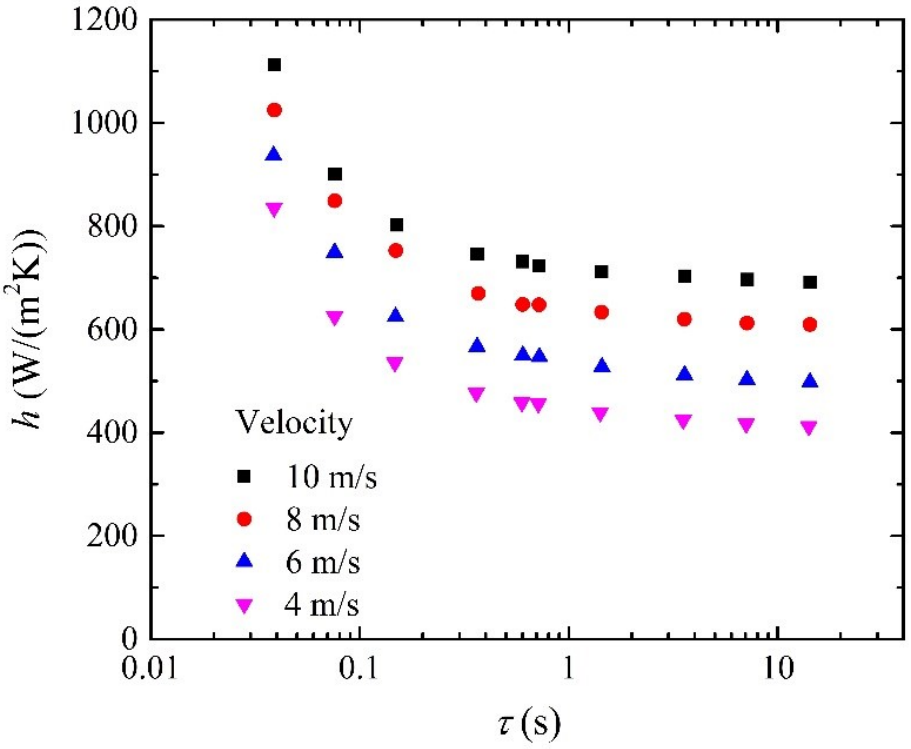

Figure 2.5 Effect of flow velocity on heat transfer coefficient at various periods.

The relation between the heat transfer coefficients and the periods of heat generation rate for the heater at various flow velocities was shown in Figure 2.5. The heat transfer coefficient increases with the increase of flow velocity. However, the increasing rate decreases. The heat transfer coefficient, h, becomes to approach asymptotic value at each velocity when τ is longer than about 1 s. On the other hand, when the period τ is shorter than about 1 s, h increases as τ shortens. It has been clarified in the early works that at extremely shorter period ($\tau < 100$ ms), the conductive heat transfer near the heater comes to govern the heat transfer process, and the heat transfer coefficient increases greatly with

shorter period in this region. When period τ is larger than about 1s, the heat transfer process turns to normal convective heat transfer through the thermal boundary layer influenced by the flow of helium gas. Therefore, in this study, the average value of heat transfer coefficients at periods larger than about 1s are taken as steady-state heat transfer coefficient.

As it is known that with the exponential increasing heat generation rate, the heater surface temperature will increase with time and then the thermal boundary layer thickness will increase. For higher heat generation rate with a shorter period, the increasing rate of heater surface temperature will be very fast. When the increasing rate of heater surface temperature is too fast for the thermal boundary layer to be fully developed, it is considered to be the transient state. For this state, the thermal boundary layer is not fully developed and it is thinner than the steady state. Thus, a higher heat transfer coefficient will be generated.

The relationship between the Nusselt number and the Reynolds number for various periods ranging from 1.4 s to 14 s with flow velocity ranging from 4 to 10 m/s was shown in Figure 2.6. Effective length of the twisted plate is 26.8 mm. As shown in the Nu_{st} /Pr $^{1/3}$ versus Re graph, the Nusselt numbers for quasi-steady state increases linearly with square root of Reynolds number. It can be correlated by the following equation.

$$Nu_{st} = 1.36\,\mathrm{Re}^{0.5}\,\mathrm{Pr}^{1/3} \tag{2.13}$$

Where, $Nu_{st} = h_{st} L/\lambda$, $\mathrm{Re} = UL/\upsilon$; h_{st} is quasi-steady state heat transfer coefficient, Pr is Prandtl number (about 0.68 in the range of this experiment).

By comparing to the experimental data of a flat plate [16], heat transfer coefficient for the twisted plate is about 40% higher. Thus, a heat transfer enhancement was considered to be generated by the twisted plate. To study the mechanism of heat transfer enhancement due to twisted structure, three dimensional numerical simulation is conducted for thermal hydraulic analysis later in this research.

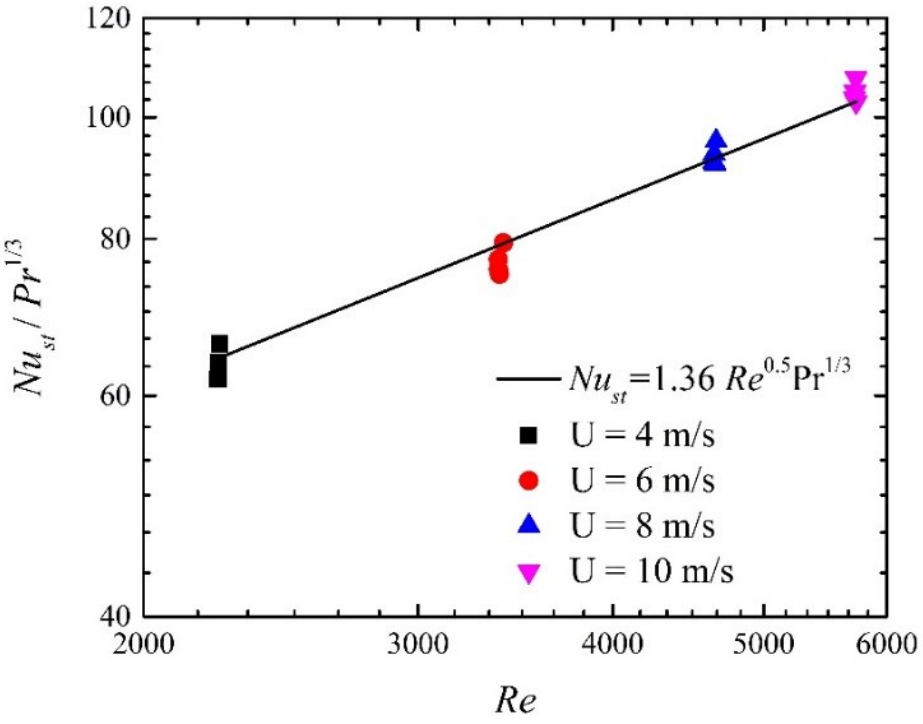

Figure 2.6 Quasi-steady heat transfer at various velocities.

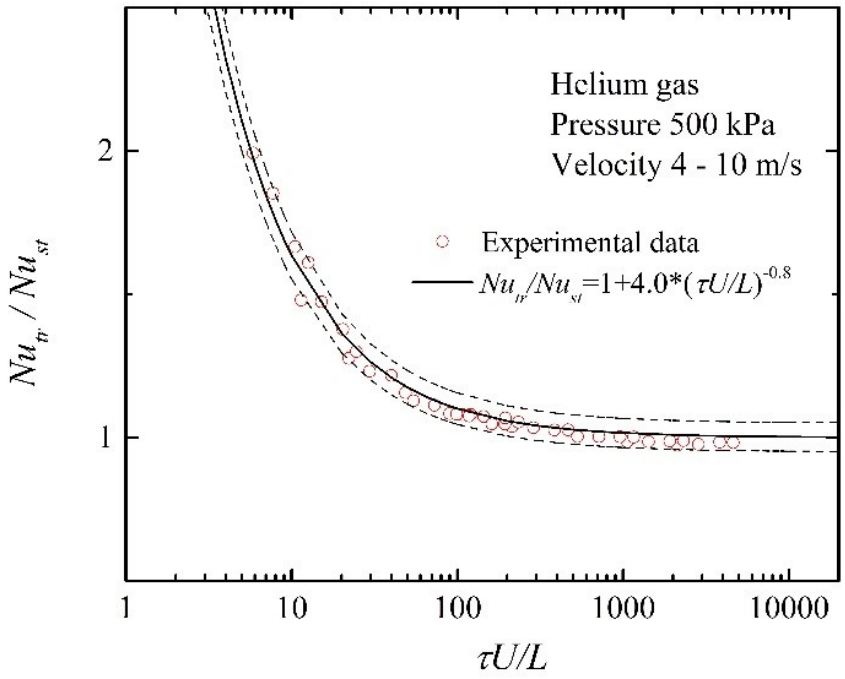

Figure 2.7 Correlation between transient and Quasi-steady Nu.

An empirical correlation of the ratio of transient Nusselt number to the quasi-steady-state Nusselt number can be obtained using a dimensionless period of τ^* ($\tau^* = \tau U/L$, U is flow velocity, and L is effective length). As shown in Figure 2.7, the empirical correlation for twisted plate can be obtained as follows.

$$Nu_{tr} = Nu_{st}[1+4.0\tau^{*-0.8}] \tag{2.14}$$

It can be seen that, the ratios of Nu_{tr} to Nu_{st} decrease to unity as the dimensionless period τ^* increases. The transient heat transfer approaches quasi-steady-state one for τ^*

larger than about 300. Dashed lines show the error bar of ± 5%.

The empirical correlation of Nusselt number for the twisted plate obtained from experimental data is compared with published correlations in Figure 2.8, as the laminar analytical solution (Holman, 2010) for plate [40], the Manglik and Bergles correlation for tube flow with twisted-tape insert [23] and the Dittus-Boelter correlation for tube flow [41]. The Manglik and Bergles correlation was obtained for Re ranged from 300 to 30000. The twist ratio y (y=H/W, H is 180 degree twist pitch, W is width) of 3 to 6. By comparing the Nu for the twisted plate with flat plate, it is about double value. When we compare the experimental data with Manglik and Bergles correlation, it is also much larger. It is because the experimental result for Nu in this study is for the twisted plate, while in the Manglik and Bergles correlation, the Nu is for the tube with twisted plate as inserts.

$$Nu_L = 0.664\,\mathrm{Re}_L^{0.5}\,\mathrm{Pr}^{1/3} \qquad \text{Plate (Laminar)} \qquad (2.15)$$

$$Nu_L = 0.106\left(y^{-0.5}\left[1+\left(\frac{\pi}{2y}\right)^{0.5}\right]\mathrm{Re}\right)^{0.767}\mathrm{Pr}^{0.3} \qquad \text{Manglik and Bergles} \qquad (2.16)$$

$$Nu = 0.023\,\mathrm{Re}^{0.8}\,\mathrm{Pr}^{0.4} \qquad \text{Dettus-Boelter} \qquad (2.17)$$

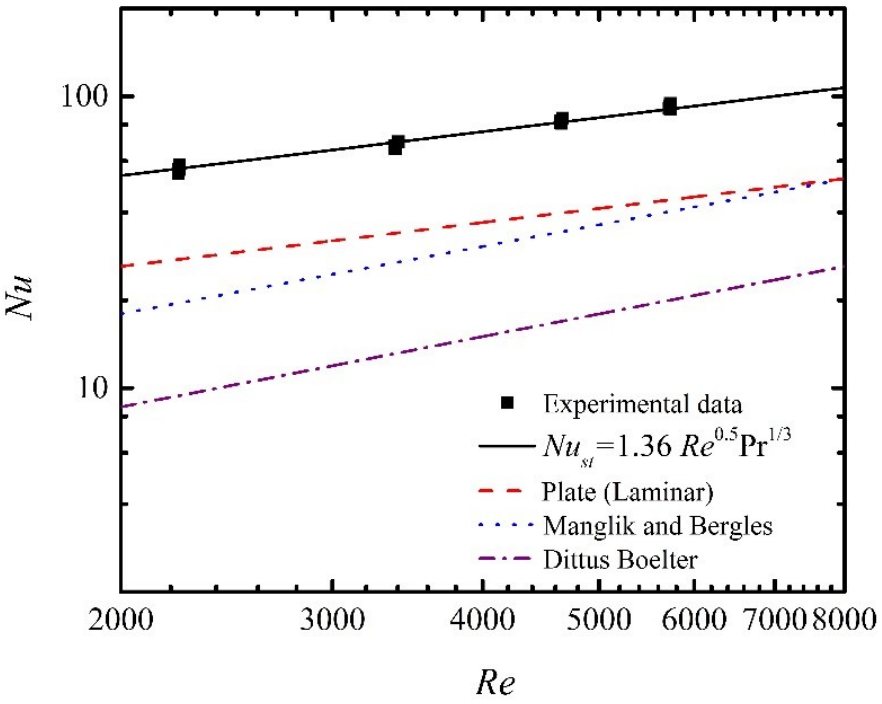

Figure 2.8 Comparison of experimental data with published correlations.

Chapter III

Numerical Method and Validation

3.1 Simulation model

Three-dimensional model was built with necessary simplification. Electricity wire is omitted in the model as it is thin and very little influence will be generated for the flow field. To ensure the flow to be fully developed, inlet and outlet channel length is set to be ten times of the tube diameter. Forced convection transient heat transfer for helium gas flowing over twisted plate with exponentially increasing heat input ($\dot{Q} = Q_0 \exp(t/\tau)$) was numerically calculated. ANSYS FLUENT 14 was used in this numerical solution. For the fluid, mass, momentum and energy conservation equations take the following forms (Reynolds Averaging), respectively [42].

$$\frac{\partial u_i}{\partial x_i} = 0 \tag{3.1}$$

$$\frac{\partial u_i}{\partial t} + \frac{\partial (u_i u_j)}{\partial x_j} = -\frac{1}{\rho}\frac{\partial p}{\partial x_i} + \nu \frac{\partial^2 u_i}{\partial x_j^2} - \frac{\partial}{\partial x_j}(\overline{u_i' u_j'}) \tag{3.2}$$

$$\rho \frac{\partial T}{\partial t} + \frac{\partial}{\partial x_i}(\rho u_i T) = \frac{\partial}{\partial x_j}\left[(\frac{k}{c_p} + \frac{\mu_t}{\mathrm{Pr}_t}) \frac{\partial T}{\partial x_j} \right] \tag{3.3}$$

The instantaneous velocity is expressed as $U_i = u_i + u_i'$, u_i is the ensemble-averaged velocity, and u_i' is fluctuating velocity. Pr_t is the turbulent Prandtl number, the default value in ANSYS Fluent is 0.85.

The turbulent heat flux is solved by the eddy-diffusivity model (contained in the Reynolds averaging energy equation) as follows [43]:

$$\rho\overline{u_i' T'} = -\frac{\mu_t}{\mathrm{Pr}_t}\frac{\partial T}{\partial x_i} \tag{3.4}$$

where, μ_t is the eddy (or turbulent) viscosity.

For the twisted plate, the energy conservation equation takes the following form.

$$\rho\frac{\partial(h_s)}{\partial t} = \nabla\cdot(k\nabla T) + \dot{Q} \tag{3.5}$$

Internal heat source: $\dot{Q} = Q_0 \exp(t/\tau)$, where, $\dot{Q}$ is heat generation rate, W/m^3, Q_0 is initial heat generation rate, W/m^3, t is time, s, and τ is period of heat generation rate or e-fold time, s.

Boundary Conditions:

at heater surface,

$$u = v = w = 0 \tag{3.6}$$

$$T_s\big|_{solid} = T_s\big|_{fluid} \tag{3.7}$$

$$q_s\big|_{solid} = q_s\big|_{fluid} \tag{3.8}$$

at the wall of channel,

$$u = v = w = 0 \tag{3.9}$$

$$T_w = T_\infty \tag{3.10}$$

In this study, turbulence models such as standard k-ε model, k-ω model and Reynolds Stress Model (RSM) were compared to experimental results. The convection term was discretized using the second order upwind scheme, and the linkage between the velocity and pressure was computed using the SIMPLE algorithm. The Enhanced Wall Treatment model was chosen for the near-wall modeling method because it combines the use of a blended law-of-the-wall and a two-layer zonal model and generally requires a fine near-wall mesh that is capable of solving the viscous sub-layer.

3.2 Mesh validation

Hexahedral grids are used for the three dimensional model with refined boundary layers. In the flow field, hexahedral grids are generated along the twisted plate with a very small twisting ratio. The helical pitch is 20 mm for 180 twisting degree and 120 layers are put along it as 1.5 degree for a layer. The mesh of the twisted heater is shown in Figure 3.1 and 6 layers were put in the 0.1 mm thickness direction. The dimensionless distance

y^+ ($\equiv \rho u_\tau y / \mu$) was considered. To ensure the mesh quality, the first near-wall node is placed at $y^+ \approx 1$.

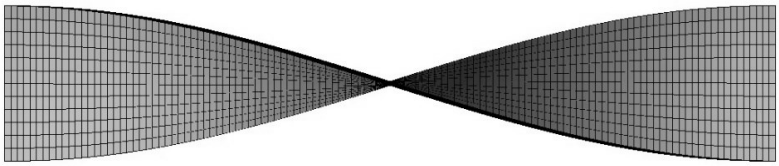

Figure 3.1 Mesh of the heater.

Finer mesh with smaller twisting degree for the twisted plate and the flow field are used to confirm the grid convergence. The total grid numbers increases from about 0.5 million to 1.2 million, a cross section view is shown in Figure 3.2. Figure3.2 (a) shows the current mesh, and a finer mesh with more layers in the boundary layer, the fluid area and the solid area is shown in Figure 3.2 (b). Three dimensional numerical simulation results for the two mesh were compared. Difference for total heat flux and temperature difference between the two mesh is about 0.05%. This indicates that the current mesh is fine enough for the calculation.

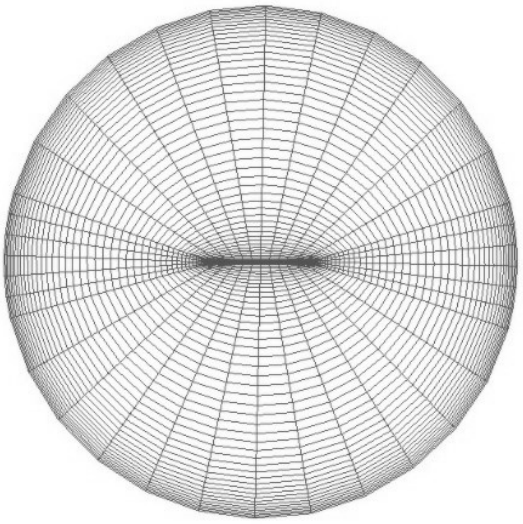

(a) Current mesh

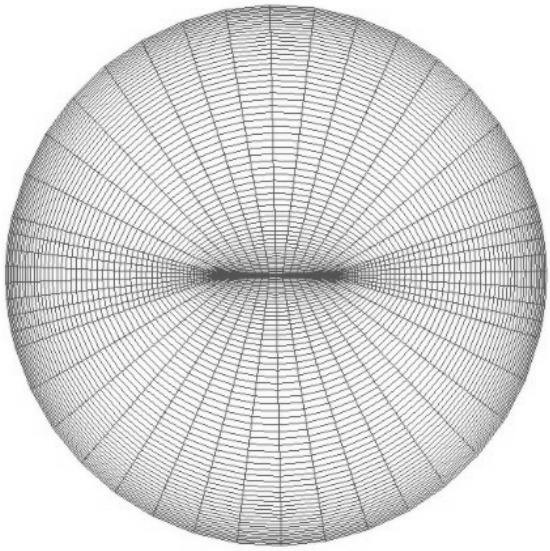

(b) Finer mesh

Figure 3.2 Cross section view of the mesh for three dimensional model.

3.3 Turbulence model

A validation study for turbulence model is conducted by comparing three kinds of

typical turbulence models as the Standard k-ε model (Launder and Spalding, 1972) [44], the k-ω model and the Reynolds Stress Model (RSM) with experimental data. The comparison for temperature difference at velocity of 10 m/s is shown in Figure 3.3 (a). The heat generation period τ is about 1.4s. As can be found, the temperature difference increases exponentially since the heat generation is increased with exponential function. In general, simulation results of the three models match the experimental data very well. When enlarge the figure and focus on the temperature difference range from 200 K to 300 K, the k-ω model is found to be a little lower than the other two models, shown in Figure 3.3 (b). The Standard k-ε model and RSM almost show no difference and both match the experimental data very well. Therefore, the RSM and Standard k-ω model are considered to be more suitable for the higher velocity simulation than the k-ω model.

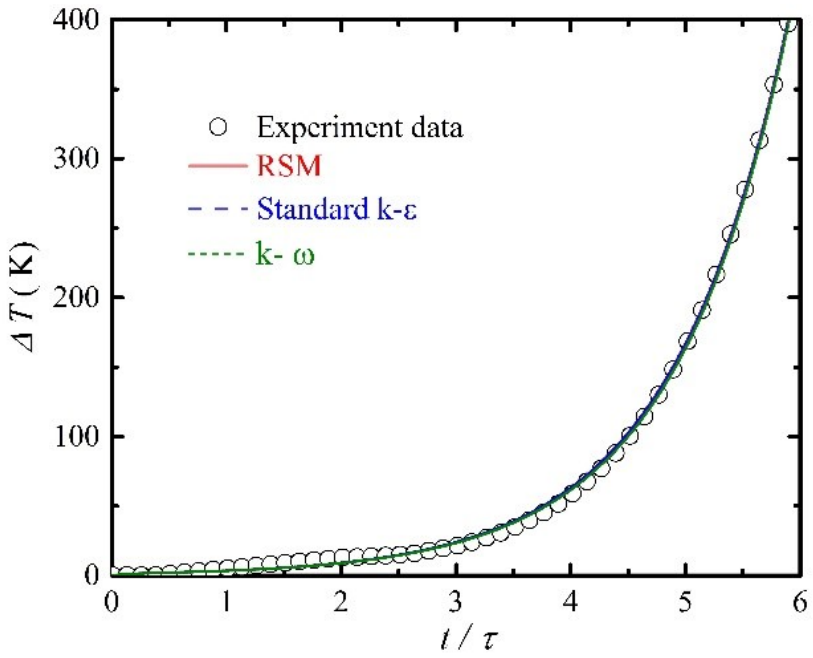

(a)

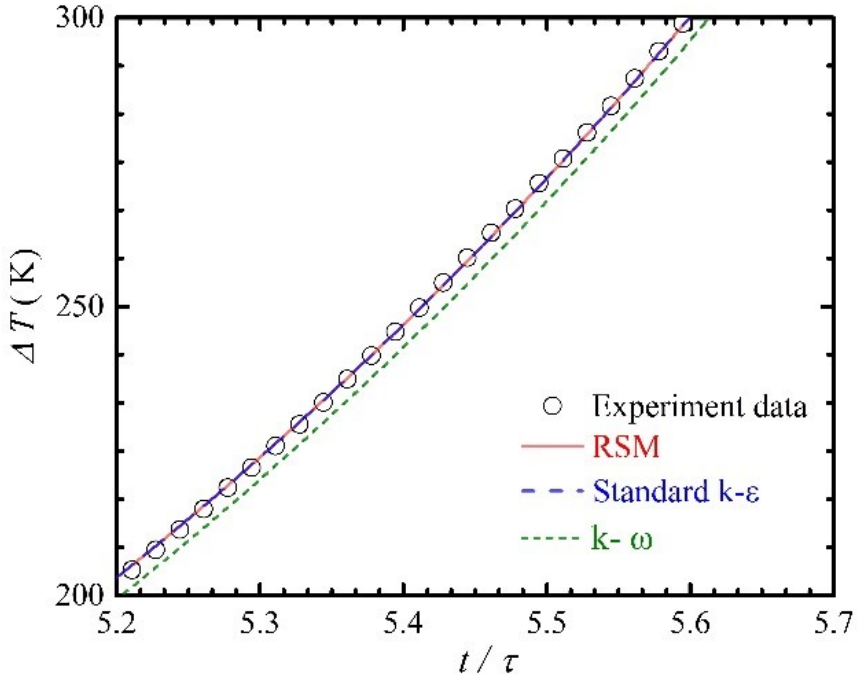

(b)

Figure 3.3 Comparison of temperature difference with experimental data at flow velocity of 10 m/s.

While for the lower velocity of 4 m/s, flow in the tube is more near laminar region. Validation study is also conducted to ensure the applicability of these models. The heat generation period τ is about 1.4s. As shown in Figure 3.4 (a), generally the simulation result for temperature difference of the three different models match the experimental data well which increases exponentially. Though, after t/τ larger than about 3, the simulation result is a little higher than experimental data. An enlarged figure for temperature difference range from 100 K to 300 K is shown in Figure 3.4 (b). It can be clearly seen that simulation results for three models are quite close and they are all a little higher than experimental result. The differences are within 5%.

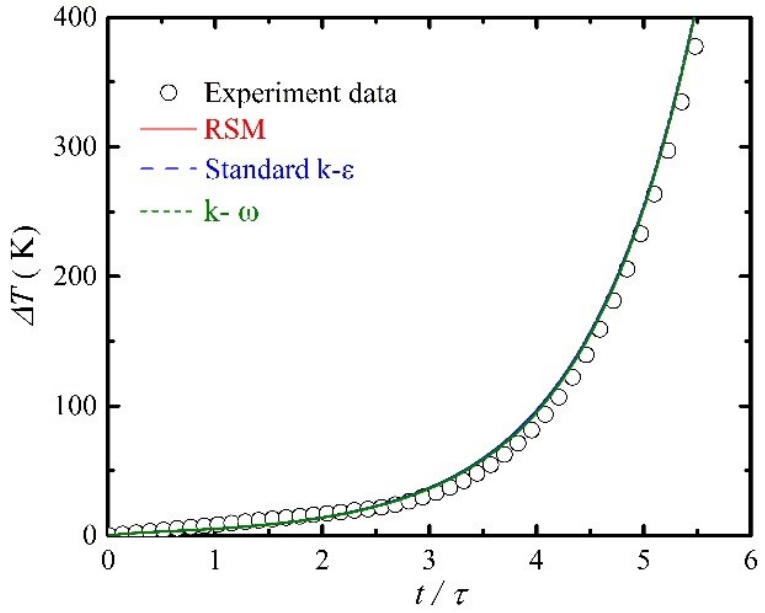

(a)

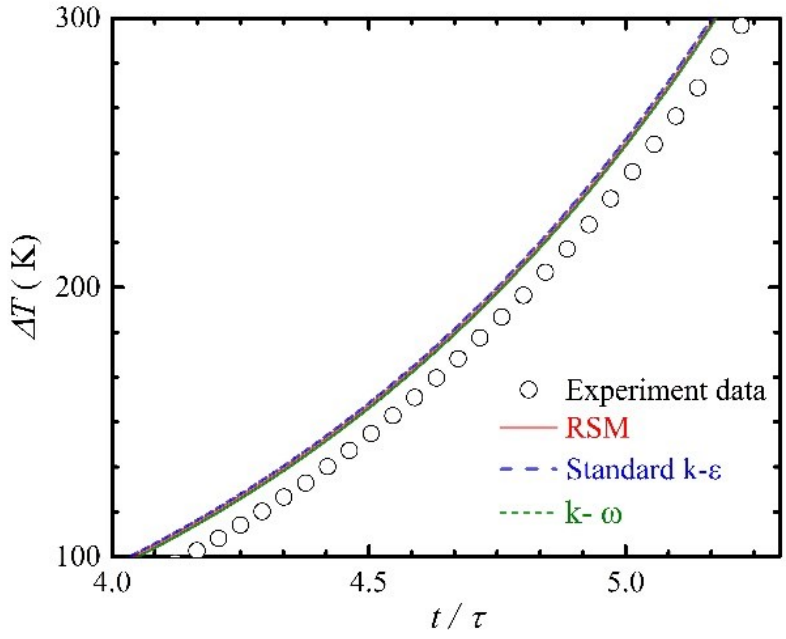

(b)

Figure 3.4 Comparison of temperature difference with experimental data at flow velocity of 4 m/s.

As can be concluded from the model validation study that all of the three models are considered to be acceptable for Re ranged from 2000 to 8000. Though for higher flow velocity the k-ω model is of a little difference and for lower flow velocity the simulation results have a difference of about 5% by comparing to the experimental data. The Standard k-ε model and RSM are considered to be more suitable for the higher flow velocity. Since the RSM abandoned the isotropic eddy-viscosity hypothesis, it closes the Navier-Stokes equations by solving transport equations for the Reynolds stress and another equation for the dissipation rate. Thus, the RSM accounts for the effects of streamline curvature, swirl, rotation, and rapid changes in strain rate in a more rigorous manner. Therefore, in this study RSM is more recommended for this twisted structure simulation.

3.4 Simulation results

3.4.1 Simulation results for quasi-steady state

As mentioned before, when the increasing rate of heater surface temperature is too fast for the thermal boundary layer to be fully developed transient heat transfer phenomena will occur. Higher heat transfer coefficient could be acquired due to the not fully developed thermal boundary layer. However, numerical simulation for the transient state is still very difficult as little research has been conducted and the empirical correlations were not well developed. Normal turbulence models such as the Standard k-

ε model, the k-ω model and RSM treat the near wall boundary layer with wall functions or near wall treatment and these near wall solutions are all based on fully developed thermal boundary layer under certain conditions.

In this study, numerical simulation for quasi-steady state heat transfer is conducted at the heat generation period of about 1.4 s. Figure 3.5 (a) and (b) shows a typical comparison of simulation results with experimental data at velocity of 10 m/s. The gas temperature is 303 K. The effective length used for the simulation is 26.8 mm, same as the experimental condition. It can be seen that the heat flux increases exponentially as the heat generation rate increases with exponential function and the simulation result for heat flux matches experimental data well. Simulation results for heat flux at other flow velocities also match experimental data well, with a difference within 3%.

Since the simulation results of heat flux and temperature difference ΔT both match experimental data well, heat transfer coefficient calculated by $h = q / \Delta T$ was considered to be able to predict the experimental result. A comparison for heat transfer coefficient at various flow velocity is shown in Table 3.1. The heat generation period is 1.4 s. Simulation results of quasi-steady state heat transfer coefficient matched experimental data well. Maximum error occurs at the lowest flow velocity of 4 m/s of 5%.

Therefore, it can be concluded that, numerical simulation results predicts

experimental data well even for the lowest velocity which is near laminar region, and with higher flow velocity a better match between simulation results and experimental data could be obtained within this range.

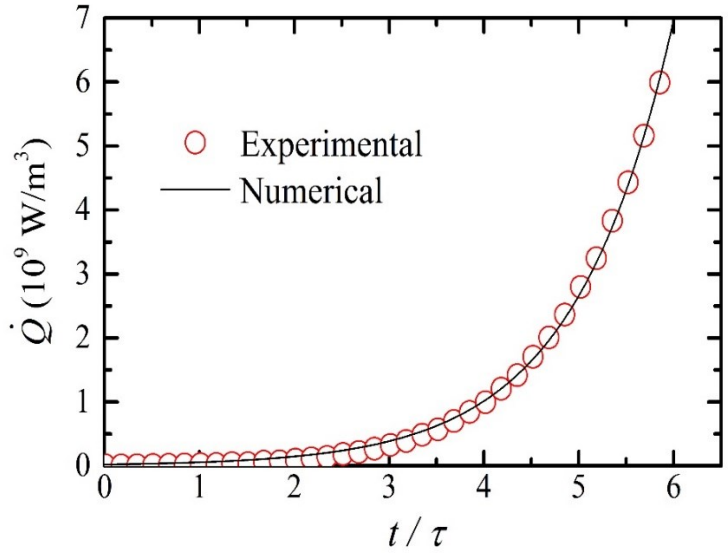

(a) $\dot{Q}$

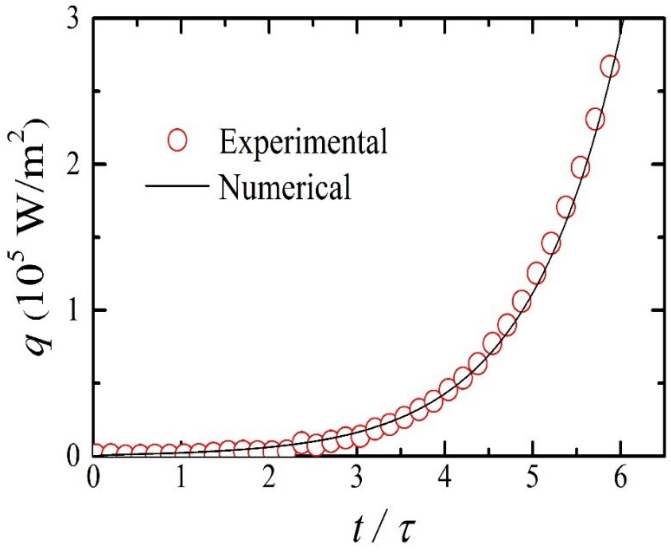

(b) q

Figure 3.5 Comparison of simulation results with experimental data.

Table 3.1 Comparison of simulation results of quasi-steady state heat transfer coefficient with experimental data under various velocities.

Flow velocity	$h_{Experimental}$, W/(m^2 · K)	$h_{Numerical}$, W/(m^2 · K)	Error
U=4 m/s	439.1	413.8	5.0%
U=6 m/s	527.4	518.2	1.7%
U=8 m/s	633.4	611.0	3.5%
U=10 m/s	712.2	689.6	3.3%

3.4.2 Difference in heat transfer between twisted plate and flat plate

As is known that heat transfer enhancement can be generated by using twisted plate instead of a flat plate. To study the difference between the two structures, a flat plate with same size of the twisted plate is numerically simulated at the period of 1.4 s and the flow velocity of 10 m/s. The flow time is at t/τ = 3. The comparison of twisted plate and flat plate for heat transfer coefficient distribution is shown in Figure 3.6.

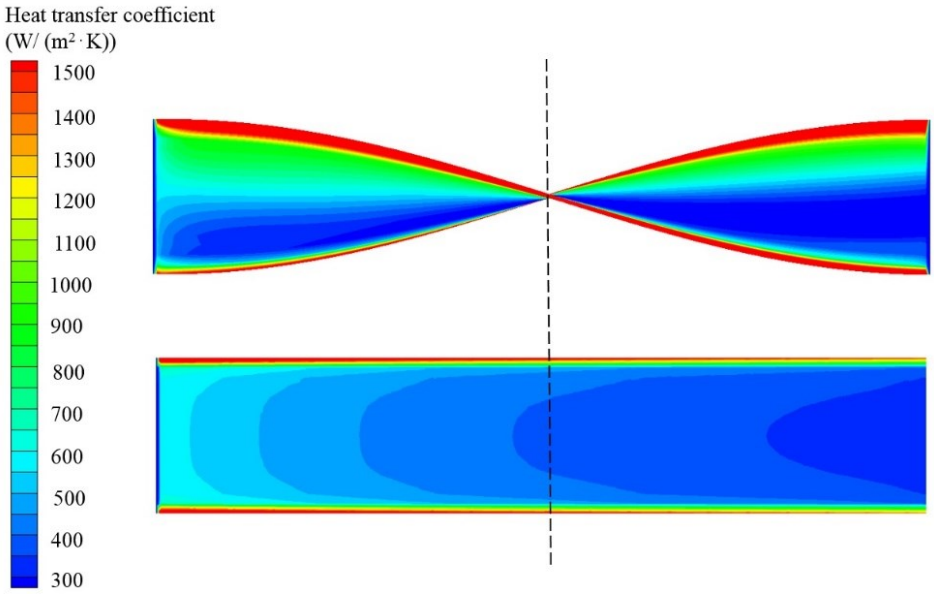

Figure 3.6 Surface heat transfer coefficient distribution for twisted plate and flat plate.

For twisted plate, a larger heat transfer coefficient was generated at the location facing the flow. The highest heat transfer coefficient exists in both sides of twisted plate where the thermal boundary thickness is very thin. In the width direction larger gradient exist for the heat transfer coefficient of the twisted plate than the flat plate. This kind of distribution is considered as a result of the flow distribution and larger heat transfer coefficient was generated due to the crash between helium gas and the twisted surface. For flat plate, heat transfer coefficient decreases along the length direction. In the width direction, heat transfer coefficient increases from the center to the side. Highest heat transfer coefficient also occurs at both sides of the width direction.

Therefore, it can be concluded that with different structure the heat transfer

coefficient distribution will be greatly changed. In the width direction, a larger gradient of heat transfer coefficient exist for the twisted plate than that for the flat plate. While in the length direction, the decreasing ratio of heat transfer coefficient for flat plate is much larger than that for the twisted plate. Moreover, larger heat transfer coefficient is obtained at the sides of twisted plate than the flat plate, as the red part shown in Figure 3.6. The average heat transfer coefficient for the twisted plate is 48.7% higher than that of the flat plate based on the simulation result.

Figure 3.7 (a), (b) and (c) show the cross sections of temperature distribution at the middle of the heater length as the dashed lines shown in Figure 3.6. The flow time is at $t/\tau = 3$. Figure 3.7 (a) shows the thermal boundary for flat plate at coolant flow velocity of 10 m/s. Figure 3.7 (b) and (c) shows the thermal boundary layer for twisted plate at typical velocities of 4 m/s and 10 m/s. As shown in Figure 3.7, there exists a curve distribution for the thermal boundary layer thickness along the width direction of the twisted plate while for the flat plate thermal boundary layer is almost uniform. This kind of thermal boundary layer thickness distribution matches the heat transfer coefficient distribution in Figure 3.6. Higher heat transfer coefficient occurs at this side (edge) of the twisted plate where thinner thermal boundary layer thickness exists. By comparing the Figure 3.7 (b) and (c) it can be found that the thermal boundary layer distribution looks

alike and with a lower velocity, the thermal boundary layer is thicker. Which has negative impact on heat transfer and thus leads to higher temperature for the twisted plate.

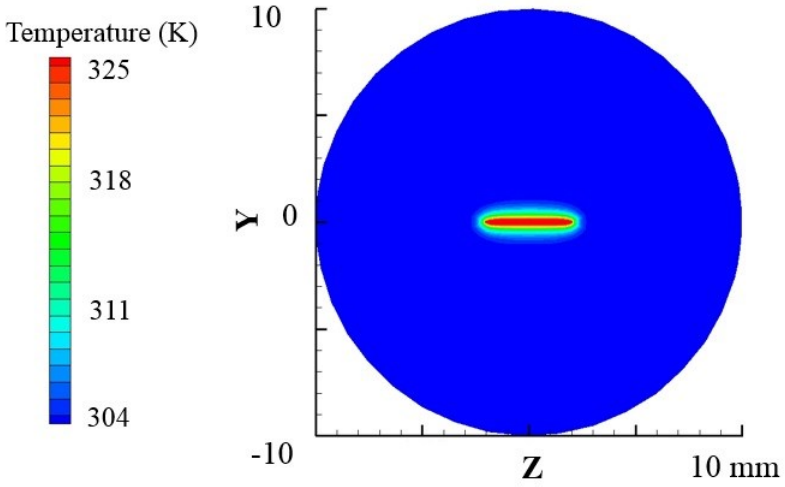

(a) Flat Plate (U = 10 m/s)

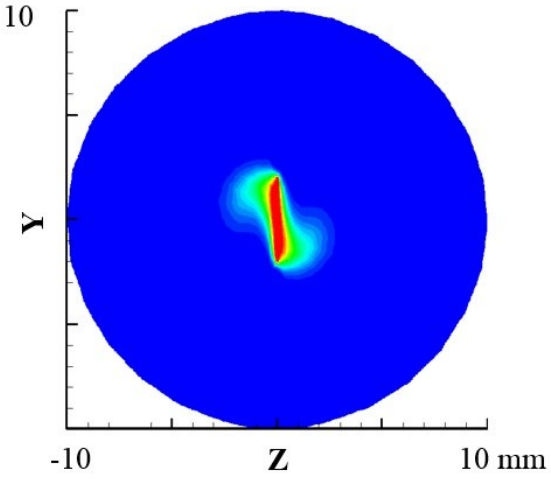

(b) Twisted plate (U = 4 m/s)

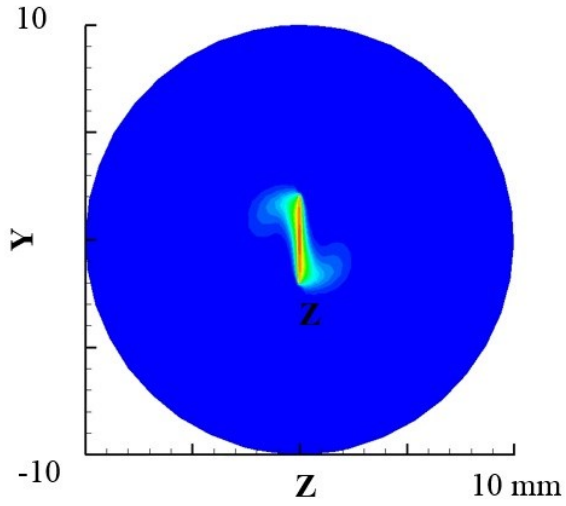

(c) Twisted plate (U = 10 m/s)

Figure 3.7 Cross section view of temperature distribution for twisted plate and flat plate.

For flat plate, the flow velocity is along the axial direction and in the radial direction it is almost zero. While for the twisted plate a radial velocity is generated due to the twisted structure. A cross section view for velocity vector distributions around the twisted plate under typical velocities at middle plane are shown in Figure 3.8 (a) and (b). The flow directions around twisted plate are indicated by these arrows. Arrow length show the velocity magnitude and color map refers to the Z-direction velocity.

As can be seen from Figure 3.8, a swirl flow is generated around the twisted plate and with a higher coolant flow velocity the radial velocity will also be higher. These radial velocities will contribute to the velocity magnitude and lead to a heat transfer enhancement. By comparing to the thermal boundary layer shown in Figure 3.7 (b) and (c), it can be found that a thinner thermal boundary layer occurs at the location where larger radial velocity is generated by the swirl flow. Moreover, larger heat transfer

coefficient is obtained at the sides of twisted plate than the flat plate where the radial velocity is vertical to the twisted plate. It is considered that this vertical flow will lead to better thermal mixing in the boundary layer around the plate. Therefore, it can be concluded that velocity in the radial direction which is also called as a "secondary flow" will contribute to the thermal mixing and increase the turbulence intensity thus lead to heat transfer enhancement.

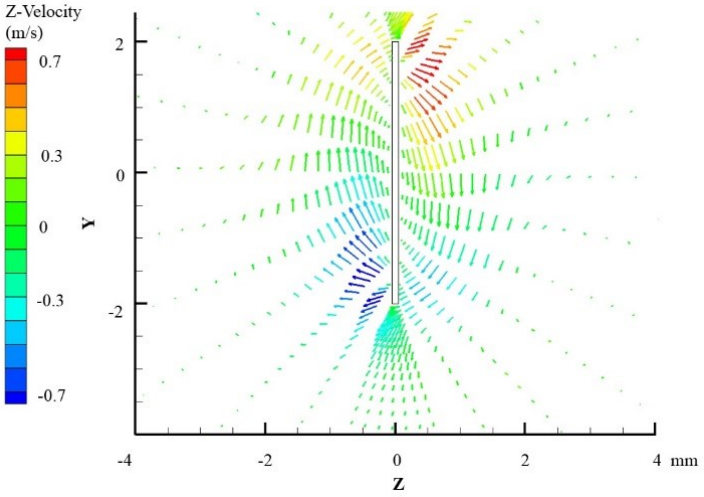

(a) U = 4 m/s

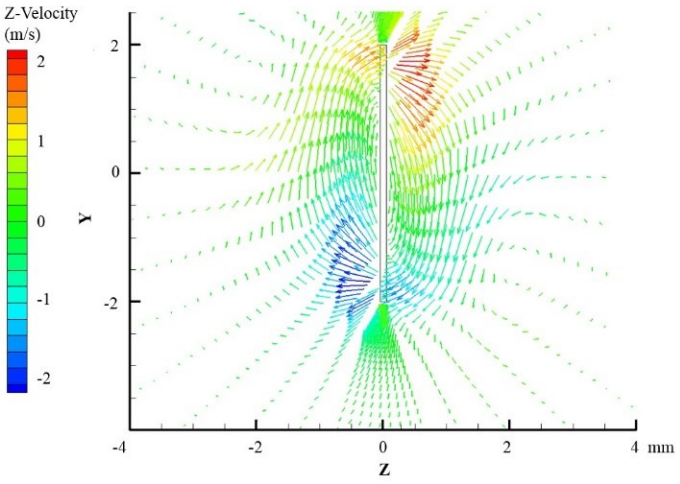

(b) U = 10 m/s

Figure 3.8 Cross section view for velocity vector around the twisted plate.

A cross section view for turbulence intensity ($I = u' / u_{avg} = 0.16(\mathrm{Re}_{D_H})^{-1/8}$, u' is root-mean-square of the velocity fluctuations, u_{avg} is the mean flow velocity, Re_{D_H} is the Reynolds number based on the pipe hydraulic diameter D_H) distributions around the twisted tape under typical flow velocities at middle plane was compared in Figure 3.9 (a) and (b). As can be found that higher turbulence intensity was generated around the twisted plate according to the swirl direction. For higher velocity of 10 m/s, a higher turbulence intensity was generated more near the heater surface by comparing to a lower velocity of 4 m/s due to the difference in velocity layer distribution.

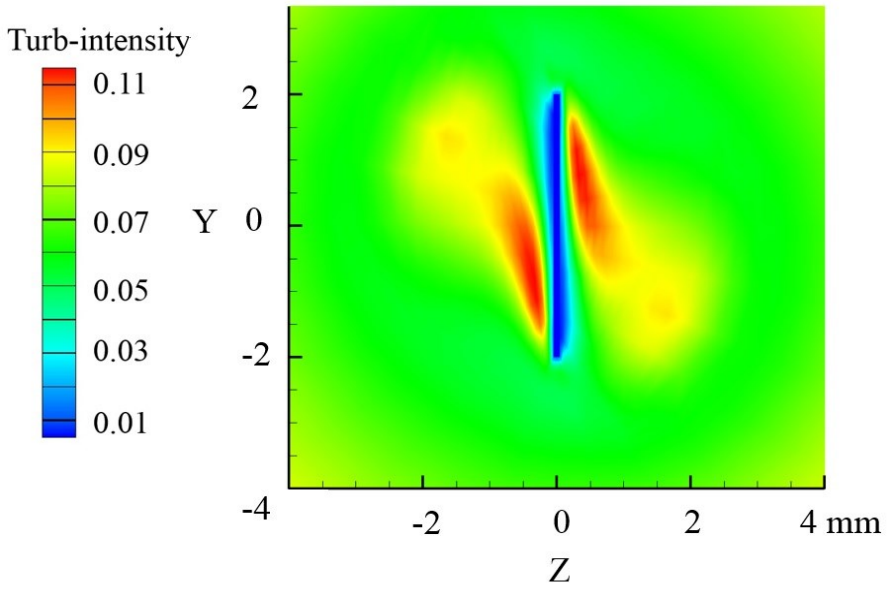

(a) U = 4 m/s

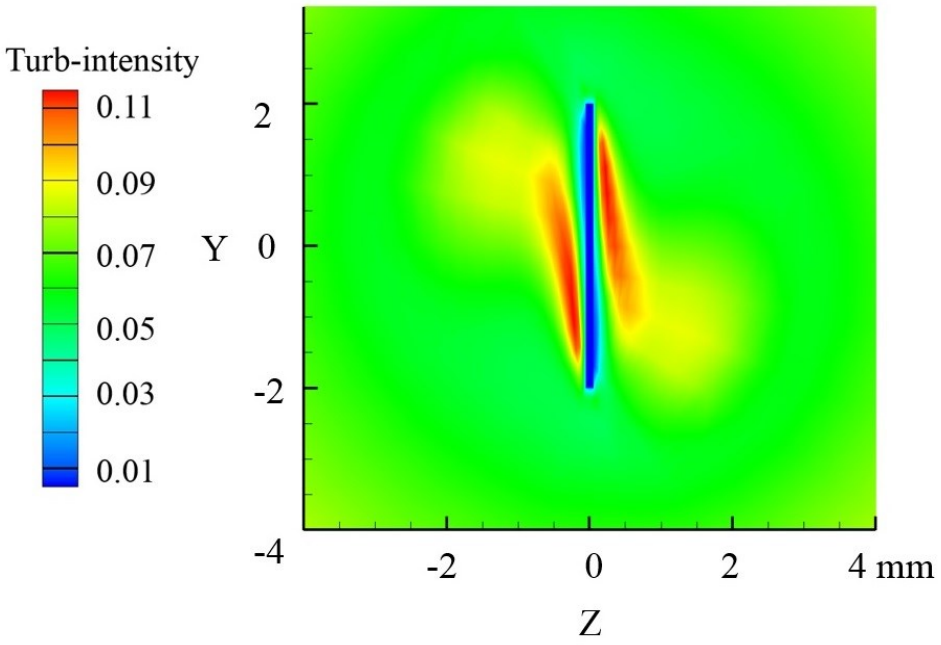

(b) U = 10 m/s

Figure 3.9 Cross section view for turbulence intensity around the twisted plate.

3.5 Summary

In this section a 3D numerical study was conducted for heat transfer process of the twisted plate with a single pitch and the results of three typical turbulence models were compared with experimental data. Numerical simulation results were obtained for average surface temperature difference, heat flux and heat transfer coefficient of the twisted plate and showed reasonable agreement with experimental data. Based on the numerical simulation, mechanism of local heat transfer coefficient distribution was clarified. A comparison of the twisted plate and flat plate was conducted to show the

difference in heat transfer coefficient distribution.

Chapter IV

Heat Transfer Characteristics of Twisted Plate

The shell-and-tube heat exchangers which are usually designed as helically arranged bundles were the first used intermediate heat exchanger (IHX) in the High Temperature Engineering Test Reactor (HTTR) of Japan. Due to the high heat generation rate of the VHTRs, the IHXs used to remove the heat has to be carefully designed. Various kinds of heat transfer enhancement technologies are under developing in order to reduce space, weight and material cost of the IHXs. Twisted plates are often adopted to enhance heat transfer in tube flows as turbulence promoters.

In this section, a series of twisted plates with different pitch sizes and a flat plate with the same width, length and thickness were numerically studied. The simulation results of heat transfer coefficients for the twisted plates and a flat plate were compared to clarify the effect of twisted structure on transient heat transfer. In addition, the effect of heater length was taken into consideration. A series of twisted plate with different length was experimentally and numerically studied to clarify the effect of heater length on transient heat transfer. The heat generation rate of the twisted plate was increased with an exponentially increasing function. The heat flux, surface temperature difference and heat transfer coefficient were obtained under various periods and velocities.

A 3D transient simulation were carried out by ANSYS FLUENT 14.0 code to get the temperature distribution, velocity distribution and heat transfer coefficient. Effect of heater length on heat transfer was discussed based on the experimental data and simulation results. Additionally, local heat transfer coefficient along the twisted plate was also investigated.

4.1 Influence of velocity on heat transfer

The relation between the heat transfer coefficients and the periods of heat generation rate for the heater at various flow velocities was shown in Figure 4.1. In experiment research the heat transfer coefficient approach constant values from higher initial values when the time passes over a certain time of about 2 to 4 times of the period ($t/\tau > 2 \sim 4$) according to different periods. And the constant value of heat transfer coefficient, h is plotted as a single point in Figure 4.1. The heater is the one with effective length of 67.8 mm (three helical pitches). The heat transfer coefficient increases with the increase of flow velocity. However, the increasing rate decreases. The heat transfer coefficient, h, becomes to approach asymptotic value at each velocity when τ is longer than about 1 s. On the other hand, when the period τ is shorter than about 1 s, h increases as τ shortens.

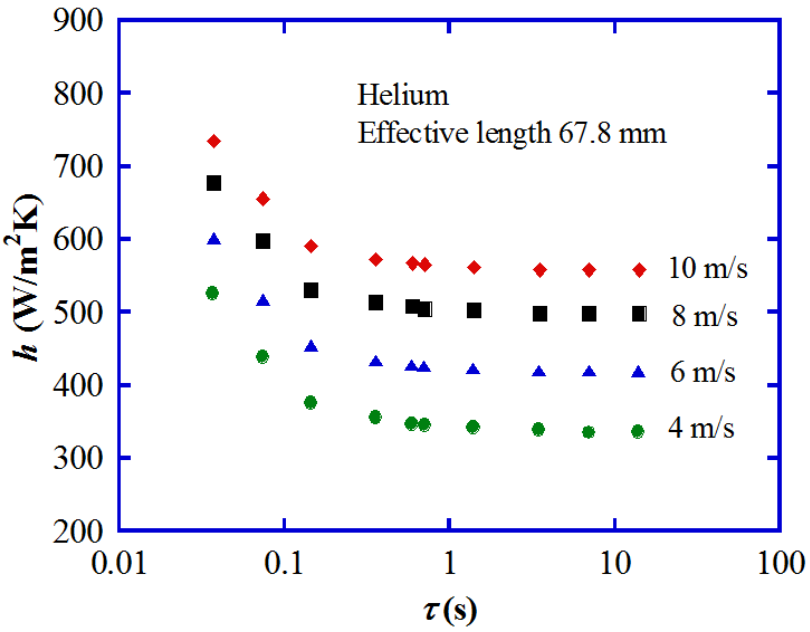

Figure 4.1. Effect of flow velocity on heat transfer coefficient at various periods.

It has been clarified in the early works that at extremely short period (τ < 100 ms), the conductive heat transfer near the heater comes to govern the heat transfer process, and the heat transfer coefficient increases greatly with shorter period in this region. When period τ is larger than about 1s, the heat transfer process turns to normal convective heat transfer through the thermal boundary layer influenced by the flow of helium gas. Therefore, in this study, the average value of heat transfer coefficients at periods larger than about 1s are taken as quasi-steady-state heat transfer coefficient.

4.2 Effect of helical pitch on heat transfer coefficient

4.2.1 Simulation models

Figure 4.2 shows the physical model in this numerical solution. The heater was mounted horizontally along the center axis of the circular channel, which is 20 mm in diameter. The twisted plate is 4 mm in width, 0.1 mm in thicknesses and 60 mm in length. The platinum plate was twisted at the center. Both ends of it were connected to two copper plates with the same thickness of twisted plate.

A 3D model was built with necessary simplification. Forced convection transient heat transfer for helium gas flowing over twisted plate with exponentially increasing heat input ($\dot{Q} = \dot{Q}_0 \exp(t/\tau)$) were numerically calculated, where, $\dot{Q}$ is heat generation rate, W/m^3, $\dot{Q}_0$ is initial heat generation rate, W/m^3, t is time, s, and τ is a period of heat generation, s. A smaller or shorter τ means a higher increasing rate of heat generation.

Three kinds of helical pitch of 20 mm, 25 mm and 30 mm were conducted for the model, as shown in Figure 4.3.

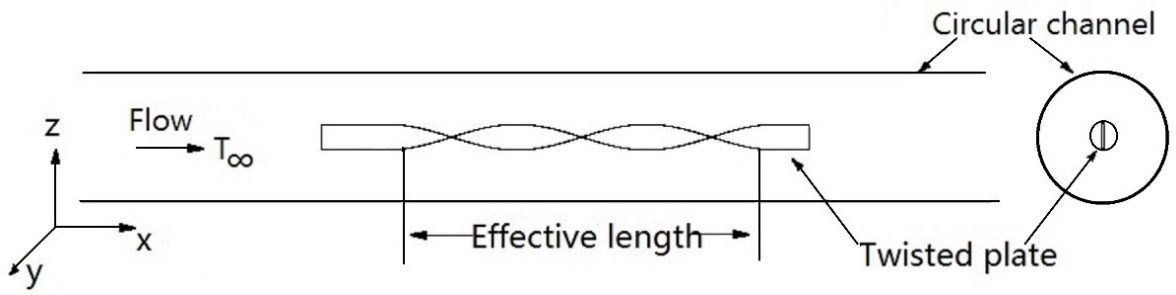

Figure 4.2 Physical model.

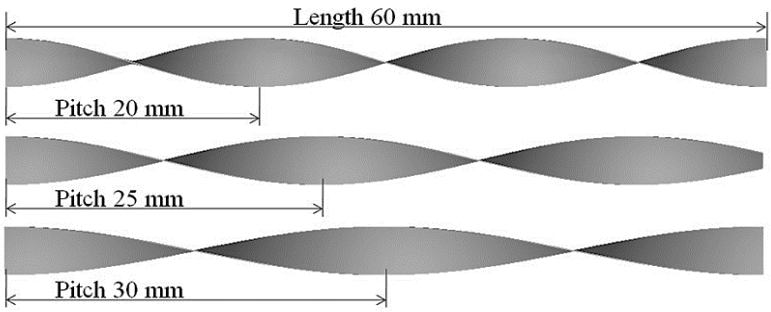

Figure 4.3 Twisted plate with various helical pitch.

4.2.2 A Partial validation study

Figure 4.4 shows time-dependence of heat generation rate, heat flux, and surface temperature difference at various heat generation rate increasing periods of 176, 1691 and 8355 ms. Flow velocity is 10 m/s. The gas temperature is 303 K at 500 kPa. The helical pitch of twisted plate is 20 mm and the model contains three pitches in total.

The symbols show previous experimental data [17], and the lines show values of the numerical solution. The heat generation rate, heat flux and temperature difference increase rapidly as the period is shorter and it is understood that the heat flux and surface temperature difference increase exponentially as the heat generation rate increases with exponential function. The simulation results of heat flux and temperature difference agree well with the experimental data within 3.0% and 1.2%, respectively.

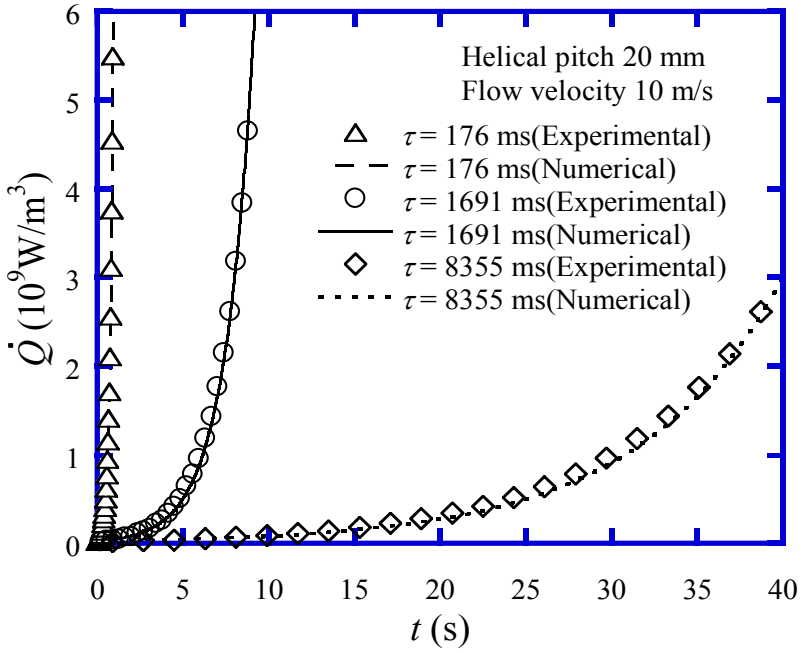
Helical pitch 20 mm
Flow velocity 10 m/s
τ = 176 ms(Experimental)
τ = 176 ms(Numerical)
τ = 1691 ms(Experimental)
τ = 1691 ms(Numerical)
τ = 8355 ms(Experimental)
τ = 8355 ms(Numerical)
$\dot{Q}$ (10^9W/m^3)
t (s)
0
1
2
3
4
5
6
0
5
10
15
20
25
30
35
40

(a) $\dot{Q}$

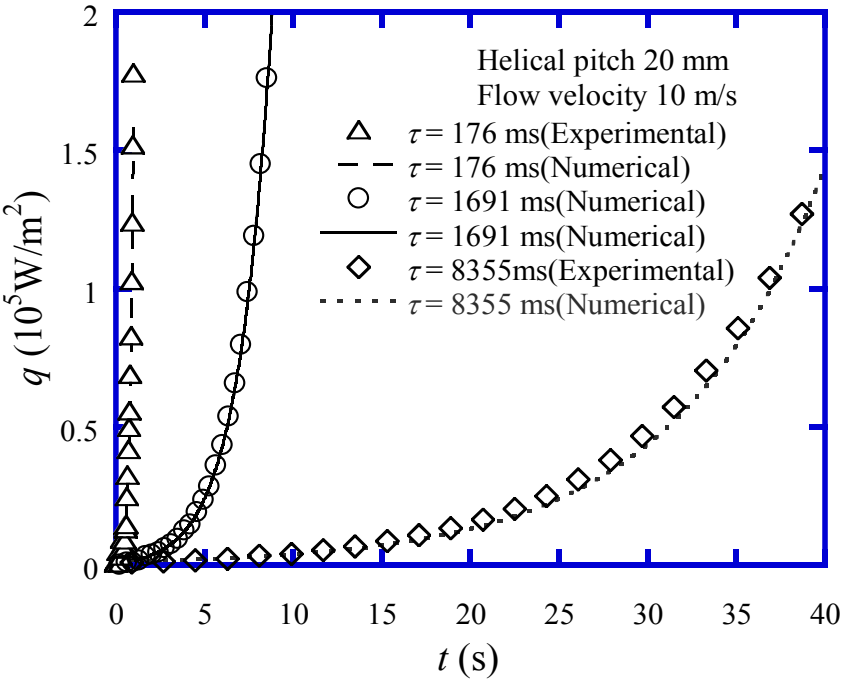
Helical pitch 20 mm
Flow velocity 10 m/s
τ = 176 ms(Experimental)
τ = 176 ms(Numerical)
τ = 1691 ms(Numerical)
τ = 1691 ms(Numerical)
τ = 8355ms(Experimental)
τ = 8355 ms(Numerical)
q (10^5W/m^2)
t (s)
0
0.5
1
1.5
2
0
5
10
15
20
25
30
35
40

(b) q

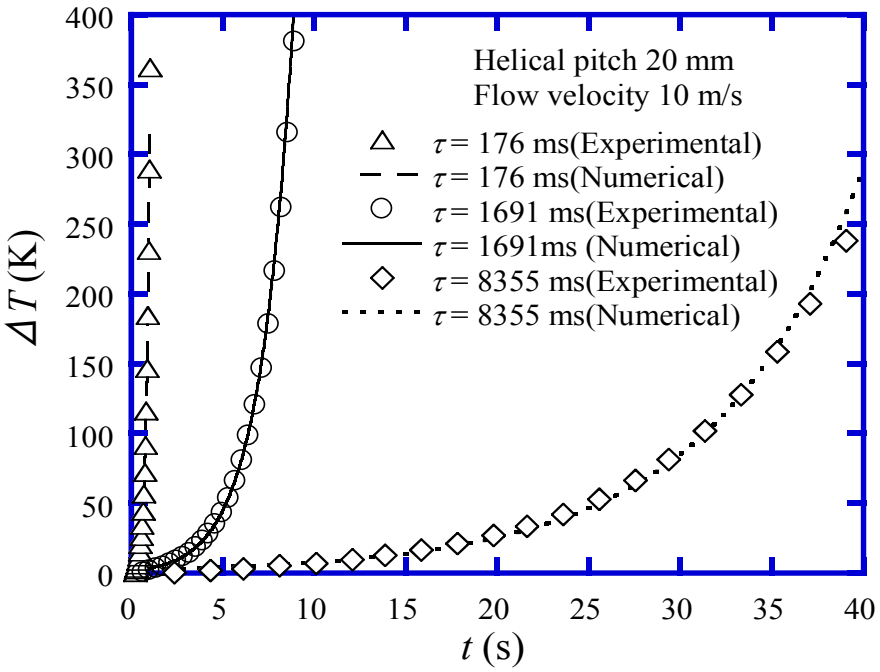

(c) ΔT

Figure 4.4 Comparison of $\dot{Q}$, q and ΔT with experimental data at various periods.

Figure 4.5 shows instantaneous heat transfer coefficients versus times at various flow velocities. The helical pitch of twisted plate is 20 mm and the model contains three pitches in total. As seen from the figure, heat transfer coefficient increases with the increase of flow velocity. For higher flow velocities at 8 m/s and 10 m/s the numerical results agree well with the experimental data, while for lower flow velocities, the simulation values are somewhat lower than experimental data, and the differences are within 7.4%.

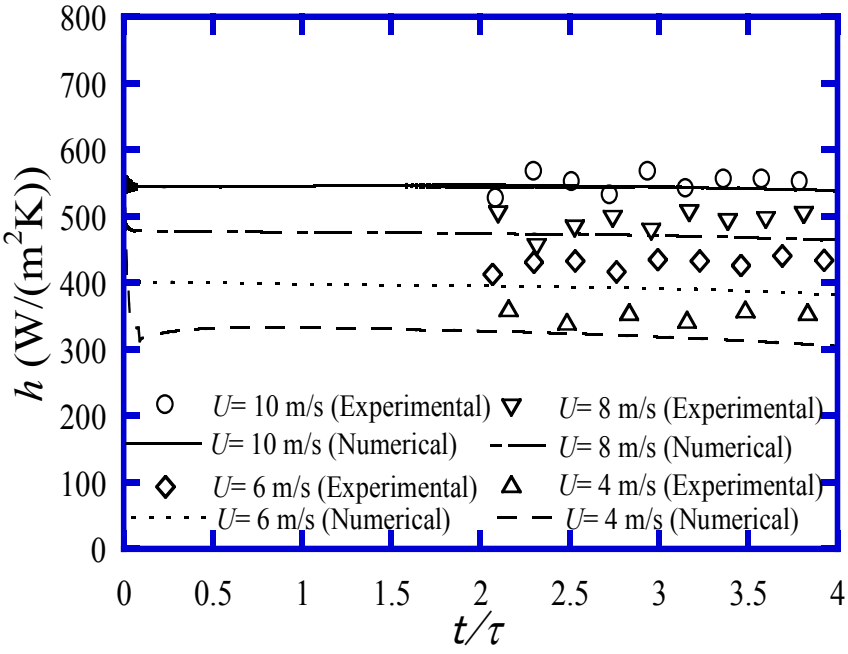

Figure 4.5 Effects of flow velocity on heat transfer.

The simulation results for the twisted heater with the helical pitch size of 20 mm showed reasonable agreement with the experimental data. This comparison partially validated the numerical study for the effect of pitch size on heat transfer.

4.2.3 Simulation results for various helical pitch sizes

To study the effect of helical pitch on heat transfer enhancement. Various helical pitches of 20, 25 and 30 mm were modeled at the period of 1691 ms and the flow velocity

of 10 m/s. A flat plate with the same width of the twisted plates is also modeled to be compared with.

The comparison of heat transfer coefficient of twisted plate with flat plate is shown in Figure 4.6. The heat transfer coefficient increases with the decrease of pitch length of twisted plate. An increasing ratio of about 6% can be generated by decreasing pitch size from 30 mm to 25 mm, or from 25 mm to 20 mm.

In this numerical simulation, the heat transfer coefficients for the twisted plate are 35-55% higher than those of flat plate. Therefore, it was considered that the short pitch twisted heater is useful for the enhancement of heat transfer.

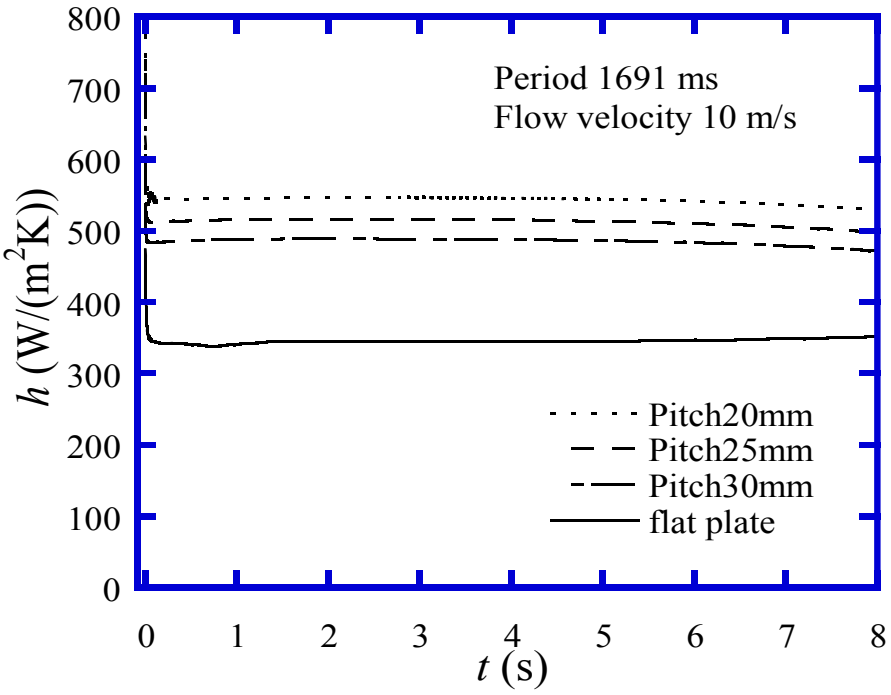

Figure 4.6 Heat transfer coefficient at various pitches.

A cross section of velocity distribution can be obtained from the simulation result at the middle of the heater along the length direction. The velocity distribution of the fluid area around the twisted plate with pitch size of 20 mm is compared to the flat plate, shown in Figure 4.7. The velocity is 10 m/s. The period of heat generation is 1.4 s and the time is 4 s, which means 4 seconds passed after the start of heating.

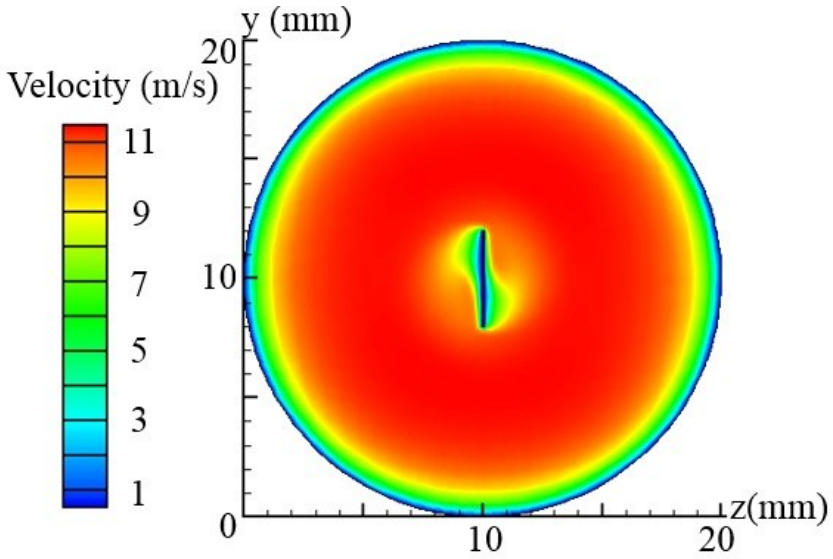

(a) Twisted plate

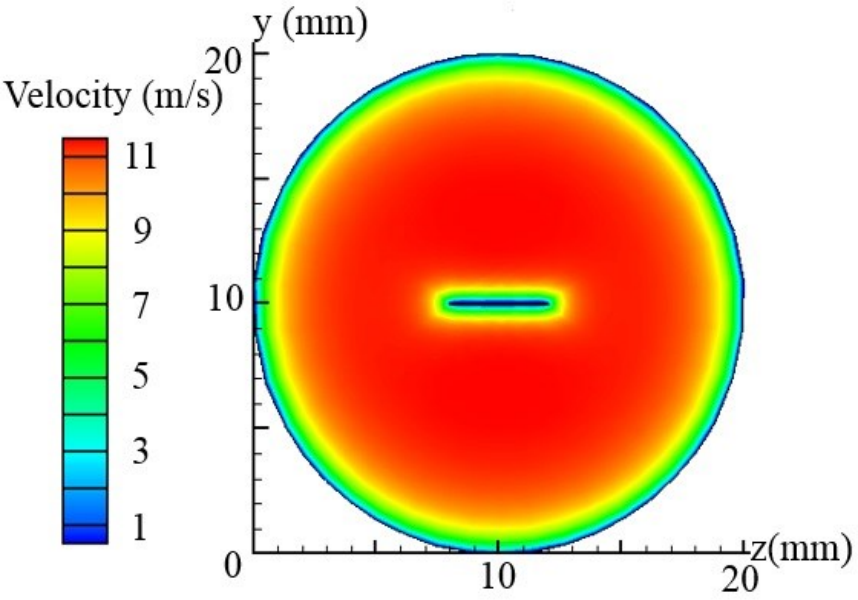

(b) Flat plate

Figure 4.7 Velocity distribution of the cross section view in the middle length

It can be found that a swirl distribution occurs for velocity boundary thickness around the twisted plate. While for the flat plate, the velocity boundary layer thickness is almost uniform.

It is considered that the helical vortices generated by the surface curvature of twisted plate will improve turbulence intensity and promote greater “thermal mixing”. It will result in sharper temperature gradients in the boundary layer and higher heat transfer coefficient. Besides, centrifugal force generated by the twisted structure will lead to a pressure distribution on the heater surface in the radial section. Thus, secondary flow perpendicular to the main flow will generate. This secondary flow in the radial direction

will contribute to the flow velocity and thus resulted in heat transfer coefficient enhancement.

With smaller pitch size, the twisting degree increases and contributes to the generating of swirl flow which will result in higher heat transfer coefficient. Therefore it is considered that the enhancement of heat transfer was attributed to swirl flow induced by twisted plate.

4.3 Effect of length on heat transfer coefficient

4.3.1 Experimental conditions

The effect of length on heat transfer coefficient was studied by experimental research using a series of twisted plates with different lengths. The heat generation rate of the twisted plate was increased with an exponentially increasing function. The heat flux, surface temperature difference and heat transfer coefficient were measured under various periods and velocities. The experimental apparatus and method has already been introduced in chapter 2. The test heater was mounted horizontally along the center part of the circular test channel, which is made of stainless steel (20 mm in the inside diameter), as shown in Figure 4.8. Platinum plate with thickness of 0.1 mm, width of 4 mm was used as the test heater. Three twisted heaters with effective length of 26.8 mm, 67.8 mm and

106.4 mm (pitch number of 1, 3 and 5) were used in this experiment, as shown in Figure 4.9. They were twisted with the same helical pitch of 20mm.

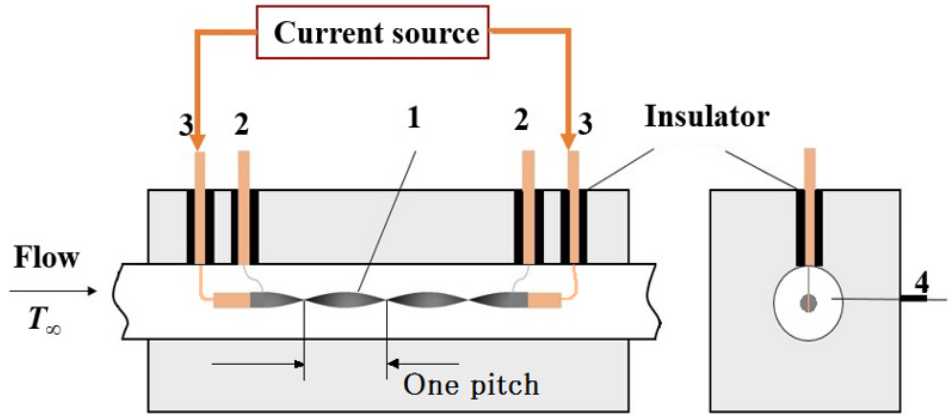

1. Test heater 2. Potential conductor 3. Current conductor 4. Thermocouple

Figure 4.8 The test section

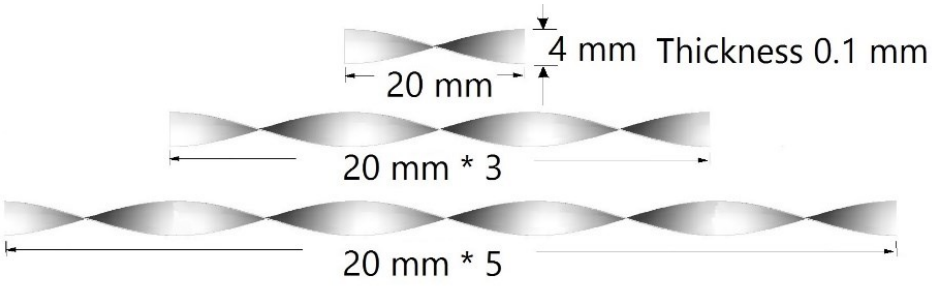

Figure 4.9 Twisted heaters with different length.

Experimental conditions are shown in Table 4.1. The transient heat transfer

experimental data were measured for the periods of heat generation rate ranged from 35 ms to 14 s and for the helium gas temperature of 303 K under a system pressure of around 500 kPa. The flow velocities ranged from 4 to 10 m/s, and the corresponding Reynolds numbers (Re) ranged from 2×10^3 to 3×10^4.

Table 4.1. Experimental conditions

Test fluid	Helium gas		
Effective length	26.8 mm	67.8 mm	106.4 mm
Pitch number	1	3	5
Pitch size	20 mm		
Period of heat generation rate	35 ms ~ 14 s		
Gas temperature	303 K		
System pressure	500 kPa		
Flow velocity	4 ~ 10 m/s		
Reynolds number	2000 ~ 30,000		

4.3.2 Experimental results for heat transfer coefficient

Figure 4.10 shows the effect of heater length at various periods and flow velocity of

10 m/s. The heat transfer coefficient, h, becomes to approach asymptotic value for each heater length when τ is longer than about 1 s. On the other hand, when the period τ is shorter than about 1 s, h increases as τ shortens. It has been clarified in the early works that at extremely short period (τ < 100 ms), the conductive heat transfer near the heater comes to govern the heat transfer process, and the heat transfer coefficient increases greatly with shorter period in this region. When period τ is larger than about 1s, the heat transfer process turns to normal convective heat transfer through the thermal boundary layer influenced by the flow of helium gas. In this study, the average value of heat transfer coefficients at periods larger than about 1s are taken as quasi-steady-state heat transfer coefficient.

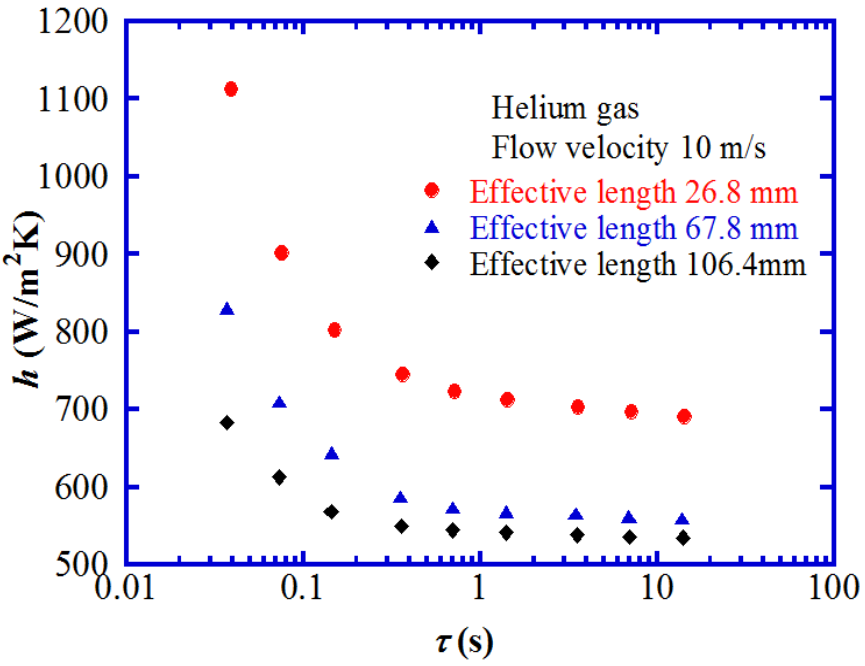

Figure 4.10 Effect of length on heat transfer coefficient at various periods.

In addition, it can be seen from Figure 4.10 that the heat transfer coefficient decreases with the increase of heater length. The quasi-steady-state heat transfer coefficient for the heater with effective length of 26.8 mm is about 700 W/(m^2·K), about 24% higher than that of the 67.8 mm heater. While the quasi-steady-state heat transfer coefficient improved only about 5% by comparing the 67.8 mm-length heater to the 106.4 mm-length heater. So, it can be concluded that the heat transfer coefficient along the length direction of a twisted plate is not constant and the distribution is nonlinear. It is considered that the thermal boundary layer becomes thick along the flow direction and lead to a lower heat transfer coefficient in the downstream side of the twisted plate. To

find the distribution of heat transfer coefficient along the length direction and to clarify the phenomena, numerical simulations will be carried out later in this study (refer to section 4.4).

4.3.3 Correlations for quasi-steady state heat transfer of twisted plate

Manglik and Bergles. [23] used a swirl parameter to describe the intensity of the tape-twisted induced secondary motion and it is defined as

$$\text{Swirl parameter} = \frac{(\text{centrifugal force})(\text{convective inertia force})}{(\text{viscous force})^2}$$

$$= \frac{(\rho U^2 / H)(\rho U^2 / d)}{(\mu U / d^2)^2} = \text{Re}^2 / y \tag{4.1}$$

Where, d is characteristic length and U is velocity.

In this study, the heat transfer enhancement of the twisted plate itself was investigated and a redefined swirl parameter $Sw = \text{Re}_{sw} / \sqrt{y}$ was adopted to indicate the swirl flow effect since the square of Reynolds number becomes very large in magnitude. Where, $\text{Re}_{sw} = U_s L_s / \nu$, U_s is the swirl velocity and L_s is the helical flow length for the twisted plate, expressed in the following equations.

$$U_s = U[1 + (\pi / 2y)^2]^{1/2} \tag{4.2}$$

$$L_s = L[1 + (\pi / 2y)^2]^{1/2} \tag{4.3}$$

$$y = H / W \tag{4.4}$$

where, L is effective length of the twisted plate (centerline length, m), y is twisted ratio, H is the pitch size (m) and W is the plate width (m). The helical flow length refers to the helically twisted streamline and can be expressed in Figure 4.11.

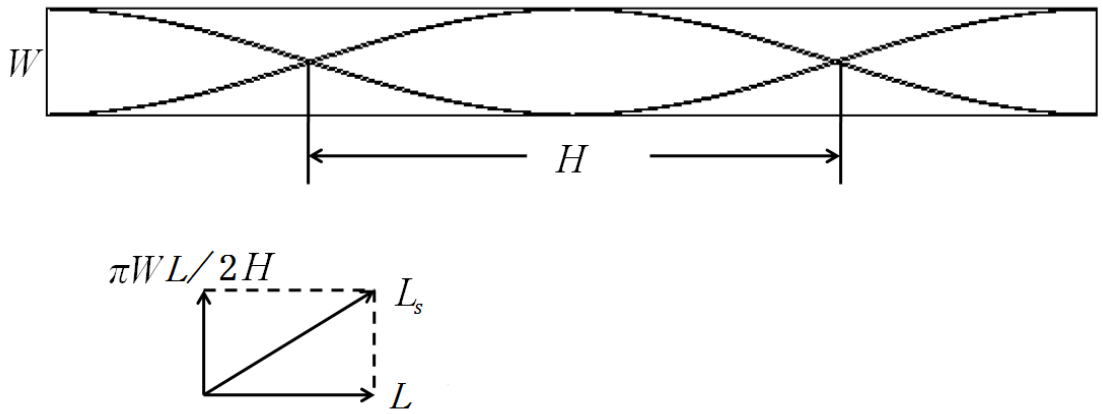

Figure 4.11 Helical flow length for twisted plate.

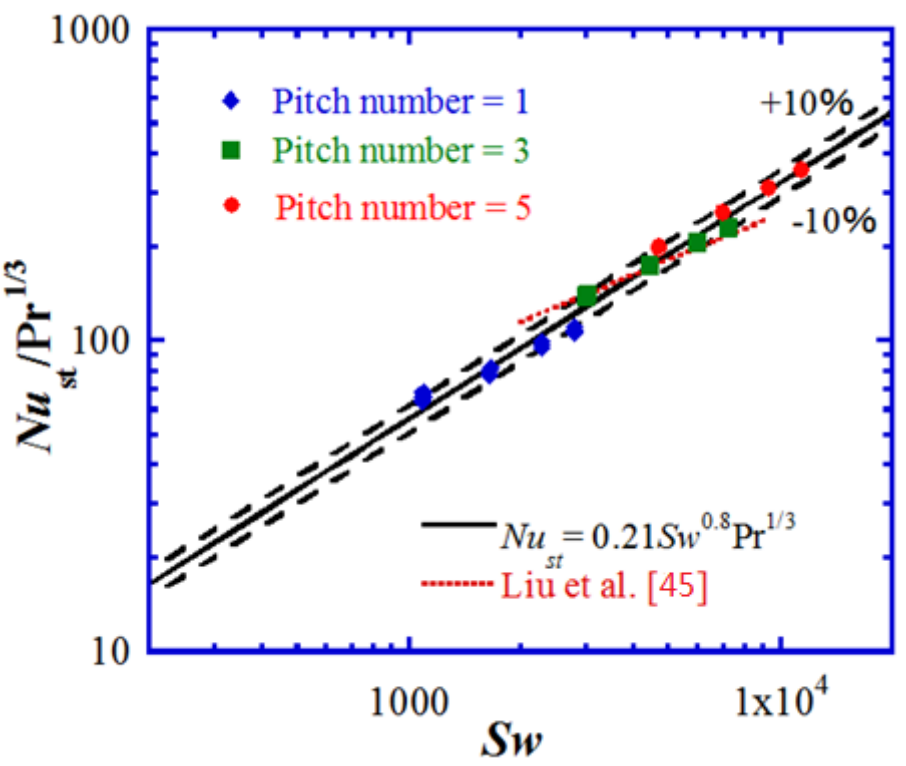

Figure 4.12 Quasi-steady-state heat transfer at various swirl parameters.

The relationship between the Nusselt number and the *Sw* parameter for various periods ranging from 1.4 s to 14 s with flow velocity ranging from 4 to 10 m/s was shown in Figure 4.12. Effective length of the twisted plates are 26.8 mm, 67.8 mm and 106.4 mm, respectively. As shown in the $Nu_{st}/Pr_f^{1/3}$ versus *Sw* graph, the Nusselt numbers for quasi-steady state increases with the redefined swirl parameter *Sw*. It can be correlated by the following equation.

$$Nu_{st} = 0.21 Sw^{0.8} \, \mathrm{Pr}^{1/3} \tag{4.5}$$

Where, $Nu_{st} = h_{st} L_s / \lambda$, h_{st}(W/m^{2}K) is quasi-steady state heat transfer coefficient, Pr is

Prandtl number (about 0.68 in the range of this experiment).

In Figure 4.12, maximum error occurs at the one-pitch case with velocity of 4 m/s where the flow is more near laminar region. For *Sw* larger than 4000, the empirical correlation matches experimental data well, with differences within 10%. As should be noticed, the transition from laminar flow to turbulent flow usually occurs at Re of about 5×10^4 for a flat plate. While for the twisted plate the transition region is considered to occur at a much lower Re due to the disturbing of flow generated by the swirl structure. A similar correlation was obtained by Liu et al. [45] with a different exponent of 0.5 for *Sw* and in the research *Sw* ranged from 3000 to 8000. The correlation was plotted by a dot line in Figure 4.12. As can been found, for this small range of *Sw*, the correlation can express the Nusselt number well. However, in this study the swirl parameter *Sw* has a larger range of about 1000 to 20000. With an overall consideration of the three different length, an empirical correlation was obtained in this research.

4.3.4 Correlations for transient heat transfer of twisted plate

As stated in the introduction, Liu et al. [16-18] carried out experiments on the transient heat transfer of helium gas for cylinders and flat plates. An empirical correlation of the ratio of transient Nusselt number (Nu_{tr}) to the quasi-steady-state Nusselt number

was obtained using a dimensionless period of τ^* ($\tau^* = \tau U/L$, U is flow velocity, and L is effective length). The present experimental data can be also correlated using the dimensionless period, $\tau U/L$. As shown in Figure 4.13, the empirical correlation for twisted plate with different length can be obtained as follows.

$$Nu_{tr} = Nu_{st}[1 + C(\tau U_s / L_s)^{-0.8}] \tag{4.6}$$

where, $\tau U_s/L_s = \tau U/L$.

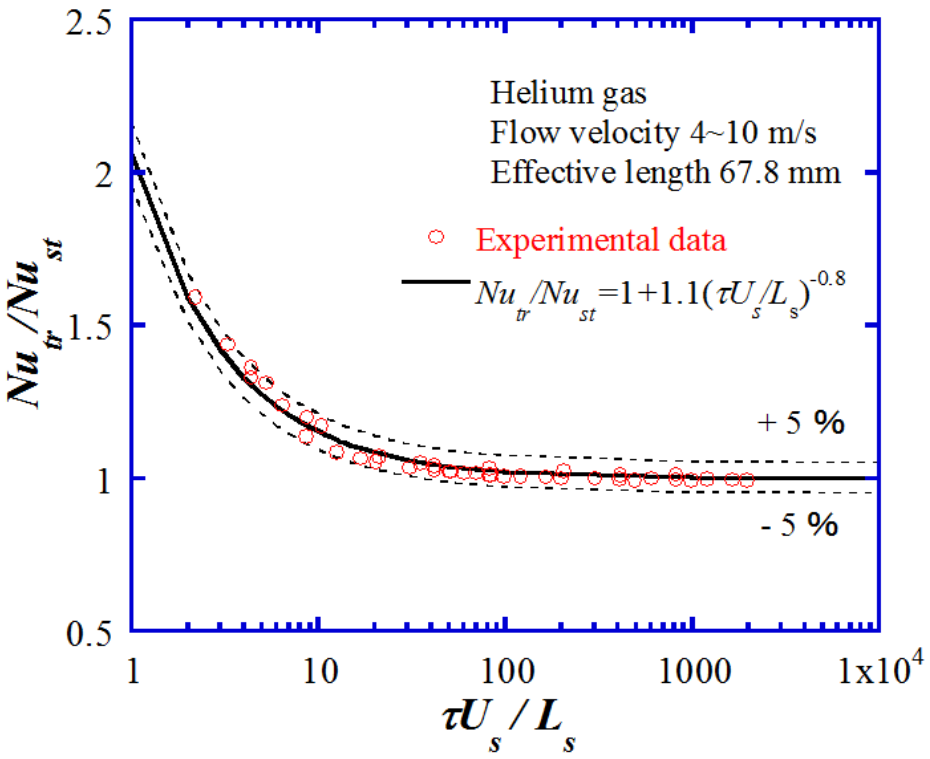

Figure 4.13 Transient heat transfer for twisted plate at various flow velocities and periods.

It can be seen that, the ratios of Nu_{tr} to Nu_{st} decrease to unity as the dimensionless

period τ^* increases. The transient heat transfer approaches quasi-steady-state one for τ^* larger than about 300. The coefficient C equals 4.0, 1.1 and 0.75 for different effective length of 26.8 mm, 67.8 mm and 106.4 mm, respectively. Here, the coefficient C for the shortest 26.8 mm heater is much larger than the other two heaters. It is because the Reynolds number for the shortest heater is about 2000 which is in the region of laminar flow (for a flat plate). In this region, the effect of conductivity takes more important part. Therefore, the increasing ratio of heat transfer coefficient from quasi-steady state region to transient region for a short heater is larger.

4.4 Local heat transfer coefficient

The distribution of heat transfer coefficient on the heater surface is shown in Figure 4.14 The heat generation period τ is 1.4 s and the passage time for heat generation is at t=4.2 s ($t = 3\tau$). The effective length is 60 mm with three pitches. The flow velocity is 10 m/s. Generally, heat transfer coefficient decreases along the length direction. A larger heat transfer coefficient was generated in the surface of twisted heater that facing the flow which is due to the disturbing of flow caused by the crash between helium gas and the twisted surface. There exists a distribution for the heat transfer coefficient along the width direction. The side facing the flow has larger heat transfer coefficient while smaller heat

transfer coefficient exists at the leeward side. The highest heat transfer coefficient exists at both edges of twisted plate where the thermal boundary thickness is very small.

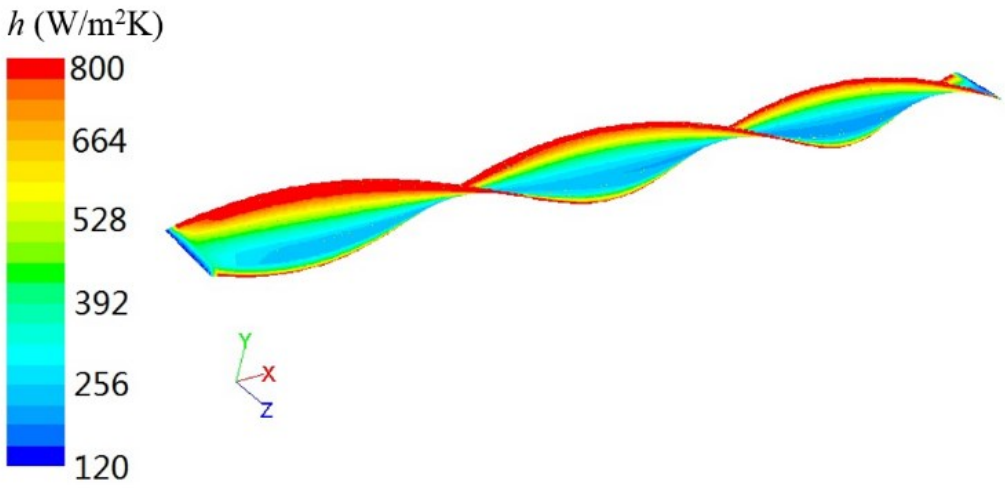

Figure 4.14 Distribution of heat transfer coefficient on the heater surface.

Figure 4.15 shows several cross section views of the temperature field in YOZ plane at different locations along the twisted plate. The period is 1.4 s at the flow time of $t = 3\tau$. The flow velocity is 10 m/s. The effective length is 60 mm covering three pitches. It can be found from the figure that generally the temperature boundary layer turns thicker along the x direction of plate. It results in the increasing of surface temperature along the length direction of the heater. The heat transfer coefficient decreases along the length direction as the thermal boundary layer turns thicker. The velocity boundary layer is alike the temperature boundary layer. It can be seen that the velocity boundary swirls with the

twisted plate, and a maximum velocity of over 10 m/s occurs around the heater. It is considered that the swirl structure of twisted plate may induce a swirl flow, and a radial velocity will be generated along the twisted plate, then it contributes to the increased flow velocity.

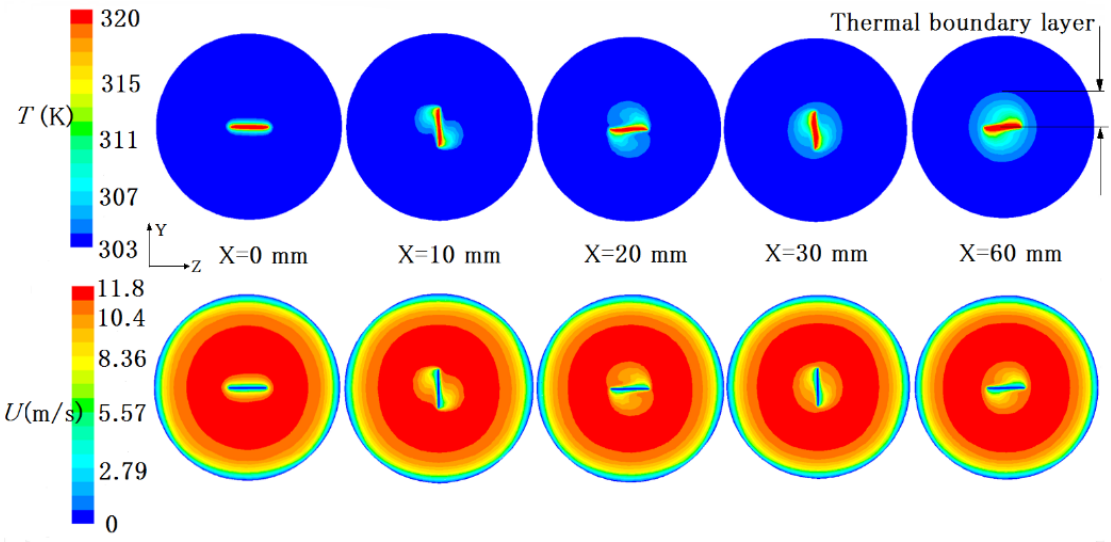

Figure 4.15 Cross section of temperature and velocity contours in YOZ plane.

In addition to the effect of increased flow velocity, it is considered that the helical vortices generated by the surface curvature of twisted plate will improve turbulence intensity and promote greater “thermal mixing”. Figure 4.16 shows the 3D velocity distribution around the center part of the twisted plate. As can be found that a swirl flow was generated. It will result in sharper temperature gradients in the boundary layer and

higher heat transfer coefficient. Therefore it is considered that the enhancement of heat transfer was attributed to the effects of “thermal mixing” and increased flow velocity.

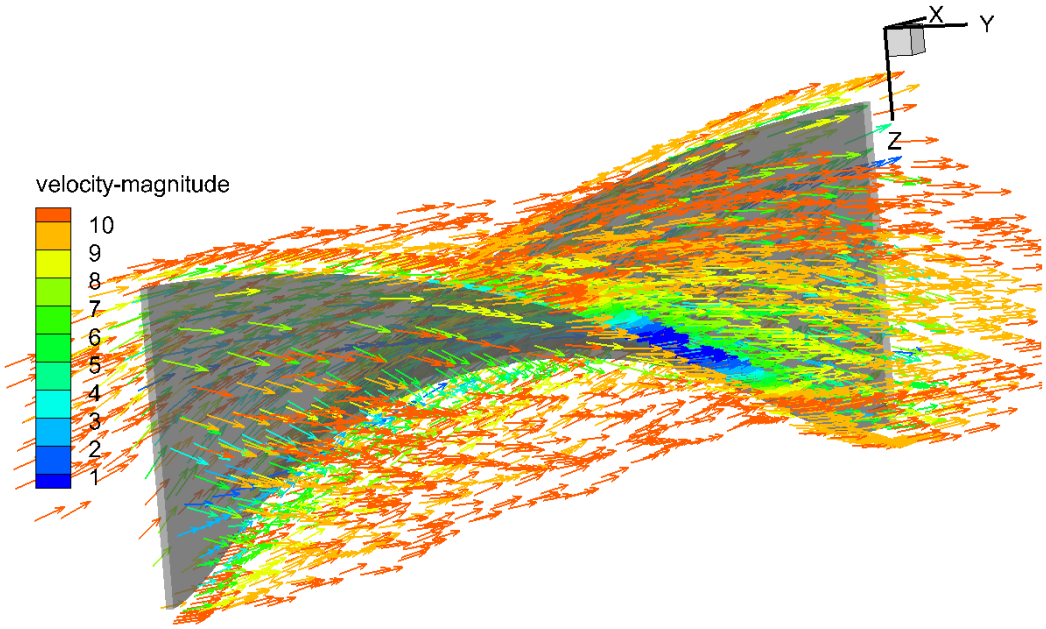

Figure 4.16 3D velocity distribution around the twisted plate.

As mentioned above, the heat transfer coefficient increases with the decrease of the heater length and the increasing ratio is not linear. The heat transfer coefficient increases about 5% from the five-pitch heater to the three-pitch heater while the increasing ratio of three-pitch heater to one-pitch heater is about 24%. Thus, it is considered that a shorter heater is of significant influence on heat transfer coefficient.

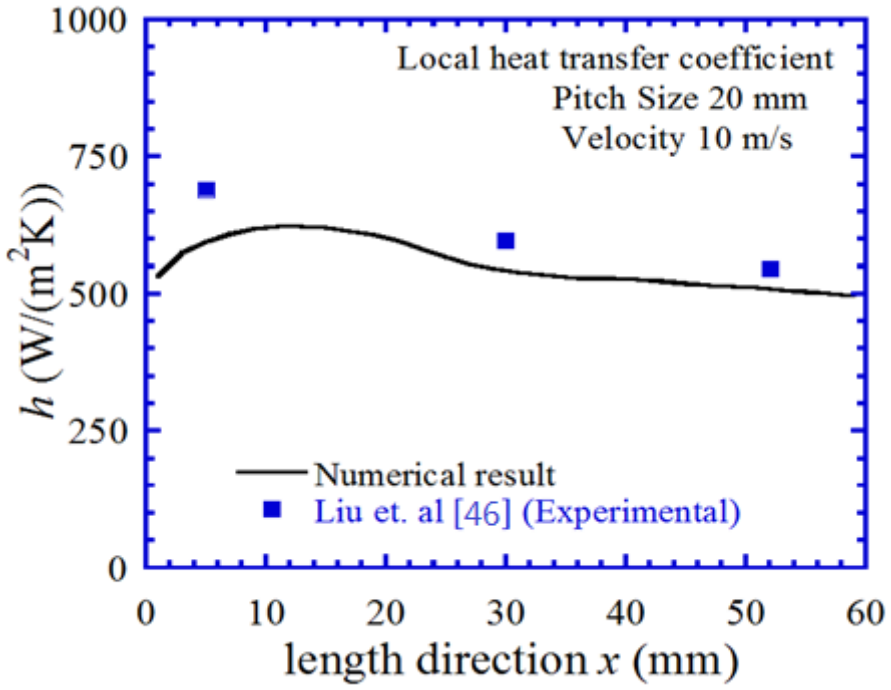

Figure 4.17 Local heat transfer coefficient along the twisted plate.

Simulation results for local heat transfer coefficient for the three-pitch case is shown in Figure 4.17. Heat transfer coefficient decreases along the length direction though it shows some fluctuations along the heater. Highest local heat transfer coefficient exists at the first pitch and decreases greatly through the second pitch. Then, for the last pitch heat transfer coefficient almost comes to a stable value. Experimental research for local heat transfer coefficient was reported in a previous work [46]. Experimental data are also shown in Figure 4.17 for comparison. The experimental data showed almost the same trend of dependence on local length, though they are about 7% to 13% higher than those of numerical values.

4.5 Summary

In this section, Parametric studies for forced convection parallel flow over a twisted plate was conducted with experimental tests and numerical simulations. The effect of flow velocity, the helical pitch size, the heater length and the local heat transfer coefficient distribution was discussed. The heat transfer coefficient for the twisted plate was enhanced, in comparison with the flat plate. It is indicated that a twisted plate either with a short length or with a smaller helical pitch size will contribute to the heat transfer coefficient.

There exists a distribution for the heat transfer coefficient along the width direction. According to the simulation results, the side facing the flow has larger heat transfer coefficient while smaller heat transfer coefficient exists at the leeward side. The highest heat transfer coefficient exists at both edges of twisted plate where the thermal boundary thickness is very small. Additionally, it is determined that the swirl structure of twisted plate may induce a swirl flow, and a radial velocity will be generated along the twisted plate, then it contributes to the increased flow velocity. Both the increased flow velocity and the helical vortices generated by the surface curvature of twisted plate will improve turbulence intensity and promote greater “thermal mixing”.

Chapter V

Thermal-hydraulics Analysis in VHTR Core

5.1 Introduction to prismatic VHTR core

The prismatic VHTR is a helium-cooled block type reactor. Hexagonal graphite blocks with fuel embedded are stacked as concentric rings in the core. A cutaway view of the 600 MWth General Atomics Gas-Turbine Modular Helium Reactor (GT-MHR, General Atomics, 1996) is shown in Figure 5.1 [47]. The active core contains 102 columns of fuel elements stacked 10 elements high, for a total of 1020 elements. Ten layers of fuel elements are stacked in the vertical direction; each fuel element is 360 mm in width and 793 mm in height. A cross-sectional view of the core is shown in Figure 5.2. Small gaps among the neighboring fuel elements exist due to tolerances in manufacturing and installation. In addition, the gap size will change during operations due to thermal expansion and fast-neutron induced shrinkage, as demonstrated by Burchell [48]. The flow paths in the prismatic core are also shown in Figure 5.2.

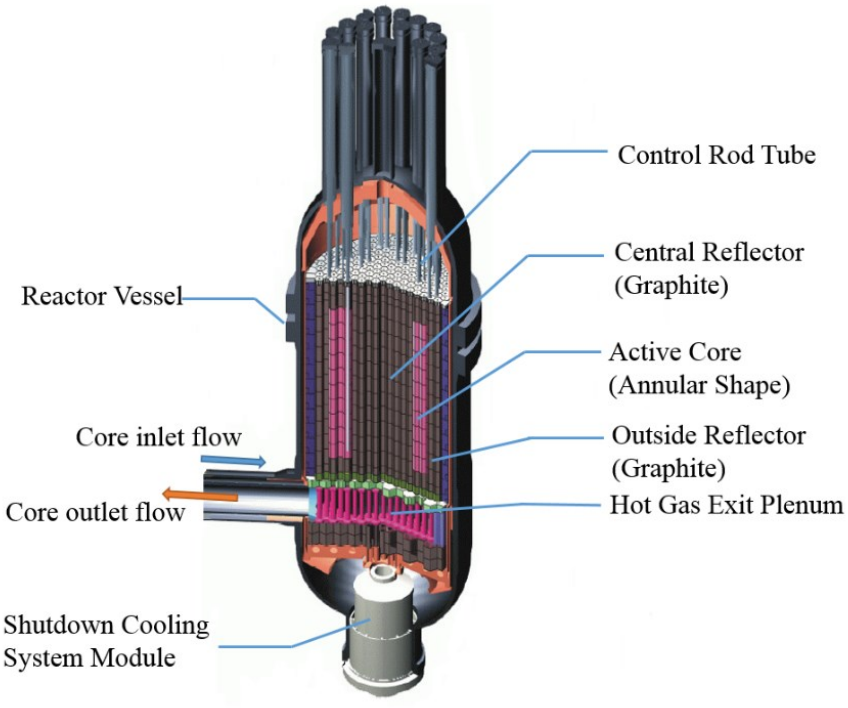

Figure 5.1 Cutaway view of the GT-MHR [47].

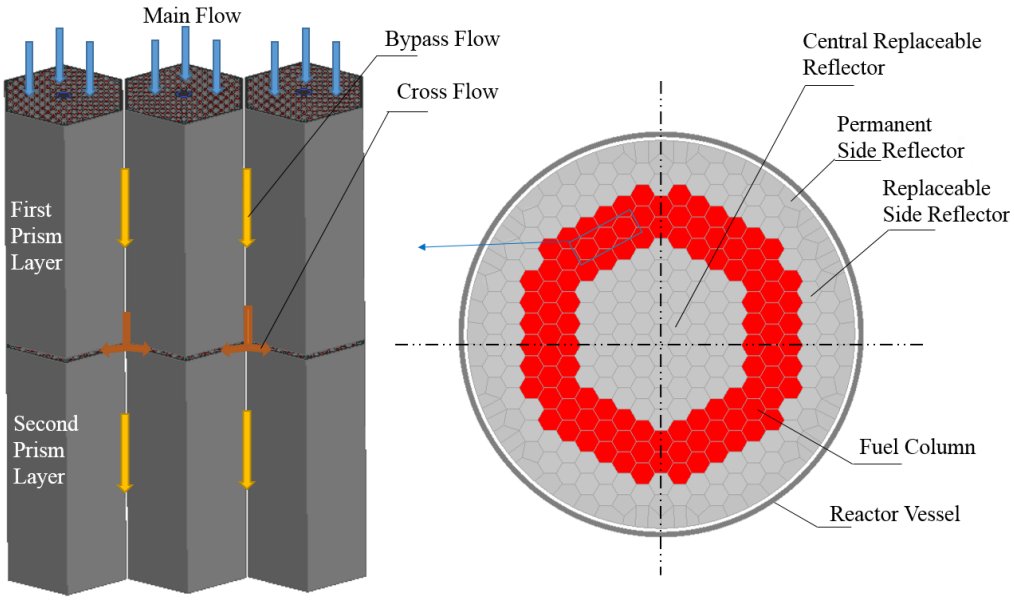

Figure 5.2 Bypass flow and cross flow gaps in the core.

The majority of the coolant flows through the coolant holes as designed, while a small portion of coolant will flow through the gaps between the hexagonal graphite blocks, which is defined as the bypass flow. In addition, the coolant that flows in a direction perpendicular to the coolant holes through the interfacial gaps between two block prisms is defined as the cross flow. The existence of bypass and cross flows decreases the coolant flow through the coolant channel resulting in an increase in maximum fuel temperature, thereby raising potential structural problems. In addition, some researches indicate that the bypass and cross flow will cause a large variation in temperature for the coolant jets exiting the core into the lower plenum. This may cause a “hot streaking” issue near the entrance of the hot outlet duct. In this regard, evaluation of the core flow distribution and thermal hydraulic analysis are important for the reactor design and safety assessment.

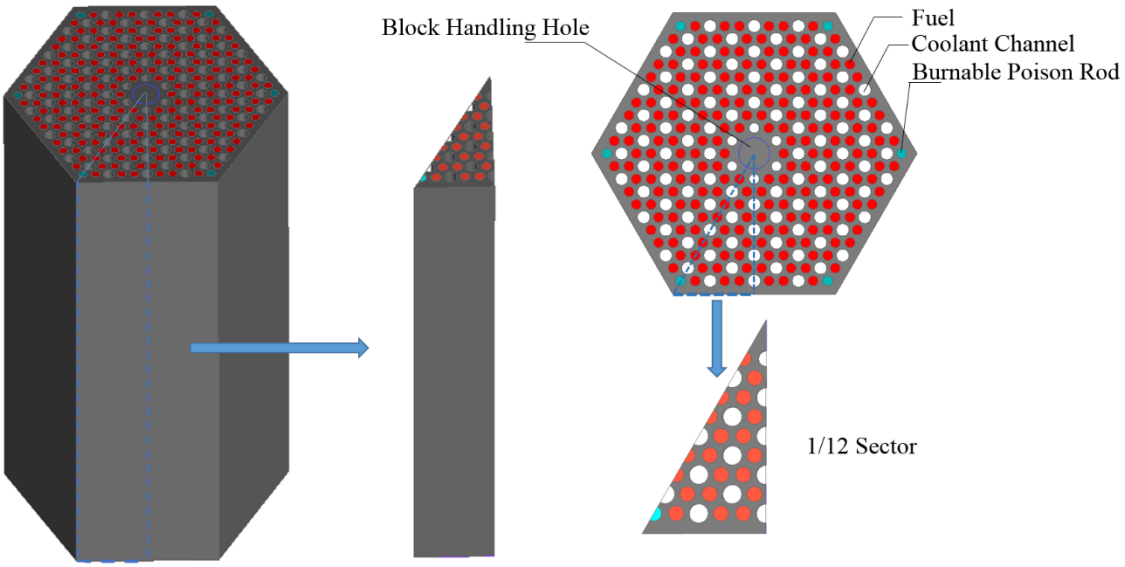

Figure 5.3 Standard fuel element for the GT-MHR.

The standard fuel element for the GT-MHR is shown in Figure 5.3. Red circles refers to fuel rods, white circles represent for coolant channels, blue circles are burnable poison rod and the gray areas shows the graphite. There are two different sizes of coolant channels, 12.70 mm diameter of a half coolant channel near the center of the fuel block, and other 5 full and 7 half coolant channels of 15.88 mm diameter. The 1/12 sector also covers 17.5 fuel holes and a half burnable poison rod hole. A one-twelfth sector of the fuel block is sectioned owing to the symmetrical structure, as shown in Figure 5.3.

5.2 CFD application

A full size model of 10.704 m is built, including an upper reflector section of 1.189

m, 10 fueled blocks and a lower reflector section of 1.585 m. The location of bypass and cross gaps are shown in Figure 5.4. The central block handling hole is ignored in the CFD model and set to graphite properties. Helium gas flows from the inlet downwards into the lower plenum with an inlet temperature of 490 °C at approximately 7 MPa. A pressure drop of approximately 34.5 kPa is used in this study. A uniform heat generation rate of 27.88 MW/m^3 is established for the fuel channels. Symmetry boundary conditions are set for all the other sides of the model.

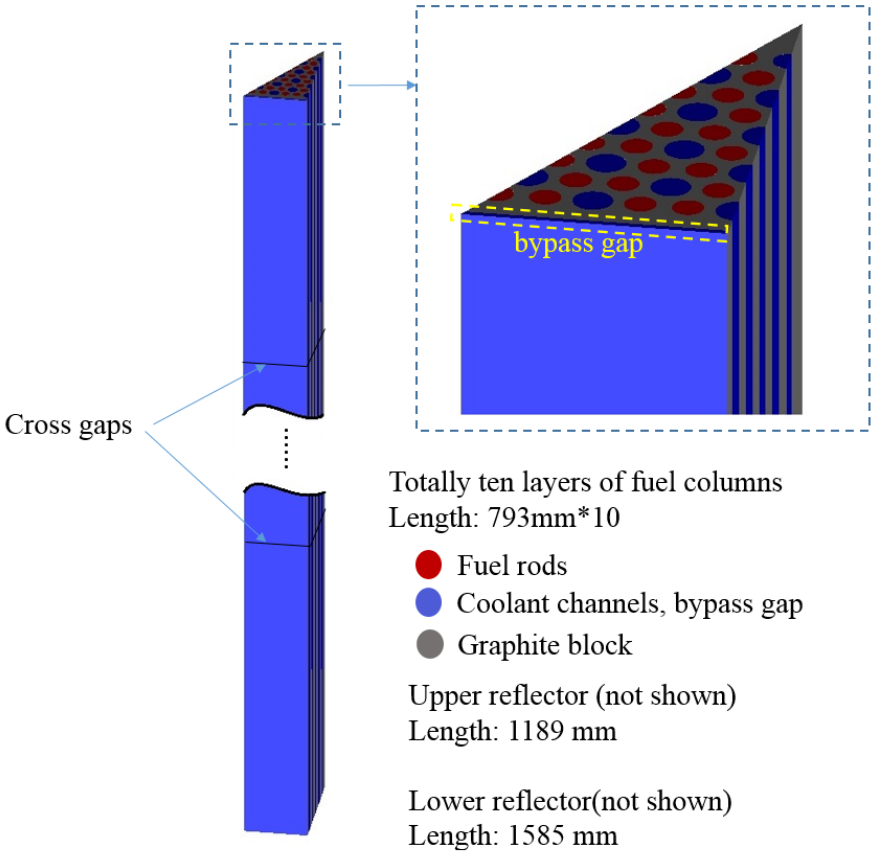

Figure 5.4 The full length simulation model.

5.2.1 Mesh generation and validation

The mesh used in this study is hexahedral dominate and is created using ANSYS ICEM14.0. Figure 5.5 shows a cross section view of the mesh generated for the one-twelfth sector. Blue areas indicate the coolant channel, red mesh represents the fuel rods, and the black mesh refers to the graphite block. A mesh independence study is conducted by comparing the previous mesh (no gap) with a finer mesh, for which a smaller mesh size has been used in the fuel compact and graphite regions. Total cell numbers of the two meshes are approximately 7.2 and 11 million, respectively. Simulation results of the total mass flow rate and maximum fuel temperature are compared between the two mesh cases. The differences for the total mass flow rate and maximum fuel temperature are 0.015% and 0.01%, respectively. This result indicates that the mesh size is adequate for the solid area.

Very fine meshes were set for the bypass gaps and cross flow gaps with a y^+ value of less than 3. In the very small bypass flow gaps of 3 mm (1.5 mm in the model according to symmetry structure) and 5 mm (2.5 mm in the model according to symmetry structure), 30 and 50 mesh layers were put in the gaps, respectively. By doubling the mesh layers of the 3 mm bypass gap case, a difference of less than 0.2% was found for the bypass gap outlet temperature and mass flow rate. In the very small cross flow gaps of 1 mm and 3

mm, 20 and 60 layers were put in the gaps, respectively. By doubling the mesh layers of the 1 mm cross gap case, a difference of less than 0.05% was found for the total mass flow rate and coolant channel outlet temperature. This indicated that the meshes used in the bypass flow and cross flow gaps were sufficiently robust to meet the analytical needs.

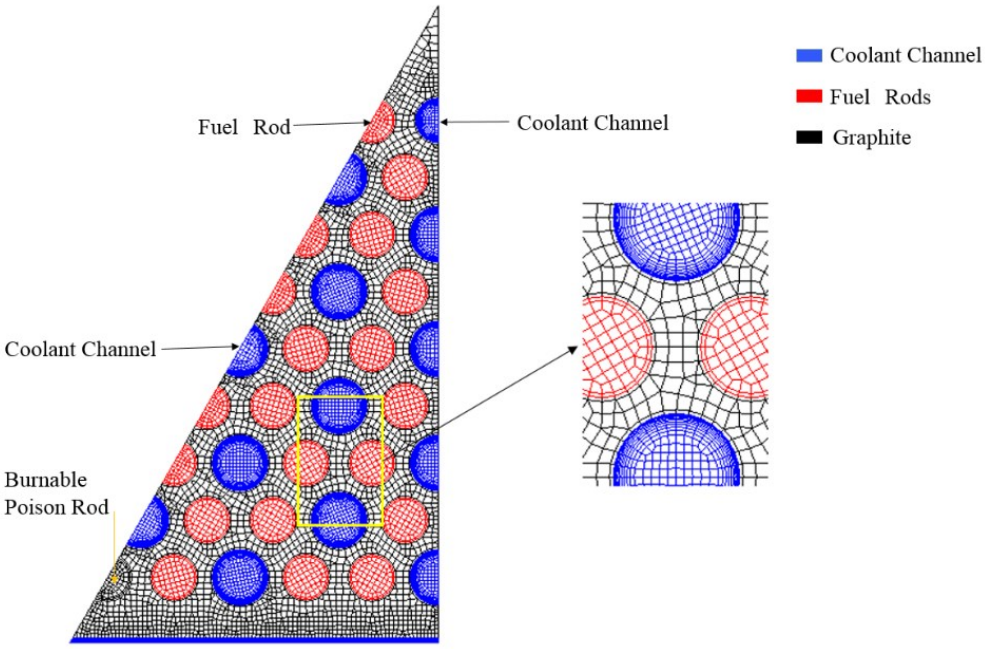

Figure 5.5 Cross-sectional view of the mesh.

As mentioned previously, the enhanced wall treatment used in this study is relying on the value of y^+ to a certain extent. Therefore, a sensitivity study for y^+ is conducted by verifying the first layer offset distance from the wall in the coolant channel. The comparison results are shown in Table 5.1. The y^+ value is set from approximately 3 to 30. The minimum y^+ acts as the baseline for comparison purpose. The maximum

difference occurs at a y^+ value of about 12, which is the difference for total mass flow rate is as high as 4.58%. The average coolant outlet temperature of the y^+=12 case is approximately 22 °C lower than that of the y^+=3 case. Therefore, a proper y^+ value is still important. However, by using the enhanced wall treatment, a wall-function mesh can also be used to achieve results without significantly reducing the accuracy.

Table 5.1 Result of y^+ sensitivity study.

y^+	Coolant channel outlet Temp. (average), °C	Total mass flow rate, kg/s	Maximum difference with the Y^+ ~3 case
~3	949.8	0.2030	-
~6	954.2	0.2011	0.94%
~12	927.4	0.2123	4.58%
~30	952.5	0.2021	0.44%

5.2.2 Turbulence model

The standard k-ε (SKE) turbulence model (Launder and Spalding, 1972) [44] with enhanced wall treatment is employed for coolant channels and gaps in this simulation.

Enhanced wall treatment is a near-wall modeling method that combines a two-layer model with enhanced wall functions. The presence of walls will have a significant influence on turbulence since the mean velocity field and turbulence change near the wall where large gradients typically occur. Usually there are three layers considered that comprise the near wall region. In the innermost layer, the flow and heat transfer are dominated by viscosity, while in the outer layer, turbulence plays the main role. An intermediate region between inner and outer layers exists where the effects of viscosity and turbulence are both not negligible. In the near-wall treatment, the viscosity-affected region and a fully turbulent region are divided by a wall-distance-based, turbulent Reynolds number, Re_y, which is defined as:

$$Re_y = \frac{\rho y \sqrt{k}}{\mu} \tag{5.1}$$

where, y is the wall-normal distance calculated at the cell centers, which is interpreted as the distance to the nearest wall, k is the turbulent kinetic energy. In the viscosity-affected region ($Re_y < Re^*; Re^* = 200$), the one-equation model of Wolfstein (1969) [49] is employed while in the fully turbulent region (Re_y>Re^*) the k-ε model is employed [49]. The enhanced wall functions were developed by smoothly blending the laminar and turbulent wall laws by using a function suggested by Kader (1981) [50]. An influence

factor of y^+ ($= \rho u_\tau y/\mu$) is defined to determine if the first near-wall mesh cell is placed in the proper region. For a very fine near-wall mesh with a small y^+ value, the enhanced wall treatment is identical to a two layer model. For a coarser mesh, enhanced wall functions will occur.

In this study, a fine boundary mesh is used in the coolant channel with an overall Y^+ of less than 6. The SIMPLE algorithm is chosen for the pressure velocity coupling method. Iteration convergence of 10^{-5} was set for all variables, and it was considered to be sufficient, as demonstrated by Sato and Johnson [51]. The changes in material properties of the helium gas, graphite, and fuel compacts due to temperature are accounted in this work by referring to a report by Idaho National Laboratory (INL) [52]. Helium properties are assumed to be isobaric at 7 MPa.

5.2.3 Validation study

The Reynolds number in the coolant channel for the present study ranges from 30,000 to 45,000 indicating fully developed turbulent flow exists in a circular channel. Since there are a number of studies and correlations for flow and heat transfer in this region, several typical published empirical correlations are chosen to be compared with the simulation results. The wall shear stress for a coolant channel with a diameter of 15.88

mm and the bypass gap are compared using the Mc Adams correlation [53], the Petukhov correlation [53] and the Blasius correlation [54], as shown in Figs.6 (a) and (b). These correlations are given as follows:

$$f = 0.184{Re_D}^{-0.2} \qquad \text{Mc Adams} \tag{5.2}$$

$$f = (0.79\ln Re_D - 1.64)^{-2} \qquad \text{Petukhov} \tag{5.3}$$

$$f = 0.3164/{Re_D}^{0.25} \qquad \text{Blasius} \tag{5.4}$$

Here, f is the friction factor, and wall shear stress τ_w is defined as:

$$\tau_w = f\rho V^2/8 \tag{5.5}$$

$$V = \frac{\dot{m}}{\rho A_c} \tag{5.6}$$

Where, ρ is density, kg/m^3; V is bulk velocity, m/s; $\dot{m}$ is mass flow rate, kg/s and A_c is the section area of the circular channel, m^2.

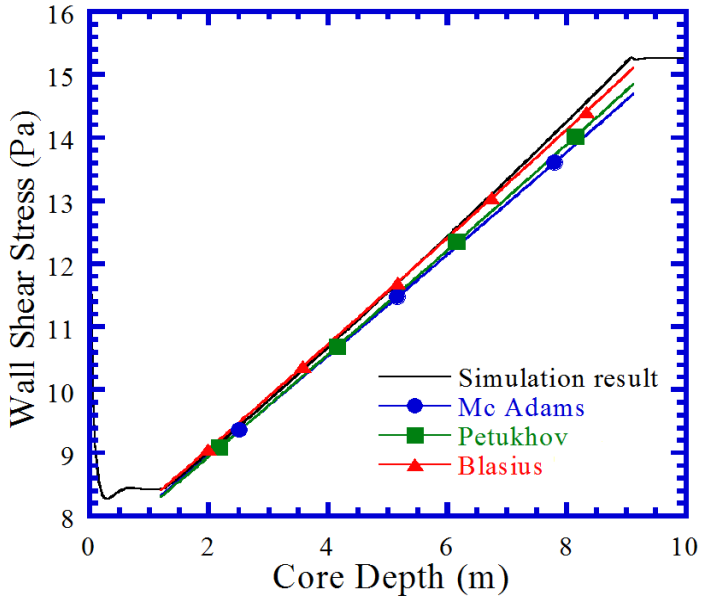

(a) Coolant channel

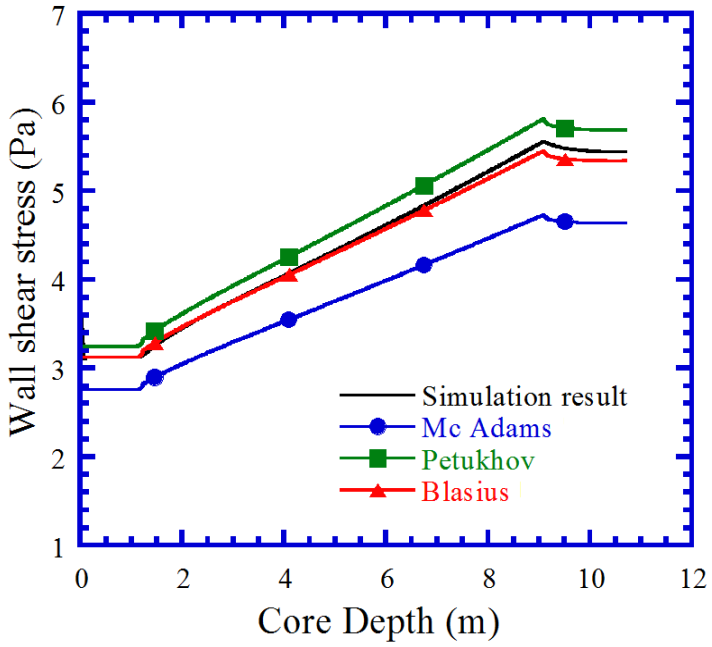

(b) Bypass gap

Figure 5.6 Comparison of wall shear stress with empirical correlations.

It can be seen from Figure 5.6 (a) that the numerical simulation results for wall shear stress in the coolant channel agree well with the empirical correlations, especially for the Blasius correlation. Additionally, the differences between simulation results using the Mc Adams and Petukhov correlations are 3.7% and 2.8%, respectively. The numerical simulation results for the wall shear stress in the bypass gap agree with the Blasius correlation, as shown in Figure 5.6 (b). Additionally, the numerical results are slightly lower when compared to the Petukhov correlation and slightly higher than the Mc Adams correlation. The wall roughness is not discussed in this study due to the lack of experimental data for actual flow and material conditions, though it will have some influence on the heat transfer process in the coolant channels and bypass gaps. Some researchers (Tung et al. 2012) [55] have numerically simulated and discussed about the effect of wall roughness on heat transfer in the coolant channels and the bypass gaps. Validation data are still needed for the numerical results.

The Reynolds number in the bypass gap is based on the gap width and calculated by Equation (5.7). For a 3 mm bypass gap, *Re* ranged from 3000 to 4200 in this study. While for a 5 mm bypass gap, *Re* ranged from 7000 to 10000. Thus, the flow in the bypass gap is considered as turbulent flow.

$$Re(\delta) = \frac{\rho V \delta}{\mu} = \frac{\dot{m}}{\mu L} \tag{5.7}$$

where, δ is the gap width, m; μ is viscosity, kg/(m•s); $\dot{m}$ is the mass flow rate, kg/s; and L is the horizontal gap length of 0.104 m.

5.2.4 Results and discussion

The location of the maximum temperature of a single fuel assembly is called a hot spot. Due to the temperature limitation of the fuel assembly, the hot spot temperature should not increase above the critical value of approximately 1600 °C [56]. Figure 5.7 shows a cross section view of the temperature and velocity distribution in a hot spot plane. The distribution is approximately 60 mm above the last prism of the fuel block. The triangle AOB is the simulated 1/12 sector of a fuel block, and the figure is obtained according to the symmetrical structure in order to show an entire fuel block.

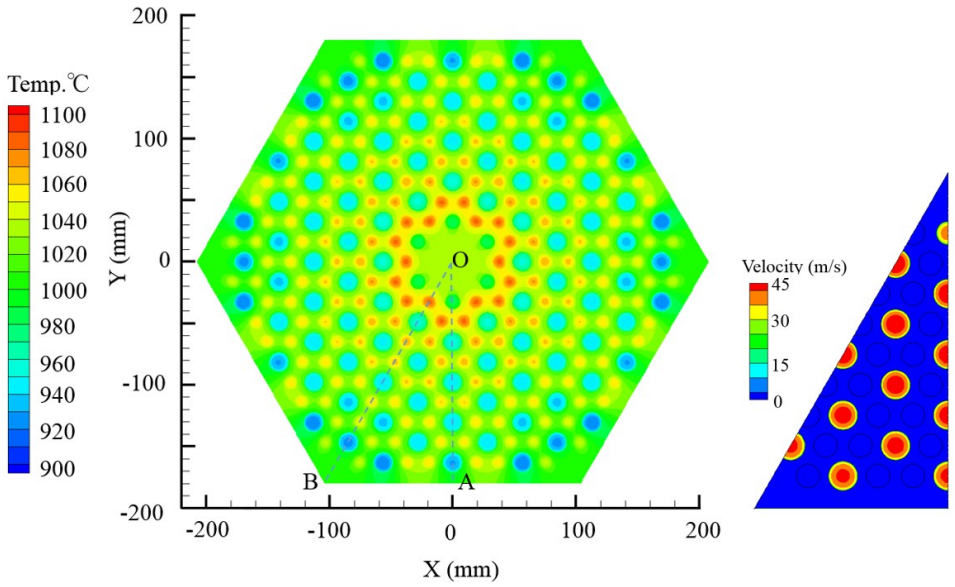

Figure 5.7 Cross-sectional view of temperature and velocity distribution at the fuel hot spot plane.

As can be seen, the temperatures of the fuel rods and coolant channels at the inner side are higher than those at the outer side. The hot spot occurs at the innermost fuel rods. The temperature of the innermost six coolant channels, which have smaller diameters of 12.7 mm, are significantly higher than for other coolant channels. This result indicates insufficient cooling in these channels. The lowest-temperature coolant channel occurs near the block side between points A and B. The temperature distribution along the OA and OB lines are shown in Figures 5.8 (a) and (b). In line OA, the valleys refer to the coolant channels. In line OB, the peaks are in a location where fuel rods exist, and valleys indicate the coolant channels. It can be determined that both the peak and valley values

decrease along the OA direction. The temperature difference between point O and point A is approximately 34 °C. For points O and B, the temperature difference is approximately 26 °C.

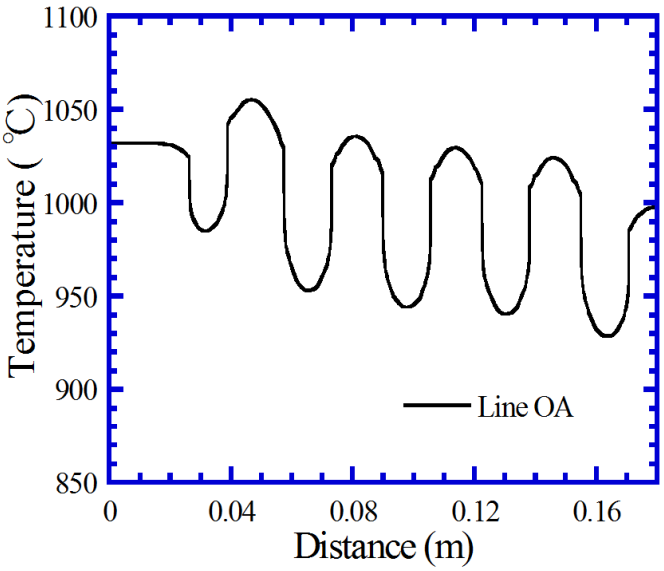

(a) Line OA

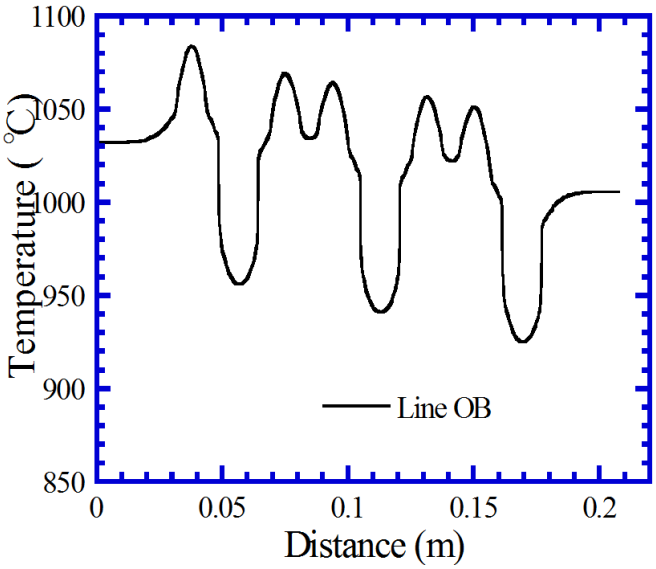

(b) Line OB

Figure 5.8 Temperature distribution along line OA and OB.

One important reason for the temperature gradient from the center of the fuel assembly to the outside is due to the smaller diameter of the innermost coolant channel. As can be seen in the velocity distribution graph (Figure 5.7), the velocity for the innermost coolant channel is less than that for the other coolant channels. A smaller diameter and velocity will both lead to insufficient cooling.

5.3 Effect of bypass flow

The bypass gap size changes over the operational lifetime due to thermal expansion and irradiation. Therefore, different bypass gap sizes should be studied to understand the effect of gap size on flow distribution and heat transfer. In this study, bypass gaps of 0 mm, 3 mm, and 5 mm are numerically simulated. Here, the bypass gaps indicate the spaces between two fuel blocks in the same prism layer. The half-size-gap is included in the one-twelfth section due to symmetry. Pressure boundary conditions are adopted here to calculate the mass flow rate distribution for each coolant channel. However, the total mass flow rate will increase with the increase of bypass gap size if the pressure difference is maintained constant. In order to investigate the effect of the bypass flow gap size on the bypass flow fraction, an approximately constant inlet total mass flow rate of 0.2 kg/s is maintained for all bypass gap size cases. The constant total mass flow rate is achieved

by changing the pressure difference within the numerical simulation.

Figure 5.9 shows the temperature distribution of the cross section with different bypass gap sizes in the upper half. In addition, the maximum and minimum coolant outlet temperature, the maximum fuel rod temperature, and the bypass flow fraction for different gap sizes are shown in the lower half. Red circles in the lower half represent the fuel rods while white circles represent the coolant channels. These are cross sections at the hot spot plane, approximately 60 mm above the last prism of the fuel block. It can be seen that the maximum fuel temperature (hot spot) increases as the gap sizes increases. With a 3 mm and a 5 mm bypass gap, the hot spot temperature increases from 1085 °C to 1109 °C and 1148 °C, respectively. This result indicates, the existence and size of the bypass gap will significantly contribute to the hot spot temperature. With an increase in the gap size, the risk of losing integrity of the coated fuel rods will increase significantly. The coolant maximum outlet temperature also increases with the increase of gap sizes and a larger temperature difference within coolant channel outlet will occur with larger gap sizes. A maximum temperature difference of approximately 141 °C exists for the 5 mm bypass gap case.

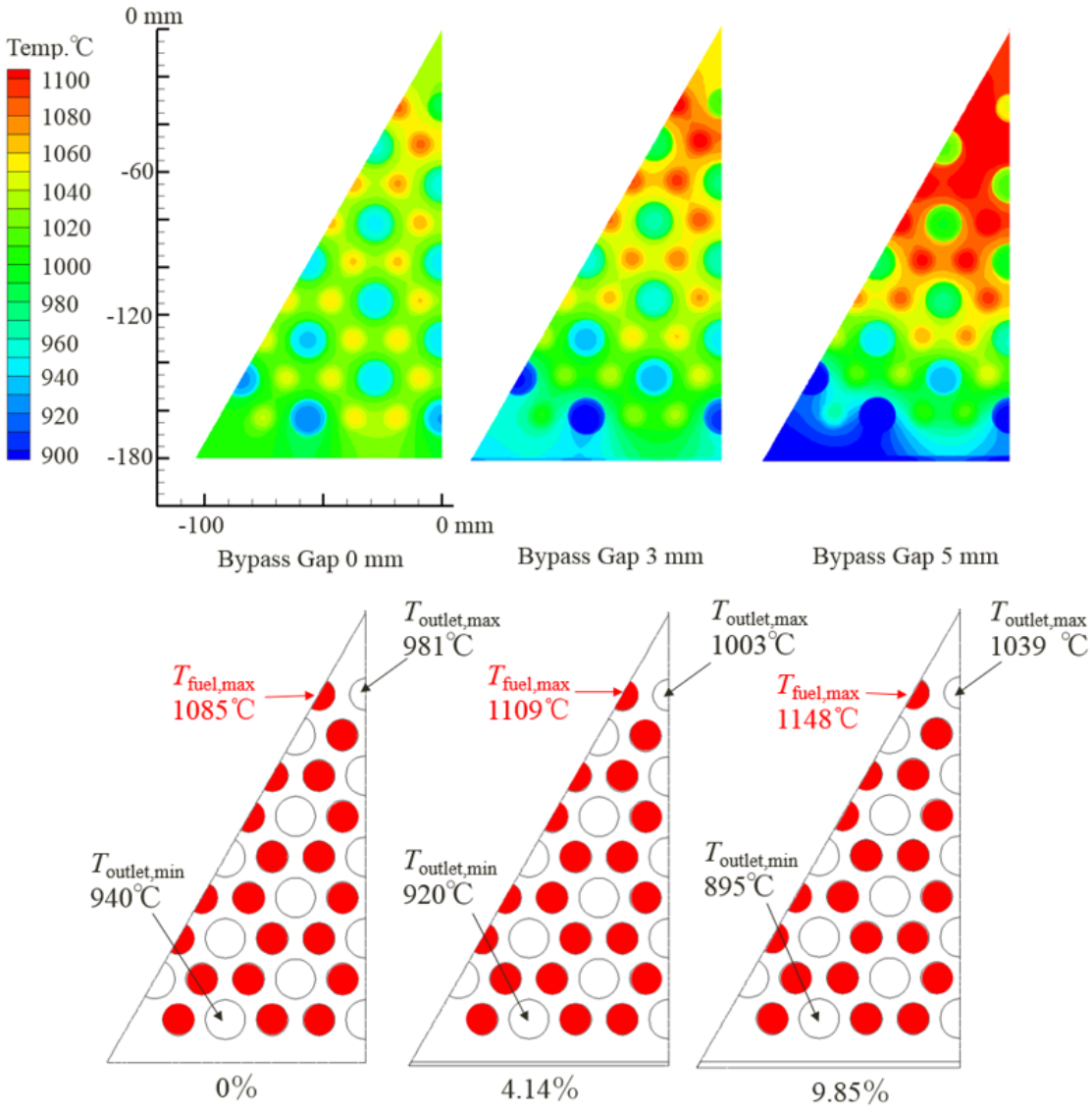

Figure 5.9 Temperature distribution and bypass flow fraction for different gap sizes.

As can be seen from the temperature distribution in Figure 5.9, which indicates the temperature gradients near the center to the outside section of the fuel block, the coolant channel and the graphite are much larger for the 5 mm bypass gap case than for the other two cases. Therefore, the existence of the bypass gap will significantly contribute to the

non-uniformity of outlet temperature of the coolant channels. This result may further lead to several undesired problems such as the “hot streaking” issue in the insulation layer of the lower plenum or insufficient mixing before flowing into the metallic outlet duct.

The mass flow rate for a 3 mm bypass gap at outlet is approximately 4.14% of total mass flow rate, and increases to 9.85% for a 5 mm bypass gap. As can be determined, the factor by which the bypass flow fraction increases is not proportional to that by which the gap size increases. While the bypass gap size increases from 3 mm to 5 mm with a factor less than 2, the flow fraction more than doubles. As the gap size increases, the flow velocity through the gap also increases. The increasing bypass flow fraction will decrease the amount of coolant flowing through designed coolant channels, leading to insufficient cooling.

5.4 Cross flow analysis

As introduced in Figure 5.2, in addition to the designed main coolant channel flow, both bypass and cross flows exist in the reactor core. Coolant flows in a direction perpendicular to the coolant holes through the interfacial gaps between two block prisms is defined as cross flow. Different cross gap sizes of 0 mm, 1 mm, and 3 mm are studied. The Reynolds number in the cross gap is less than 2300, since the cross gap size and the

velocity perpendicular to the main flow are both very minor. Therefore, the flow regions in the cross gaps are considered as laminar zones. As previously discussed, the cross flow is driven by the pressure difference between the coolant channels and the bypass gap. A bypass gap size of 5 mm is used in this study. Pressure boundary conditions are adopted for the inlet and outlet coolant channels. Inlet static pressure is maintained at approximately 7 MPa. To maintain a constant total mass flow rate of 0.2 kg/s, a pressure difference of 28.9 kPa is set for the calculation. In total, nine layers of cross gaps between ten fuel block prisms are considered.

The cross-sectional view of the pressure and temperature distribution between the last two prisms is shown in Figure 5.10. This is the case for a cross gap of 0 mm. From the pressure distribution, it can be found that the pressure for the bypass gap is higher than for the nearby coolant channels. Additionally, for the coolant channels, which are located near the center of the fuel block, have higher pressures than the outside region. The pressure distribution for the coolant channels has a similar profile as the temperature distribution.

According to the pressure distribution, a cross flow will flow from bypass gap to the nearby coolant channels due to pressure difference. This cross flow will decrease the amount of coolant in the bypass gaps and increase the coolant in the coolant channels. As

previously mentioned, the decreasing bypass flow fraction will lead to a decrease in the fuel hot spot temperature. In addition, a cross flow between coolant channels will also occur from the interior coolant channels to the outer coolant channels owing to the pressure difference. This type of cross flow will contribute to the flow mixing in the cross gaps. However, the coolant flowing from interior coolant channels to the outer channels will result in an increasing temperature difference since the temperatures are higher in the interior thereby requiring additional coolant. Therefore, the cross flow between coolant channels will have negative effect on heat transfer in the fuel block and lead to an increase in localized hot spot temperature.

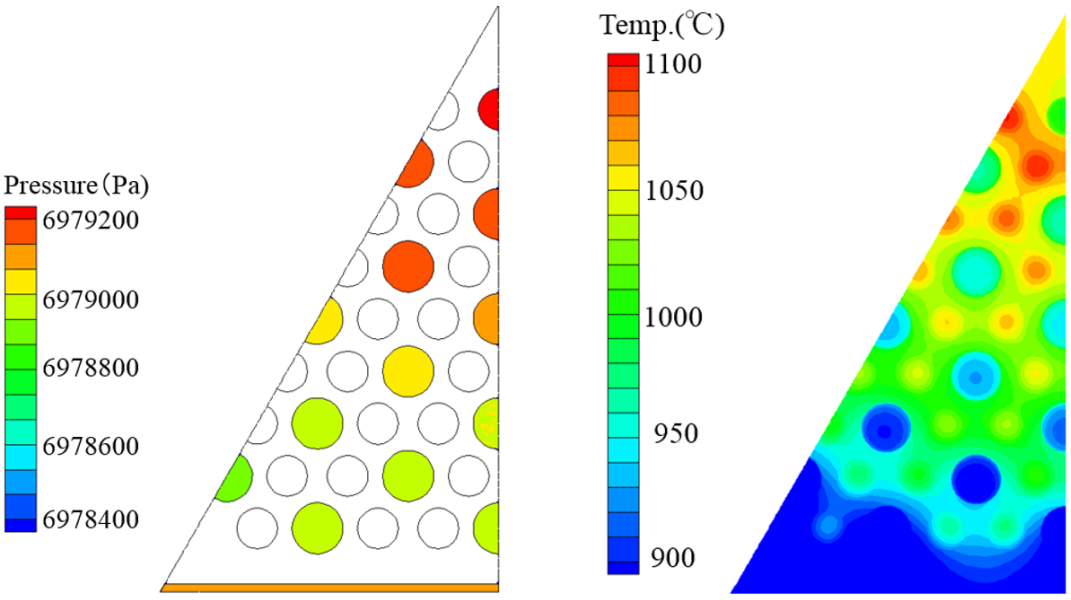

Figure 5.10 Pressure and temperature distribution for no cross gap case at cross section between 9th and 10th fuel block.

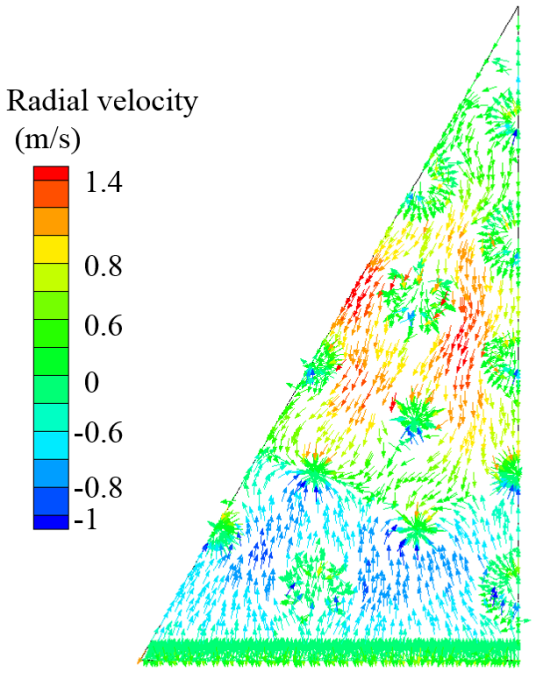

Figure 5.11 Velocity distribution of the cross flow between 9th and 10th fuel block.

A typical cross section view of the velocity distribution for the 1mm cross gap case is shown in Figure 5.11. The location of the figure is in the middle of the cross gap. The blue arrows show the cross flow from a bypass gap to the nearby coolant channels. The red arrows indicate the cross flow from the higher pressure coolant channels to lower pressure channels. The two types of cross flow will mix in the middle section of the fuel block. Additionally, the two types of flow will have an opposing influence on hot spot temperature.

The effect of cross gap size on the bypass flow fraction, cross flow fraction, hot spot

temperature, and coolant channel outlet temperature difference is shown in Table 5.2. Here the bypass flow fraction is the mass flow rate of bypass flow at the outlet divided by the total inlet mass flow rate of the model. The cross flow fraction is the mass flow rate of cross flow through bypass gap divided by total inlet mass flow rate of the model. The bypass flow fraction decreases with a slight increase in the cross gap size owing to cross flow. The hot spot temperature decreases only 1 °C and the influence of gap size is insignificant. With the existence of a cross gap, the coolant channel outlet temperature difference decreases from 143.5 °C to 136.3 °C. However, cross gap sizes of 1 mm and 3 mm do not show comparatively large differences. The improvement in the uniformity of the coolant channel outlet temperature is believed to be a result of the cross flow between the ten prism layers.

Table 5.2 Effect of cross gap size on flow and temperature distribution.

	Cross gap 0 mm	Cross gap 1 mm	Cross gap 3 mm
Total mass flow rate (kg/s)	0.20	0.20	0.20
Bypass flow fraction (%)	9.85	9.58	9.55
Cross flow fraction (%)	0	0.27	0.30
Hot spot temperature (°C)	1148.6	1146.8	1147.0
Coolant outlet ΔT_{max} (°C)	143.5	136.3	136.3

5.5 Summary

A 3D full size model of a fuel column in a reference prismatic VHTR is developed for heat transfer and flow distribution simulation by applying commercial CFD codes. Both the core bypass and cross flows are investigated for various gap sizes. A mesh validation is performed by adapting a finer mesh in the solid area. Additionally, a sensitivity study for the value of Y^+ is performed for a range of 3 to 30. The calculation result of the friction coefficient for a coolant channel from the inlet to outlet is compared to published empirical correlations. The results show agreement and the SKE turbulence model used in this calculation was validated. However, in the cross gaps, the flow involves transition from laminar to turbulent conditions. Numerical results for such application still require further consideration and validation data obtained at actual flow and material conditions. The effects of the bypass flow and cross flow on hot spot temperature, coolant outlet temperature differences, and mass flow rates are clarified as follows:

(1) The bypass flow has significant influence on heat transfer in the fuel column. With a larger bypass gap size, a larger temperature gradient will occur within the fuel block.

(2) The hot spot temperature rises as the bypass gap size increases.

(3) Coolant channel outlet temperature difference increases with an increase in the bypass gap size. This result will increase the risk of “hot streaking” or insufficient mixing in the lower plenum.

(4) Cross flow is driven by the pressure difference between the bypass gap and the coolant channels.

(5) The cross flow from the bypass gap to the coolant channels will contribute to heat transfer capabilities and decrease the temperature gradient. Additionally, the cross flow from the interior high-pressure channels to the outer low-pressure channels will decrease the available coolant in the hot areas and increase temperature gradient.

(6) The existence of a cross flow will decrease the maximum coolant channel outlet temperature difference, while the gap size shows little influence on the overall result.

Chapter VI

Conclusions

In this work, experimental research for forced convection transient heat transfer between the twisted plate and the coolant (helium gas) was conducted. 3D numerical simulation was applied to analyze the heat transfer process and the twisted structure induced heat transfer enhancement mechanism. In addition, thermal-hydraulics analyses for reactor core by applying Computational Fluid Dynamics (CFD) were performed.

Experiment was carried out at various periods ranged from 35 ms to 14 s. The transient heat transfer effect with various heat generation period was clarified and empirical correlations for both transient Nusselt number and quasi-steady state Nusselt number were obtained. The heat transfer enhancement effect by twisted structure effect was also clarified.

Simulation results for forced convection heat transfer of helium gas flowing over twisted plates were obtained for average surface temperature difference, heat flux and heat transfer coefficient of the twisted plate and showed reasonable agreement with experimental data. Based on the numerical simulation, mechanism of local heat transfer coefficient distribution was clarified. A comparison of the twisted plate and flat plate was conducted to show the difference in heat transfer coefficient distribution.

Thermal hydraulics analysis for reactor core was performed with CFD method. The effect of bypass flow and cross flow gaps in the core of a VHTR were taken into consideration. Parametric study by changing the size of bypass gap and cross gap are performed with a one-twelfth sector of fuel block. Simulation results show the influence of bypass gap size on temperature distribution and coolant mass flow rate distribution in the prismatic core. It is shown that the maximum fuel and coolant channel outlet temperature increases with the increase of gap size which may lead to a risk on the structure of fuel block. The cross flow is divided to two kinds. One is the cross flow from bypass gap to coolant channels and another is the flow from high pressure coolant channels to low pressure coolant channels. These two kinds of flow have opposite influence on temperature gradient. It is found that the presence of the cross flow gaps may have a significant effect on the distribution of the coolant in the core due to flow mixing in the cross gaps.

References

[1] Gralla F., John B. Abson D., etc. The role of sustainability in nuclear energy plans-what do national energy strategies tell us? Energy Research & Social Science, Vol.22, pp. 94-106, 2016.

[2] Brundtland G. H. World commission on environment and development. Environmental Policy and Law, Vol.14, pp. 26-30, 1985.

[3] Abram T., Ion S. Generation-IV nuclear power: A review of the state of the science. Energy Policy, Vol.36, pp. 4323-4330, 2008.

[4] Krivit S. B., Lehr J. H. Kingery T. B. Nuclear energy encyclopedia. Wiley series on energy, John Wiley & Sons, INC., 2011.

[5] Futterer M., Fu L., Sink C., etc. Status of the very high temperature reactor system. Progress in Nuclear Energy, Vol.77, pp. 266-281, 2014.

[6] Beck J.M., Pincock L. F. High temperature gas-cooled reactors lessons learned applicable to the next generation nuclear plant. INL/EXT-10-19329, 2011.

[7] Lee Y. W., Park J. Y., Kim Y. K. etc. Development of HTGR-coated particle fuel technology in Korea. Nuclear Engineering and Design, Vol.238, pp. 2842-2853, 2008.

[8] Wu Z.X., Lin D. C. Zhong D. X. The design features of the HTR-10. Nuclear

Engineering and Design, Vol.218, pp. 25-32, 2002.

[9] Hittner D., Angulo C., Basini V. HTR-TN achievements and prospects for future developments. Journal of Engineering for Gas Turbine and Power, Vol.133, 064001-1, 2011.

[10] Energy Policy Act of 2005, US Congress.

[11] Thomas S. The pebble bed modular reactor: An obituary. Energy Policy, Vol.39, pp. 2431-2440, 2011

[12] McEligot, D.M., McCreery, G.E., 2004. Scaling Studies and Conceptual Experiment Design for NGNP CFD Assessment. INEEL/EXT-04-02502.

[13] Soliman, M., Johnson, H.A. Transient heat transfer for forced convection flow over a flat plate of appreciable thermal capacity and containing an exponential time-dependent heat source. International Journal of Heat and Mass Transfer, Vol.11, No.1, pp.27-38, 1968.

[14] Kataoka, I., Serizawa, A. and Sakurai, A. Transient boiling heat transfer under forced convection. International Journal of Heat and Mass Transfer, Vol.26, No.4, pp.583-595, 1983.

[15] Liu, Q.S, Fukuda, K., and Zheng Z. Theoretical and experimental studies on transient heat transfer for forced convection flow of helium gas over a horizontal cylinder.

JSME International Journal, Series B, Vol.49, No.2, pp.326-333, 2006.

[16] Liu, Q.S., Shibahara, M., and Fukuda, K. Transient heat transfer for forced convection flow of helium gas over a horizontal plate. Experimental Heat Transfer, Vol.21, No.3, pp.206-219, 2008.

[17] Liu, Q.S., Zhao, Z., Fukuda, K. Transient heat transfer for forced flow of helium gas along a horizontal plate with different width. International Journal of Heat& Mass Transfer, Vol.75, pp433-441, 2014.

[18] Liu, Q.S., Fukuda, K., Shibahara, M. Transient heat transfer from single horizontal heaters in forced flow helium gas at exponentially increasing heat inputs. ASME Summer Heat Transfer Conference, Paper No. HT2008-56274, pp.1-11, 2008.

[19] Gordeev. S, Heinzel. V, Slobodtchouk. V. Features of convective heat transfer in heated helium channel flow, International Journal of Heat and Mass Transfer, Vol.48, pp.3363-3380, 2005.

[20] Chen. Y, Arbeiter. F, Heinzel. V, Schlindwein. G., Transient conjugated heat transfer within IFMIF high flux test module, Nuclear Engineering and Design, Vol.249, pp.172-179, 2012.

[21] Leung C W, Chan T L, Probert S D, Kang H J. Forced convection from a horizontal ribbed rectangular base-plate penetrated by arrays of holes. Appl. Energy, 62(2):81-

95, 1999.

[22] Saha S. K., Dutta A. and Dhal S. K., Friction and Heat Transfer Characteristics of Laminar Swirl Flow Through a Circular Tube Fitted with Regularly Spaced Twisted-Tape Elements, Int. J. Heat and Mass Transfer, Vol.44, pp.4211-4223, 2001.

[23] Manglik, R. M., Bergles, A. E. Heat transfer and pressure drop correlations for twisted-tape-inserts in isothermal tubes: Part I- laminar flows. Journal of Heat Transfer, Vol.115, pp.881-889, 1993.

[24] Manglik, R. M., Bergles, A. E. Heat transfer and pressure drop correlations for twisted-tape-inserts in isothermal tubes: Part II- transition and turbulent flows. Journal of Heat Transfer, Vol.115, pp.890-896 , 1993.

[25] Manglik, R. M., Bergles, A. E. Characterization of twisted-tape-induced helical swirl flows for enhancement of forced convective heat transfer in single-phase and two-phase flows. Journal of Thermal Science and Engineering Applications, Vol.5, Paper No. 021010-1, pp.1-12, 2013.

[26] Hata, K. and Masuzaki, S. Twisted-tape-induced swirl flow heat transfer and pressure drop in a short circular tube under velocities controlled. Nuclear Engineering and Design, 241(11), pp.4434-4444, 2011.

[27] Nakano M., Tuji N. and Tazawa Y. Conceptual Reactor Design Study of Very High

Temperature Reactor (VHTR) with Prismatic-Type Core. Journal of Power Energy System Vol.2, pp. 768-774, 2008.

[28] Yoon S.J., Lee J.H., Kim M.H. and Park G.C. The Effects of Crossflow Gap and Axial Bypass Gap Distribution on the Flow Characteristics in Prismatic VHTR Core", Nuclear Engineering and Design. Vol. 250, pp. 465-479, 2012.

[29] Tak N., Kim M.H. and Lee W. J. Numerical Investigation of a Heat Transfer within the Prismatic Fuel Assembly of a Very High Temperature Reactor. Annals of Nuclear Energy, Vol. 35, pp. 1892-1899, 2008.

[30] Travis B W, El-Genk M S. Numerical simulation and turbulent convection heat transfer correlation for coolant channels in a very-high-temperature reactor. Heat Transfer Engineering. Vol.34 (1), pp. 1-14, 22013.

[31] Travis B W, El-Genk M S. Thermal-hydraulics analyses for 1/6 prismatic VHTR core and fuel element with and without bypass flow. Energy Conversion and Management, Vol. 67, pp. 325-341, 2013.

[32] Sato H., Johnson R. W. and Schultz R. Computational Fluid Dynamic Analysis of Core Bypass Flow Phenomena in a Prismatic VHTR. Annals of Nuclear Energy, Vol. 37, pp. 1172-1185, 2010.

[33] Johnson R.W. and Sato H. Bypass Flow Computations Using a One-twelfth

Symmetric Sector for Normal Operation in a 350MWth Prismatic VHTR. Nuclear Engineering and Design. Vol. 251, pp. 84-91, 2012.

[34] Wang H.H., Dominguez-Ontiveros E., Hassan Y.A. Computational Fluid Dynamics Analysis of Core Bypass Flow and Cross Flow in a Prismatic Very High Temperature Gas-Cooled Nuclear Reactor Based on a Two-Layer Block Model. Nuclear Engineering and Design, Vol. 268, pp. 64-76, 2014.

[35] Zhao Z, Liu Q S, Fukuda K. Experimental and numerical study on transient heat transfer for helium gas flowing over a flat plat containing an exponentially increasing heat source. Mechanical Engineering Journal, Vol. 1(4), pp. 1-13, 2014.

[36] Fukuda, K., Liu, Q. S. Steady and transient critical heat fluxes on a horizontal cylinder in a pool of freon-113, International Journal of Transport Phenomena, Vol.7, pp.71-83, 2005.

[37] Liu, Q.S., Shiotsu, M., and Sakurai, A. A Correlation for forced convection film boiling heat transfer from a horizontal cylinder, Two-Phase Flow and Heat Transfer, ed. by J. H. Kim et al., ASME Book, HTD-Vol. 197, pp. 101-110, 1992.

[38] Shibahara M., Liu Q.S., and Fukuda K., Transient forced convection heat transfer for nitrogen gas flowing over plate heater with exponentially increasing heat input, International Journal of Heat and Mass Transfer, Vol. 95, pp. 405-415, 2016.

[39] ANSI/ASME PTC 19.1-1985, Measurement uncertainty, supplement on instruments and apparatus, part 1, 1987.

[40] Holman J P. Heat transfer (10th Edition). The McGraw-Hill Companies (2010), Inc. pp. 187-194.

[41] Dittus F. W., Boelter L. M. K., Heat transfer in automobile radiators of tubular type, Int. Comm. Heat mass transfer, Vol.12, pp.3-22, 1985.

[42] Ansys Inc., Ansys Fluent, Version 14, Theory guide, 2012.

[43] Daiguji H., Miyake Y., Yoshizawa A., Computational fluid dynamics of turbulent flow-models and numerical methods, University of Tokyo Press, pp. 371-395, 1998 (in Japanese).

[44] Launder B.E., Spalding D.B., Lectures in mathematical models of turbulence, Academic Press, London, England, 1972.

[45] Liu Q S, Zhao Z, Fukuda K. Experimental study on transient heat transfer enhancement from a twisted plate in convection flow of helium gas. International Journal of Heat and Mass Transfer, Vol. 90, pp. 1160–1169, 2015.

[46] Liu Q S, Zhao Z, Fukuda K. Width effect and local heat transfer characteristics for helium gas flowing over a twisted plate. Journal of Nuclear Science and Technology, Vol. 23 (2), pp. 22-231, 2015.

[47] Moses, D.L. Very High-Temperature Reactor (VHTR) Proliferation Resistance and Physical Protection (PR& PP). ORNL/TM-2010/163, 2010.

[48] Burchell, T.D. Radiation effects in graphite and carbon-based materials. MRS Bulletin, Vol.04(22), pp. 29-35, 1997.

[49] Wolfstein, M. The velocity and temperature distribution of one-dimensional flow with turbulence augmentation and pressure gradient, International Journal of Heat and Mass Transfer, Vol. 12, pp. 301-318, 1969.

[50] Kader, B. Temperature and concentration profiles in fully turbulent boundary layers, International Journal of Heat and Mass Transfer, Vol.24 (9), pp. 1541-1544, 1981.

[51] Sato, H., Johnson, R.W., Schultz, R.R. Computational fluid dynamic analysis of core bypass flow phenomena in a prismatic VHTR. Annals of Nuclear Energy, Vol. 37, pp. 1172-1185, 2010.

[52] Johnson, R.W., Sato, H., Schultz, R.R. CFD Analysis of Core Bypass Phenomena, INL/EXT-09-16882, 2009.

[53] Incropera, F.P., DeWitt, D.P., Bergman, T.L., Lavine, A.S. Fundamentals of Heat and Mass Transfer 6th Edition, Chapter 8, John Wiley & Sons, Inc., New York, 2007.

[54] Schlichting, H. Boundary-Layer Theory 7th Edition, Chapter XX, McGraw-Hill, Inc., United States of America, 1979.

[55] Tung, Y., Johnson, R. W., Sato, H. Effect of graphite surface roughness on bypass flow computations for a HTGR. Nuclear Engineering and Design, Vol.252, pp.78-87, 2012.

[56] Chapin, D., Kiffer, S., Nestell, J. The Very High Temperature Reactor: A Technical Summary, MPR Associates Inc, 2004..

Publications concerning with this doctoral dissertation

Journal papers

[1] Li Wang, Qiusheng Liu and Katsuya Fukuda, ”Numerical solution on transient heat transfer for forced convection flow of helium gas over a twisted plate with different helical pitch”, ***Journal of the JIME***, Vol. 50(6), pp.776-781, (2015).

[2] Li Wang, Qiusheng Liu and Katsuya Fukuda, “Experimental and numerical study on transient heat transfer for a twisted plate with different length in helium gas at various velocities”, ***Journal of Nuclear Science and Technology***, Vol.53, No.10, pp.1535-1545, (2016).

[3] Li Wang, Qiusheng Liu and Katsuya Fukuda, “Experimental and numerical study of transient heat transfer for forced convection flow of helium gas over a twisted plate”, ***Journal of Thermal Science and Technology***, Vol.11, No.1, pp.1-16, (2016).

[4] Li Wang, Qiusheng Liu and Katsuya Fukuda, ”Numerical solution of heat transfer process in a VHTR core accompanying bypass and cross flows”, ***Nuclear Engineering and Design***, Vol. 307, pp. 275-283, (2016).

国際会議

[1] Li Wang, Qiusheng Liu and Katsuya Fukuda, “Numerical solution on transient heat transfer for forced convection flow of helium gas over a twisted plate with different helical pitch”, ***Proceedings of International Symposium on Marine Engineering (ISME2014)***, Paper No.119, pp.1-6, Harbin, China, (2014).

[2] Li Wang, Qiusheng Liu and Katsuya Fukuda, “Numerical study on transient heat transfer for forced convection flow of helium gas over a twisted plate”, ***3rd International Symposium of Maritime Sciences***, pp.149-154, Kobe, (2014).

[3] Li Wang, Qiusheng Liu and Katsuya Fukuda, “Experimental and numerical study on transient heat transfer for helium gas flowing over a twisted plate with different length”, ***23th International Conference on Nuclear Engineering (ICONE-23)***, paper 1035, JAPAN, (2015).

[4] Li Wang, Qiusheng Liu and Katsuya Fukuda, “Numerical Solution of Heat Transfer Process in a Prismatic VHTR Considering Core Bypass and Cross Flow”, ***16th International Topical Meeting on Nuclear Reactor Thermal hydraulics (NURETH-16)***, pp.7872-7885, Chicago, USA. (2015).

[5] Li Wang, Qiusheng Liu, Makoto Shibahara and Katsuya Fukuda, “Thermal-hydraulic analysis for prismatic very high temperature reactor”, ***Proceedings of the First Pacific Rim Thermal Engineering Conference***, paper number-14472. Hawaii, USA, (2016).

国内講演会

[1] 王麗, 劉秋生, 福田勝哉, “ヘリウムガスにおける種々長さのねじり発熱体の過渡熱伝達に関する実験及び理論的研究”, 日本機械学会熱工学コンファレンス学術講演会論文集,C142, 2014 年,東京.

[2] Li Wang, Qiusheng Liu and Katsuya Fukuda, “ヘリウムガスにおけるねじり発熱体の過渡熱伝達に関する数値シミュレーション”, 第 84 回日本マリンエンジニアリング学術講演会論文集, pp.125-126, 2014 年,下関.(優秀発表賞受賞)

[3] 王麗, 劉秋生, 福田勝哉, “超高温ガス炉の炉心燃料要素体における伝熱と流動の数値シミュレーション”, 第 51 回日本伝熱シンポジュウム学術講演会論文集, SP404, 2015 年, 福岡.

[4] 王麗, 劉秋生, 福田勝哉, 柴原誠, “種々長さのねじり発熱体の過渡熱伝達に

関する研究”,若手フロンディア研究会 2015，神戸大学百年記念館

Appendix

A.1 Photos of Test Loop

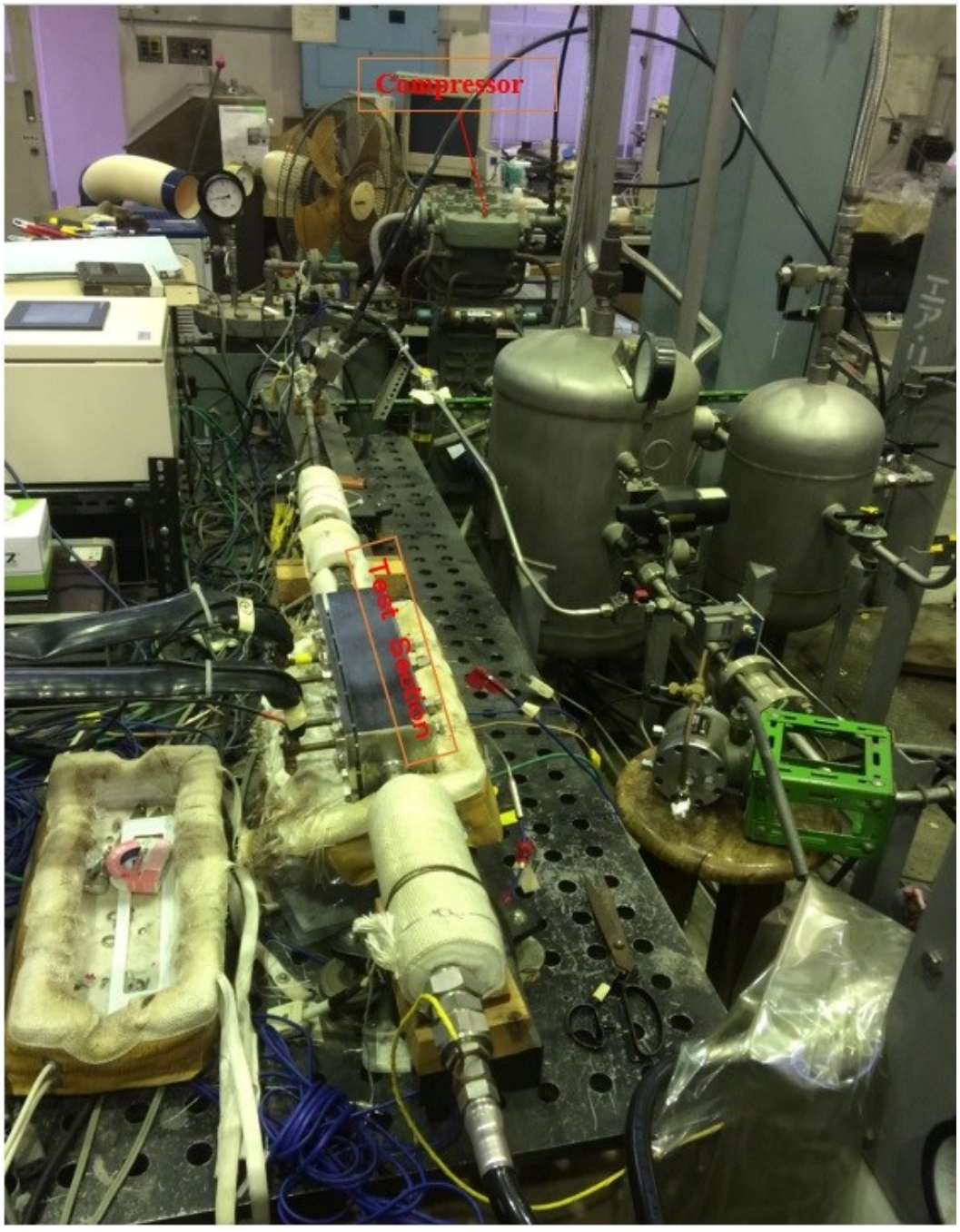

Fig.A.1 Test loop

A.2 The preheating system

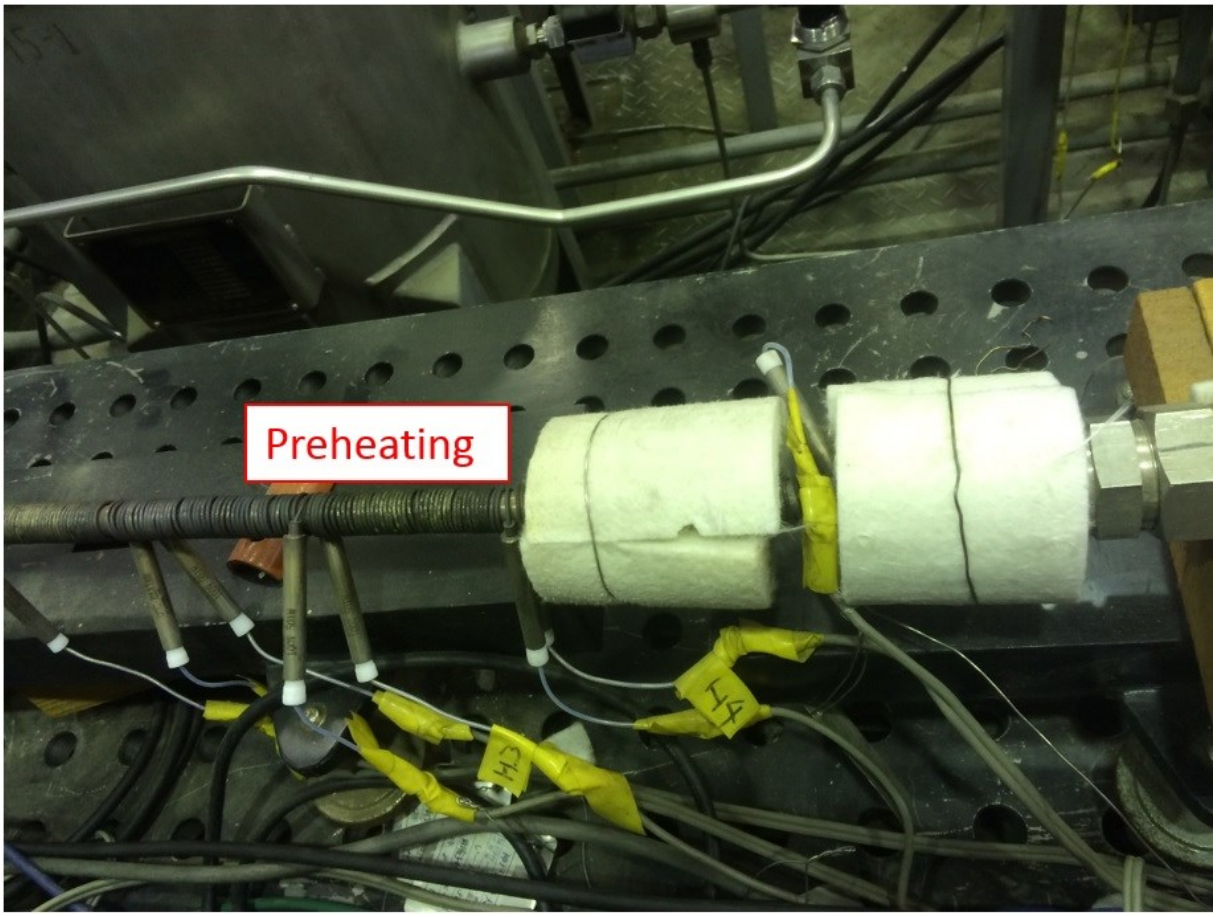

Fig.A.2 The preheating system

A.3 The test section

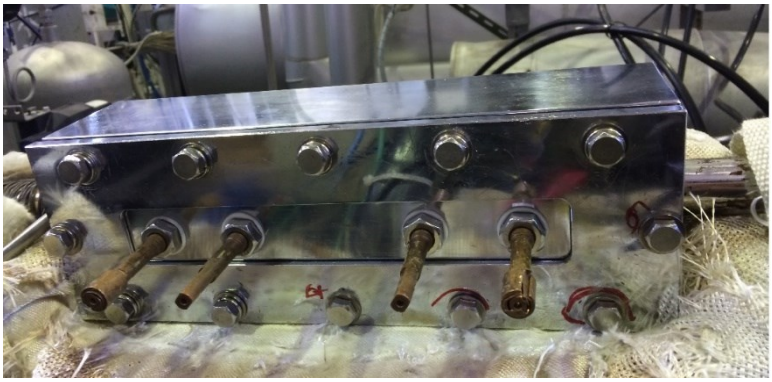

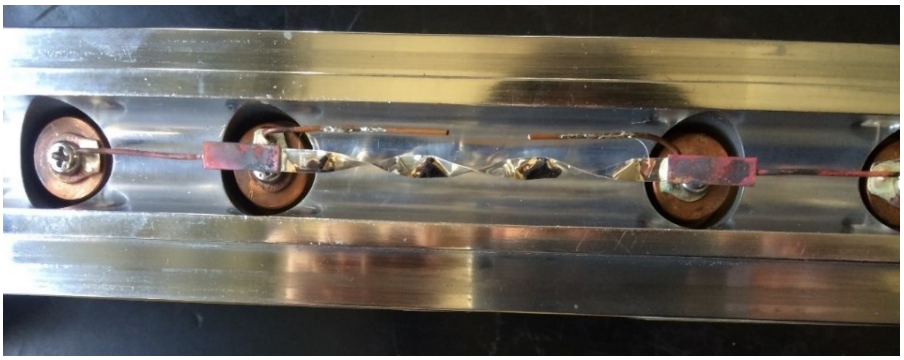

Fig.A.3 The test section

A.4 DC power supply.

Fig.A.4 DC power supply.